BIO-BUTANOL FUEL ATOMIZATION AND COMBUSTION PROCESSES

BY

MARIA AGATHOU

DISSERTATION

Submitted in partial fulfillment of the requirements
for the degree of Doctor of Philosophy in Mechanical Engineering
in the Graduate College of the
University of Illinois at Urbana-Champaign, 2010

Urbana, Illinois

Doctoral Committee:

Associate Professor Dimitrios C. Kyritsis, Chair
Professor Quinn M. Brewster
Professor Alan C. Hansen
Professor Chia-Fon Lee

ABSTRACT

Three bio-butanol fuel atomization and combustion technologies were considered, namely butanol electrostatic sprays, butanol non-premixed flames, and butanol kinetic modeling in view of the emergence of methods of production of this fuel from biological sources.

Butanol electrospray (e-spray) phenomenology was investigated through high-speed visualization and compared with the corresponding electrosprays of ethanol, heptane and butanol-containing mixtures. Electrospray structure was probed using Phase Doppler Anemometry and both droplet size and velocity measurements were obtained for sprays of butanol and butanol-containing fuel blends. These results indicated an unstable and polydisperse electrospray behavior for most conditions. Several factors were identified as responsible for this unstable behavior and were investigated experimentally. These included: e-spray menisci oscillations, instabilities initiating the droplet break-up, secondary droplet break-up because of high Weber numbers and finally stability of butanol electrical conductivity with applied voltage. Stable butanol electrosprays were achieved within a narrow region of low flow rates and a non-dimensional analysis was performed in order to develop an empirical expression correlating the dimensionless average diameter, flow rate and applied voltage.

Butanol non-premixed flames were studied in a counter-flow burner configuration. Major combustion species were measured using line Raman imaging and

K-type thermocouples were used in order to perform temperature scans across the flame. Also, extinction strain rates were measured as a function of overall stoichiometry. Butanol flames were compared with flames of methane (which is not oxygenated) as well as ethanol which is a currently widely employed biofuel and with butanol-methane mixture flames. It was shown that butanol flames could sustain higher strain rates at extinction than ethanol flames but significantly smaller than methane flames. For the strongly diluted flames under consideration, it was shown that temperature followed a very closely linear relation with nitrogen concentration. For the same nitrogen concentration, butanol exhibited lower temperatures at the same overall stoichiometry and heat release, because of the higher average molecular weight of the fuel stream. In addition, the possibility of estimating the scalar dissipation rate at the stoichiometric surface χ_{stoich} was investigated through a measurement of the mixing layer thickness. It was proven that approximating the mixing layer thickness through the gradient of the mixture fraction at the stoichiometric surface, offered a good estimation of χ_{stoich}.

Butanol kinetic modeling was studied in a zero-dimensional piston-cylinder assembly and a MATLAB code was used in order to solve the energy conservation and species equations. Pressure and temperature results were provided as a function of time, along with mol fractions of major species and combustion intermediates. The same calculation was performed for ethanol and n-heptane. It was shown that butanol peak pressures and temperatures were lower than the corresponding values for the other two fuels and that its autoignition occurred after a longer time interval.

ACKNOWLEDGEMENTS

First, I would like to express my sincere gratitude to my academic advisor Prof. Kyritsis, for sharing with me his invaluable expertise and endless motivation. His optimism and dedication kept me sane, especially at the times when the completion of this work seemed a utopia. And frankly speaking, it would have been one, without his talent of successfully and consistently converting my frustration into motive. Today, I am proud of being not only his colleague, but also his friend. Moreover, I would like to express my appreciation to my senior lab-mates Suzy Smith, Kowtilya Bijjula, Chris Evans, Taekyu Kang, and Eric Anderson for their eager assistance and encouragement. In particular, I deeply thank Suzy, Kowtilya and Chris for honoring me with their friendship as well.

I am more grateful to my fiancé, Manolis, than I can ever express. Except for his endless love, support and patience, I thank him for our full of inspiration conversations on culture, hopes and dreams, that kept reminding me that my definition of life still exists beyond the border of Champaign. My parents and sister Christina, have also been incredibly supportive. I want to thank them for their infinite trust and encouragement and for helping me develop the most valuable virtue; independent thought, which has led me to the paths I have walked through the years.

Finally, I would like to acknowledge the support of the U.S. Department of Energy through the Graduate Automotive Technology Education (GATE) Center of

Excellence at the University of Illinois as well as the American Chemical Society Petroleum Research Fund (Grant # PRF 42287 – G9-Dr. David L. Schutt, Acting Program Director), as well as of the U.S. National Science Foundation (grant CTS 04-48968CAR - Dr.Phillip Westmoreland, contract monitor).

TABLE OF CONTENTS

LIST OF TABLES

LIST OF FIGURES

CHAPTER 1

INTRODUCTION

1.1 Motivation

Recent research has shown the possibility of producing butanol efficiently with the use of fermentation microorganisms (*clostridia)* [1-4]. This could potentially lead to the production from renewable sources of a fuel that has energy density significantly increased with respect to the currently widely used ethanol. This is because of the smaller oxygen content of the butanol molecule (22%) compared to the oxygen content of the currently used ethanol (35%) that butanol has only 18% smaller energy content (in terms of MJ/kg) than gasoline as compared to the 45% deficit of ethanol. This advantage is, of course, conditioned on the assumption that other combustion metrics such as pollutants (soot, NOx) remain within acceptable limits.

Moreover, butanol is a fuel that does not require engine modifications and can be directly utilized in the existing infrastructure. Its combustion in an internal combustion engine environment is potentially beneficial in terms of emissions. In particular, combustion of butanol-diesel blends shows decreased levels of CO and soot as well as of NOx when compared to pure diesel results [54]. Butanol addition influences negatively only the formation of HC [54].

An additional very attractive feature of butanol is that it is a molecule with significantly longer carbon-chain than ethanol, which means that it can be produced with processes that can be significantly less energy-consuming than ethanol, since the long organic bio-molecules that are to be used as raw material need not be broken down to the level of the two-carbon ethanol molecule, but the related biological processes can stop much earlier. Furthermore, butanol, unlike ethanol, can mix with petroleum diesel, without the addition of co-solvents.

Table 1.1 presents the properties of butanol in comparison with the ones of ethanol, gasoline and diesel. It should be noted that for the case of butanol, these are average properties for the four butanol isomers.

Table 1.1 Properties of butanol, ethanol and gasoline

Fuel	Energy density (MJ/kg)	Stoich A/F ratio	Heat of vaporization (MJ/kg)	Density (g/cm^3)	R-octane rating	Kin. Visc. (cSt)
Gasoline	44.9	14.0	0.36	0.712	91-99	0.4-0.8
Ethanol	24.8	9.0	0.92	0.789	130	1.52
Butanol	36.4	11.2	0.43	0.802	96	3.64
Diesel	42.5	14.7	0.27-0.86	0.820-0.860	Cetane number: 40-55	2.8

Because butanol has only recently been considered as a fuel, the fundamentals of its combustion have not been investigated in detail. Also it is noted that because of the –OH bond in its molecule, butanol has an electrical conductivity that is substantially higher than that of hydrocarbons and is therefore appropriate for electrostatic atomization. Previous work in these two areas is briefly reviewed in the following

sections. The four butanol isomers are presented in Fig. 1.1 and butanol-1 or normal-butanol is considered for the rest of this study, because this isomer is heavily favored during the production of bio-butanol.

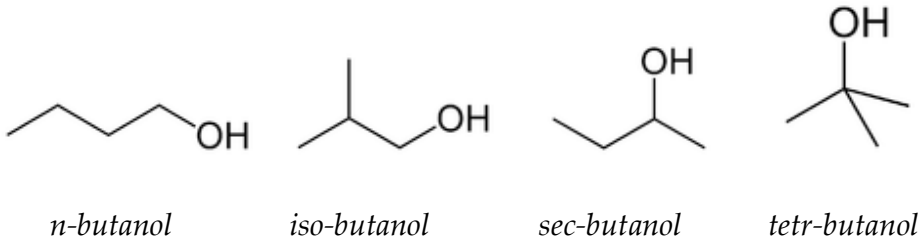

Figure 1.1 Molecular structure of the four butanol isomers

1.2 Previous Related Work

1.2.1 Electrostatic sprays (E-sprays)

The electrospray is an injection system based on electrostatic forces, where atomization is in principle not driven by a substantial pressure difference, unlike common pressure-driven injectors. A picture of the typical electrospray is presented on the right-hand side of Fig. 1.2, and a common schematic of the system producing it, is presented on the left-hand side of the same Figure. A capillary is fed with liquid fuel by a flow controlling pump and on its outer surface high voltage of several kV is applied. The ground electrode is placed on a mesh below the capillary. The electrostatic field is then created between the conductive nozzle and the ground, generating a ligament and ultimately liquid droplets.

For low conductivity liquids, namely hydrocarbons, there is a region of stable electrospray operation, where the formed e-spray consists of three major sections [5,6]. First, the conical meniscus, which is formed at the outer surface of the nozzle and is also known as "Taylor cone" after G.I. Taylor, who first predicted it in 1964 [7]. The Taylor cone is followed by the liquid ligament, which further downstream breaks up due to Rayleigh instability into a spray of nearly uniform size droplets [8-10]. After the droplets are created, they repel each other due to the Coulombic forces generated by the electrostatic field, forming the droplet 'fan' clearly indicated in Fig. 1.1. This mode of operation is also known as the "cone-jet" regime.

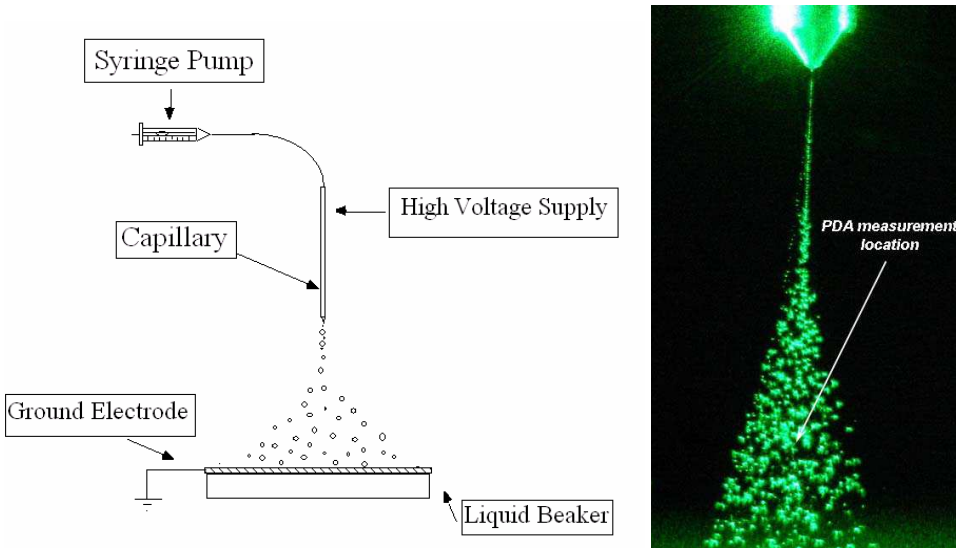

Figure 1.2 Electrospray configuration

It is interesting to notice, that because of the strongly polarized –OH bond butanol is particularly appropriate for the technology of electrostatic and

electrostatically assisted sprays of automotive fuels on which promising results have been recently reported by researchers in the University of Illinois for butanol, gasoline and gasoline-ethanol-mixture sprays [11-15]. This body of work is following up on earlier experimental and computational studies addressing the possibility of electrospray application of the automotive technology [16-19]. The potential of electrostatic effects for combustion applications was pointed out by Thong and Weinberg [20] and shortly thereafter, Kim and Turnbull [21] and Kelly [22] showed that electrical charge can be injected in liquids of relatively low conductivity such as hydrocarbons ($<10^{-6}$ $(\Omega m)^{-1}$) with the use of sharp electrodes.

The fluid mechanics of droplet emission from liquid cones is analyzed in [23]. Gomez and his collaborators at Yale have extensively studied hydrocarbon fuel electrosprays [5,6] and recently proposed a mesoscale burner based on kerosene electrosprays to be used in a "liquid fuel battery" [24,25]. Especially in these studies, two features of the electrospray were highlighted that can be potentially very advantageous for applications that relate to power generation:

a) When operated in the "cone-jet" mode, the electrospray can produce practically monodisperse sprays.

b) The droplet size of the mono-disperse electrosprays can be controlled by the mass flow rate per spray.

The morphology of the electro-sprays was extensively studied by Cloupeau and Prunet-Foch, both in the cone-jet regime and in other functioning modes [26,27].

Different forms of the cone-jet mode are illustrated in Fig.1.3, where it can be seen that the meniscus takes on the form of a cone extended at its apex by a permanent jet whose break-up gives rise to the droplets. For liquids of relatively high conductivities, the cone may have a straight generatrix (Fig. 1.3a) or a curved one (Fig. 1.3b) and when the conductivity is relatively low, the profile of the liquid at the capillary outlet often remains similar to that of a more or less open cone (Fig.1.3.c and d) [27].

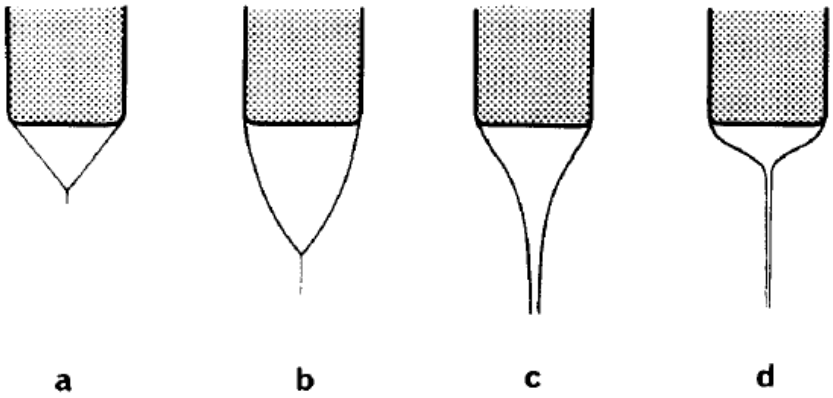

Figure 1.3 Different forms of the meniscus in cone-jet mode: (a) straight generatrix, (b) curved generatrix, (c) and (d) open cone [27]

Except for the cone-jet regime, different modes of electrospray operation appear at different liquid flow rate and applied voltage conditions, as shown in Figure 1.4 [27].

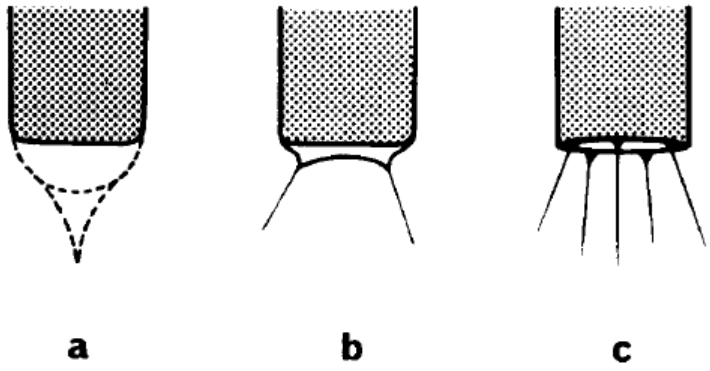

Figure 1.4 Other modes of electrospray operation: (a) Pulsed or intermittent regime, (b) and (c) multi-jet regime [27]

In Fig. 1.4a the *intermittent* or *pulsed* mode is illustrated, where the jet is emitted in a discontinuous way and the apex of the meniscus takes either a pointed or a rounded form. In this pulsed mode, emission phases can occur at perfectly regular time intervals. The diameter of the jet varies during these emission phases, so that the distribution of droplet sizes is never very narrow. In Fig. 1.4b and c the m*ultijet or multicone-jet* mode is illustrated. In this case, the jet may split, with the meniscus forming two or more emissive cusps, the number of which increases with applied voltage.

The jet break-up into droplets occurs as a result of two different instabilities as shown in Fig.1.5 [27].

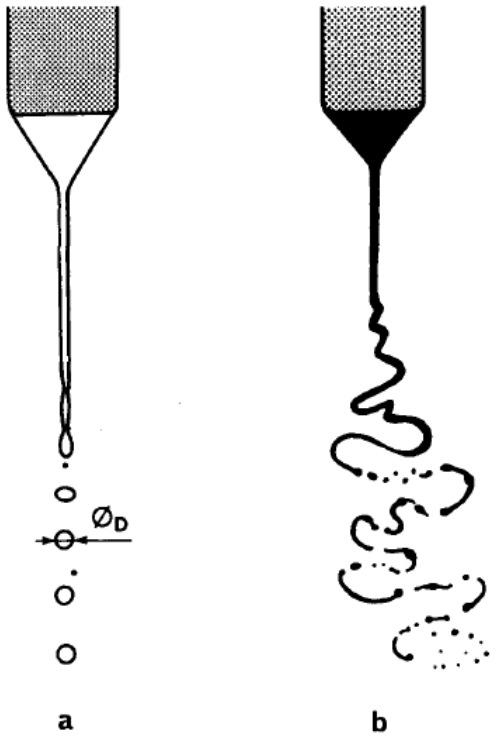

Figure 1.5 Jet break-up into droplets: (a) varicose instability and (b) kink instabilities [27]

First, *varicose* instabilities occur in the same manner as for a neutral jet (Fig. 1.5a) and they can essentially produce uniform-size droplets. In order to do so, it is necessary, as in the case of the uncharged jets, to cause the breakup of the jet at regular intervals by disturbances, the frequency of which is close to the break-up frequency [26]. Second, *kink* instabilities are shown in Figure 1.5b, which usually appear with increasing voltage. In this case, the jet stretches out into disordered winding threads and is thinned out very irregularly. The resulting droplets are of very different sizes.

An overview of the possible morphology of the created e-sprays is shown in Figure 1.6, where cases (a-c) correspond to a *simple* jet, (d, e) to a *ramified* jet and case (f) to *random* spraying [27].

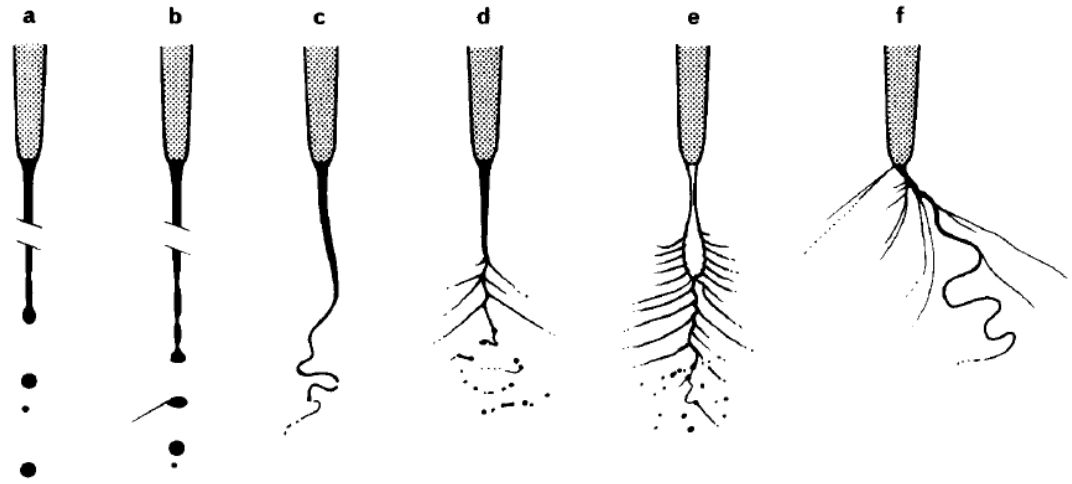

Figure 1.6 Overview of the e-spray morphology: (a, b, c) simple jet, (d, e) ramified jet and (f) random spraying [27]

Even though Figure 1.6 illustrates the observed aspects for ethanol e-sprays from data in [27], these spray morphologies are not restricted to the particular liquid. In Fig. 1.6a, the jet breaks up into large drops possibly accompanied by satellite drops and in

Fig. 1.6b, the large drops are observed as well. In Fig. 1.6c, the jet forms whipping thread before breaking up and in Fig. 1.6d, the jet forms a succession of thickened regions from which one or more fine jets emerge. In Fig. 1.6e, the jet shortly after leaving the nozzle widens and many fine jets are emitted. Finally, in Fig. 1.6f, the steady part of the jet disappears and spraying develops a strongly unstable behavior.

1.2.2Diffusion flames in counter-flow burners

Counter-flow diffusion flames have been investigated in depth due to their ability to represent turbulent flames through models employing laminar flamelets. The interaction of turbulence with reactive flow is a subject of intense research activity. A notion that has proved useful in this context, is the one of the laminar flamelet. Flamelets are thin convective-reactive-diffusive layers embedded within an otherwise non-reacting turbulent flow field. Approaching a turbulent diffusion flame as an ensemble of stretched laminar flamelets was initially presented by Williams [28] and the calculation of means and variances in turbulent flames based on diffusion flame profiles, was suggested by Liew et al. [29]. Additionally, Peters et al. [30-32] published thorough reviews on the diffusion flamelet models stating the validity of the aforementioned approach under the assumption of high Damköhler numbers.

This study is focused on the laminar diffusion flamelet, with the purpose of establishing a fundamental tool for the study of "real world" turbulent environments. Diffusion flame analysis in counter-flow burners dates back in the early '30s when Burke

and Shumman [33] proposed that the combustion of non-premixed fuel and oxidizer streams occurs in an infinitely thin flame sheet where the two meet in stoichiometric proportions. Additionally, their research revealed the need to introduce a parameter independent of chemistry (a conserved scalar), which is the mixture fraction variable Z and is defined as the local ratio of the mass flux originating from the fuel nozzle to the sum of both mass fluxes. Bilger et al. [34] expanded the analysis beyond the infinite thickness of the flame sheet, employing the shifting chemical equilibrium assumption. The thickness of the flame zone in this case, results from the existence of both fuel and oxidizer at the stoichiometric surface due to the occurring reverse reactions.

The structure of diffusion flames in counter-flow burners was presented in detail by Liñán [35], who carried out an asymptotic analysis for a one-step irreversible reaction, first order with respect to fuel and to oxygen, with a large activation energy. Later, Bilger [36] proved that the reaction rate can be related directly to the equilibrium species concentration and the scalar dissipation rate, which represents the inverse of a characteristic diffusion time and is defined as:

$$\chi=2D(\nabla Z)^2 \qquad (1.1)$$

where D represents mass diffusivity and Z is the mixture fraction.

The importance of scalar dissipation rate is highlighted when compared to strain rate. Strain rate is the local velocity gradient and for steady, laminar, counter-flow diffusion flames it can be approximated as [37]:

$$K=\frac{2V_{ox}}{d}\left[1+\frac{V_{fuel}}{V_{ox}}\left(\frac{\rho_{fuel}}{\rho_{ox}}\right)^{\frac{1}{2}}\right] \tag{1.2}$$

For a steady flame, the imposed strain rate K is proportional to the scalar dissipation rate at the stoichiometric surface χ_{stoich} :

$$K \propto \chi_{stoich} = 2D(\nabla Z)^2_{stoich} \propto D/\delta^2 \tag{1.3}$$

In the last equation, δ is the mixing layer thickness which scales as the inverse gradient of the mixture fraction at the stoichiometric surface:

$$\delta \propto 1/\left|\nabla Z\right|_{stoich.} \tag{1.4}$$

Unlike strain rate, the scalar dissipation rate incorporates diffusion effects and therefore provides a better definition for the residence time. Moreover, for non-premixed and partially-premixed flames, it constitutes the determining parameter for the response of chemical reactions to sudden perturbations caused by variations of the turbulent flow field [38]. At the stoichiometric surface of a diffusion flamelet, χ_{stoich}, is proportional to fuel depletion rate [39] and is therefore theoretically expected to control extinction. Interpreting the structure and extinction of unsteady diffusion flames based on the scalar dissipation rate is proven to be more appropriate [40-44] than the traditional strain rate approach.

Kim et al. [45] suggest that the values of stoichiometric mixture fraction (Z_s) encountered most often in diffusion flames of practical interest, are small. A typical schematic diagram of the flow in a counter-flow burner is given in Fig. 1.7, where the

reaction sheet lies far from the stagnation plane in the oxidizer side, as predicted for small Z_s. The reaction sheet is defined as the surface where the two reactants coexist in stoichiometric proportion and is obtained by setting: $Z = Z_s$. According to the definition of the mixture fraction, Z=1 at the inlet of the fuel stream and Z=0 at the inlet of the oxidizer nozzle, on the bottom and on the top of Fig. 1.7 respectively. The stagnation plane is defined as the surface where the two counter-flowing streams meet having zero speeds and its location differs from the one of the flame, which is defined by $Z = Z_s$.

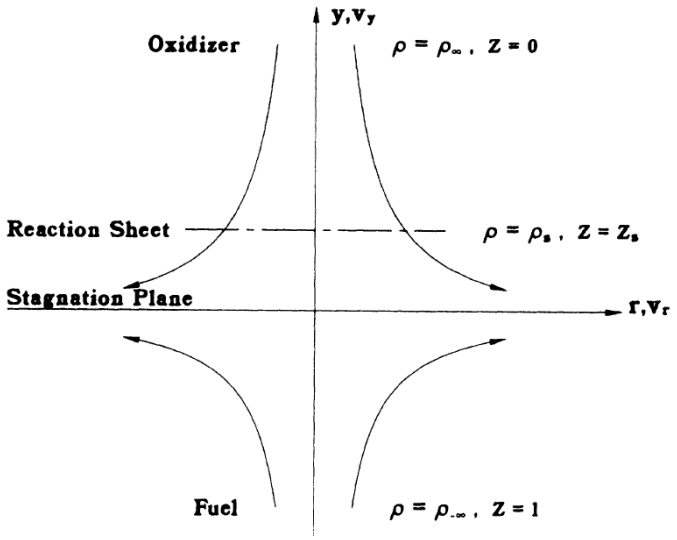

Figure 1.7 Schematic diagram of the flows involved in a counter-flow burner [44]

In closure, published work shows that the diffusion flame is to a large extent a well understood problem. Recent research in this field has focused on the interaction of kinetics and transport for an array of fuels. Methane/air diffusion flames have been studied explicitly by several researchers. Notably, Im et al. [38] focus on unsteady strain

rates, Santoro et al. [41] on emissions production and Bijjula et al. [46] on scalar dissipation rate measurements. Other fuels of experimental interest have been studied namely hydrogen [47], methanol [41] and ethanol [48]. As far as butanol diffusion flames are concerned, Sarathy et al. [49] present numerical and experimental results using a jet stir reactor and a quartz microprobe in the opposed flow case.

1.2.3Butanol combustion processes

Apart from butanol non-premixed flames, research on butanol fuel has been conducted in two related fields, specifically internal combustion engines and chemical kinetic modeling. Internal combustion engine work involving butanol fuel was performed by Alasfour [50,51]. The use of a 30% butanol-gasoline blend as an alternative fuel in a single-cylinder engine was investigated and the experiments showed an increase in first- and second-law efficiencies in the lean region. Gautam et al. [52,53] performed an experimental investigation of combustion characteristics of higher-alcohol/gasoline blends indicating that these blends show a much better resistance to knock.

More recently, Rakopoulos et al. [54] conducted an extended experimental investigation in order to evaluate and compare the use of n-butanol as supplement to conventional diesel fuel at several blending ratios in a DI diesel engine. The tests were conducted at three loads and exhaust emissions were measured. The smoke density was measured to be significantly reduced and the NOx emissions were slightly reduced with

the use of the butanol–diesel fuel blends with respect to those of the neat diesel fuel, with the reduction being higher the higher the percentage of butanol in the blend. The CO emissions were reduced as well, however unburned hydrocarbons (HC) were increased with the use of the butanol–diesel fuel blends. Concerning the engine performance with the butanol–diesel fuel blends against the neat diesel fuel case, with increasing percentage of butanol in the blends, the specific fuel consumption was slightly increased with corresponding slight increase of brake thermal efficiency and a decrease in exhaust gas temperatures.

Also, within 2010, two more butanol-related papers were published in the internal combustion engine area. Dernotte et al. [55] evaluated different butanol-gasoline blends in a port fuel-injection spark-ignition engine, in order to quantify the influence of butanol addition on combustion stability, ignition delay timings and emissions of unburned HC, CO and NOx. According to their work, a B40 blend by volume (40%butanol-60%gasoline) minimized HC emissions, whereas no significant change in NOx emissions was observed. The addition of butanol improved combustion stability, reduced the ignition delay and the specific fuel consumption of the B40 blend was within 10% of that of pure gasoline for a stoichiometric mixture. Szwaja et. al. [56] studied n-butanol-gasoline blends in a spark-ignition engine as well. Stoichiometric air-to-fuel ratios, fixed engine torque, and compression ratios of 8:1 and 10:1 were considered. Among their conclusions they stated that the behavior of n-butanol with

respect to combustion knock was similar to that of 87-octane-number gasoline. This included the sensitivity to spark timing and compression ratio.

The area of butanol oxidation kinetics is today in an embryonic stage and notably, only one mechanism exists in the literature so far. In their work, Dagaut et. al. [57-59], included additional reactions to represent the butanol mechanism on a previously proposed oxidation mechanism [60] for C1–C4 chemistry. The claim was that the oxidation of n-butanol proceeds via unimolecular initiation and hydrogen abstraction reactions. The fuel radical species formed were consumed via unimolecular decomposition and biomolecular reactions. Isomerization of radical species was also included in this model. The rate expression for new reactions derived from tabulations for alkanes and alcohols and the rate constants for reverse reactions were computed from the corresponding forward rate constants and the appropriate equilibrium constants were calculated from thermochemistry.

More recently, Zhang et al. [61] studied the oxidation of butanol and a mixture of n-heptane-butanol in a motored engine, at an equivalence ratio of 0.25. In their analysis they claim that butanol was consumed mainly through H-atom abstraction and among these reactions, the H-atom abstraction from the a-carbon of butanol was particularly favored. In the case of the n-heptane-butanol mixture, butanol oxidation was facilitated at low temperatures through the radical pool generated from the oxidation of n-heptane. Finally, Veloo et al. [62] performed a comparative experimental and computational study of methanol, ethanol, and n-butanol premixed flames. Laminar flame speeds and

extinction strain rates of the flames were measured experimentally and the effect of n-alkane and alcohol molecular structures was investigated on high-temperature flame kinetics. The kinetics model of Dagaut [57] on n-butanol oxidation was used to simulate the experiments. According to their results, laminar flame speeds of ethanol/air and n-butanol/air flames were similar to those of their n-alkane/air counterparts and methane/air flames had consistently lower laminar flame speeds than methanol/air flames. The laminar flame speeds of methanol/air flames were considerably higher compared to both ethanol/air and n-butanol/air flames under fuel-rich conditions.

1.3 Goal and Objectives

The main goal of this work was to investigate the feasibility of bio-butanol as a fuel in terms of both atomization and combustion. This was conducted mainly experimentally, with computational support as far as kinetic calculations were concerned. The effort was focused on three major areas: First, investigate the behavior of bio-butanol electrostatic sprays. Second study non-premixed flames of bio-butanol and third perform research in the field of butanol oxidation kinetics. In more detail, **the specific research objectives** were:

- Examination of the possibility of producing stable electrostatic sprays of butanol, with special reference to operation in the "cone-jet" mode and creation of monodisperse droplets.

- Comparison between butanol, ethanol and heptane electrostatic sprays, as well as determination of the fundamental causes for possible differences.
- Generation of electrosprays of alcohol-containing mixtures with the same electrical conductivity and surface tension but varying composition and study their e-spray behavior.
- Establishment of steady butanol diffusion flames in a counter-flow burner configuration and acquisition of temperature and species concentration measurements, for varying strain rate and overall equivalence ratio, as well as dilution of the fuel and oxidizer streams.
- Establishment of pure butanol flames in the aforementioned configuration and comparative study with other fuels of interest, namely ethanol and methane.
- Investigation of butanol oxidation kinetics through a closed system of varying volume (piston-cylinder assembly) using CANTERA. Two simulations were performed, one considering stoichiometric and one lean combustion (phi=0.7) conditions. Particular emphasis was given in calculating the variation of pressure and temperature, as well as the concentration of major species with time. In addition, mole fractions of certain radicals were calculated. These findings were compared to the corresponding results for ethanol and n-heptane.

CHAPTER 2

METHODOLOGY AND EXPERIMENTAL DESIGN

2.1 Overview of the Experimental Strategy

In order to accomplish the objectives of this research and characterize bio-butanol as a fuel, experimental work was developed in three major fields.

- First, electrostatic sprays of butanol were studied. In order to characterize the morphology of the sprays, optical techniques for measuring droplet size and velocity were employed and spray visualization was performed. Detailed comparison with ethanol and heptane sprays as well as with mixture combinations of the three liquids was conducted and the possibility of monodisperse sprays of butanol was investigated.
- The second area of study was butanol combustion and in particular the establishment of butanol non-premixed flames in a counter-flow burner. Measurements of major species concentration were pursued using Raman spectroscopy and extinction data were collected for a variety of overall equivalence ratios and total heat released. In addition, the possibility of estimating the scalar dissipation rate at the stoichiometric surface (χ_{stoich}) was investigated through a measurement of the mixing layer thickness δ, which

was approximated both through the experimentally measured temperature distribution as well as through the gradient of the mixture fraction at the stoichiometric surface $|\nabla Z|_{stoich}$. Butanol behavior was also evaluated in comparison to fuels widely used; hence, methane, ethanol and butanol-methane flamelets were established.

- As a third field of this study, butanol kinetic modeling was studied in a zero dimensional piston-cylinder assembly and a MATLAB code was used in order to solve the energy conservation and species equations. Pressure and temperature results were provided for two initial conditions as a function of time, along with major and radical species concentrations. Similar results were obtained for ethanol and n-heptane as well.

2.2 Electrostatically-Driven Sprays (Electrosprays)

2.2.1 Electrospray experimental set-up

A schematic of the experimental configuration was presented in Fig. 1.2. The apparatus consisted of a syringe pump that fed the injector with the liquid fuel under consideration and controlled the flow rate. The injector was charged at a potential on the order of several kV provided by a high voltage power supply. The charged spray was collected at an electrical ground in the form of a steel mesh placed several mm from the

capillary exit. The liquid was drained in a liquid beaker placed beneath the electrical ground.

At the beginning of this study, the injector utilized was a steel capillary with an outer diameter of 1.59 mm and an inner diameter of 127 μm and the liquid beaker was placed 11mm below the nozzle exit. The liquid under consideration was pure butanol-1. Butanol has a relatively high electrical conductivity when compared to commercially available hydrocarbons. For this reason, electrospraying was possible without addition of the conductivity enhancers used in [5]. However, the relatively thick steel boundaries of the injector became problematic when the injector tip had to be fabricated. The particular importance of the sharp feature of the injector that was necessary for the generation of a locally intense electrical field was demonstrated by Anderson et al. [12, 13]. Of the techniques available for the tip fabrication, classical machining with a lathe and electrical discharge machining (EDM), failed to create a symmetric and smooth conical surface around the injector-hole in this scale. Thus, the established butanol electrosprays were highly affected by surface roughness, resulting in polydisperse behavior [11].

In order to alleviate the negative effects of surface roughness on the created sprays, commercially available glass capillaries were used as injectors. A layer of silver was applied on their outer surface that acted as a conductor. The capillaries had an outer and inner diameter of 1mm and 30 μm respectively and the distance between the capillary-tip and the ground electrode was set to be 18mm. Sprays of butanol-1, ethanol

and heptane with 2% Stadis 450 as conductivity enhancer were investigated with the use of glass capillaries. The relevant physical properties of these fuels are presented in Table 2.1 [5, 63].

Table 2.1 Physical properties of butanol, ethanol and heptane with 2% Stadis 450

	Electrical conductivity	Surface tension	Kinematic viscosity	Density	Liquid dielectric constant
Liquid fuel	λ (1/Ωm)	σ (N/m)	ν (m^2/s)	ϱ (kg/m^3)	ε
Butanol	2.300E-04	2.493E-02	3.143E-06	809.5	17.84
Ethanol	5.500E-04	2.197E-02	1.361E-06	789.3	25.3
Heptane with 2% Stadis 450	6.700E-06	1.870E-02	6.260E-07	679.5	1.91

Additionally, three mixture combinations of the aforementioned pure fuels were considered (conductivity enhancer Stadis was not added to heptane), which had the same surface tension and electrical conductivity. Each mixture contained two substances. The composition, as well as the calculated physical properties of the created mixtures, are presented in Table 2.2.

Table 2.2 Compositions and calculated physical properties for mixtures 1, 2 and 3

	Butanol	Ethanol	Heptane	Electrical conductivity	Surface tension	Kinematic viscosity	Density
	(% per volume)			λ (1/Ωm)	σ (kg/s^2)	ν (m^2/s)	ϱ (kg/m^3)
Mixture 1	0.48	0.52	0.00	4.311E-04	2.330E-02	1.908E-06	7.99E+02
Mixture 2	0.45	0.00	0.55	4.311E-04	2.333E-02	1.248E-06	7.38E+02
Mixture 3	0.00	0.70	0.30	4.338E-04	2.331E-02	1.335E-06	7.56E+02

The mass fraction of each pure substance in the mixture was selected such that the resulting mixtures had the same electrical conductivity λ and surface tension σ. The

importance of these two parameters for the electrospraying technology is developed in Chapter 3 and the detailed list of formulae, is presented in the following section, (2.2.2).

2.2.2 Calculation of electrical conductivity and surface tension of the mixtures

In order to calculate the electrical conductivity of a mixture, the concept of the mobility u of an ion was used, as introduced in [64]:

$$u = \frac{z \cdot e}{6 \cdot \pi \cdot \mu \cdot a} \tag{2.1}$$

where $z \cdot e$ is the charge of an ion, μ is the dynamic viscosity and a is the molecular radius, which is calculated through [64]:

$$2a = d = \sqrt{\frac{2}{3\mu}\sqrt{\frac{k \cdot T \cdot MW}{N_A \cdot \pi^3}}} \tag{2.2}$$

where d is the molecular diameter, k is the Boltzmann's constant, N_A the Avogadro's number and T the temperature. The dynamic viscosity μ was approximated using the method of Grunberg and Nissan [65] for a binary mixture:

$$\ln \mu_m = x_1 \ln \mu_1 + x_2 \ln \mu_2 + x_1 x_2 G_{12} \tag{2.3}$$

where G_{12} is the binary interaction parameter, given in eq. 2.4, where the intermediate parameters $\Sigma\Delta$, W and N for the two mixture components i and j, are obtained from tables in [66]:

$$G_{12} = \Sigma\Delta_i - \Sigma\Delta_j + W \tag{2.4}$$

$$W = \frac{0.3161 \cdot \left(N_i - N_j\right)^2}{\left(N_i + N_j\right)} - 0.1188 \cdot \left(N_i - N_j\right) \quad (2.5)$$

For each mixture, *i* was selected using priority rules in [66] and *j* became the second mixture component. The values of G_{ij} for the three mixtures, along with the intermediate parameters from equations 2.4 and 2.5, are given in Table 2.3. *Ni* is the number of carbon atoms in *i* and $\Sigma\Delta$ was calculated based on the contributions of a group of bonds in the molecule. For example: $\Sigma\Delta_{-CH3} = -0.100$ and $\Sigma\Delta_{-CH2-} = 0.096$.

Table 2.3 Gij values and intermediate calculated parameters

	MIXTURE 1		**MIXTURE 2**		**MIXTURE 3**	
	i: Butanol	j: Ethanol	i: Butanol	j: Heptane	i: Ethanol	j: Heptane
$\Sigma\Delta$	-0.255	-0.027	-0.255	0.28	-0.027	0.28
N	4	2	4	7	2	7
W	-0.027		0.615		1.472	
Gij	-0.255		0.08		1.165	

After calculating the mobility through eq. 2.1, the electrical conductivity of the mixture under consideration is given by:

$$\lambda = z \cdot e \cdot u \cdot N_A \quad (2.6)$$

In order to calculate the surface tension of the mixtures the Macleod-Sugden correlation was used [67]:

$$\sigma_m^{1/4} = \sum_{i=1}^{n} [P_i] \cdot \left(\rho_{Lm} x_i - \rho_{vm} y_i\right) \quad (2.7)$$

In the last equation *Pi* is an intermediate term called the Parachor and its value was obtained from tables in [66]. In these tables, the structural contributions for each

bond group in the molecule are found. For the three liquids under consideration: [$P_{BUTANOL}$] = 205.3, [$P_{ETHANOL}$] = 125.3 and [$P_{HEPTANE}$] = 311.0.

In addition, x_i and y_i is the mole fraction of i in liquid and vapor phases, whereas ρ_{Lm} and ρ_{vm} are the liquid-mixture and the vapor-mixture density respectively. The density of the vapor term was neglected and the equation reduced to:

$$\sigma_m^{1/4} = \rho_{Lm} \sum_{i=1}^{n} \left(\frac{x_i \cdot \sigma_i^{1/4}}{\rho_{Li}} \right) \tag{2.8}$$

2.2.3 Droplet size and velocity measurements – Phase Doppler Anemometry (PDA)

For spray droplet size and velocity measurements, a Dantec Fiber Phase Doppler Anemometer (PDA) was used. It was powered by a 5W Ar-ion laser and was run in 1-D PDA mode at 514.5 nm and a 71.4° forward scattering angle. In the PDA software, the refractive index for butanol, ethanol and heptane was set to 1.3988, 1.3611 and 1.3855 respectively [63] and for the mixtures to 1.38. For the electrosprays established with the steel capillaries, a number of 10,000 data points was selected. However, due to the steady nature of the sprays, a number of 1,000 counts was sufficient for adequate statistics and it was applied to all spray cases with the glass injectors, avoiding high collection times. Droplet size and velocity measurements were performed at a location on the central spray axis 5mm and 10mm from the steel and glass capillary exit respectively. The collection point location is shown in Fig.1.2, of the introduction part.

Droplet size measurements were obtained at only one location, since the goal remains to investigate the possibility of monodisperse sprays for the liquids under consideration.

2.2.4 Electrical conductivity measurements

In order to characterize precisely the electrical properties of butanol fuel and to examine the deviations observed from previously published electrospray results, measurements of the electrical-conductivity of butanol were performed with the apparatus shown in Fig. 2.1. A plastic tube of an internal diameter equal to 5.1mm and a length equal to 27.4 cm was filled with butanol and charge of 2-7kV was applied by a high voltage supply. The current through the butanol tube was measured using a Keithley 6485 picoamperometer. An additional resistor R_1 = 4 MΩ was connected in series with butanol to prevent short-circuits that would damage the picoamperometer.

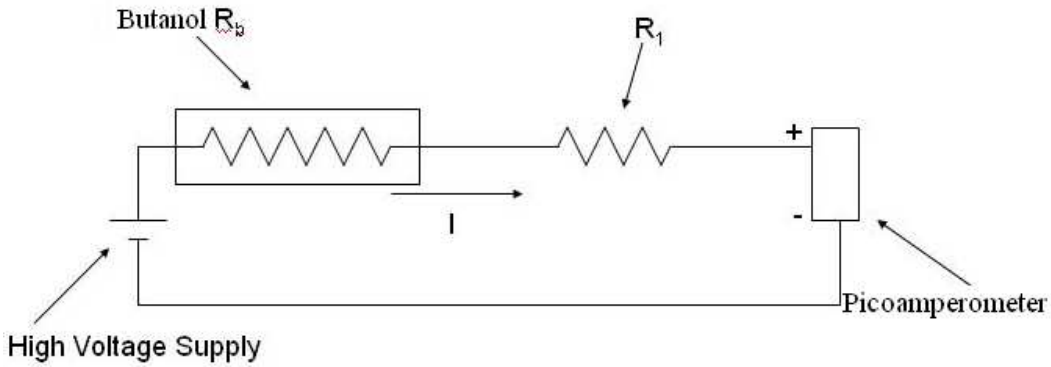

Figure 2.1 Experimental setup for butanol electrical conductivity measurements

In the simple circuit of Fig. 2.1, the applied voltage V and the current I measured by the picoamperometer, are correlated through:

$$\frac{V}{I} = R_b + R_l \tag{2.9}$$

In the last equation R_b was the resistance of the butanol-filled tube. The resistance of the plastic tubing was established to be so large that was reasonable to assume that the resistance of the tube was only due to the resistance of the butanol it contained. In such a case, if l is the length and S is the cross-sectional area of the tube, the electrical conductivity λ of butanol was determined by the relation:

$$R_b = \frac{1}{\lambda}\frac{l}{S} \tag{2.10}$$

2.2.5 Visualization techniques

Imaging of the butanol electrosprays established with the steel capillaries was performed with a Canon EOS Digital Rebel camera. The camera was placed directly in front of the spray, mounted on a level tripod. Zoom and focus were both manually adjusted, with the zoom set to maximum (5.6x). The focal length of the lens was 55 mm and the aperture was set to *f*/4.5. An Nd-YAG laser operating at 532 nm and delivering approximately 3.1 mJ/pulse was used as an illumination source and its beam was directed toward a doublet of a -500 mm concave spherical lens and a 300 mm cylindrical lens that was used to generate a laser sheet. To eliminate the need for precise camera

timing, the camera exposure time was set to the inverse of the laser firing frequency. The laser was pulsed at 10 Hz so the camera exposure time was set to 100 ms.

For all sprays created with the glass injectors, imaging was provided by a Vision Research Phantom v7.0 unintensified CCD high-speed video camera. Three Nikon extension tubes totaling 82.5 mm in length were used to increase magnification along with a Tiffen 52 mm zoom lens. Camera exposure time was set to 96 μs and the zoom and f-stop settings were adjusted to provide a clear view of the entire spray. Laser light from an Oxford Laser Systems LS 20-50 Copper-Vapor laser operating at 510.6 nm and having a frequency of 10 kHz was directed toward the doublet of the concave spherical – cylindrical lens that was used to generate the laser sheet. Both the high speed camera and the laser were synchronized by the Berkeley Nucleonics 500C042 pulse generator. To acquire images of a 2-D cross section of the spray, the created laser sheet was aligned so that the top would be directly below the capillary tip and the bottom would be approximately 20 cm below the orifice, so that the whole spray was captured. The thickness of the laser sheet was approximately 1 mm.

2.3 Counter-flow Flames

2.3.1 Experimental counter-flow burner

An axisymmetric, laminar, fuel-oxygen diluted flame was established in the counter-flow burner configuration of Fig.2.2.

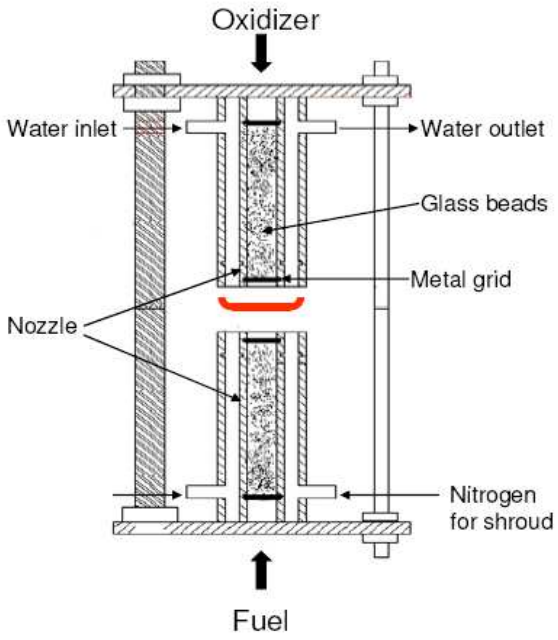

Figure 2.2 Cross-sectional area of the counter-flow burner

Liquid (butanol-1, ethanol) and gaseous (methane) fuels were metered separately on the bottom part of the burner. The oxygen stream was nitrogen-diluted and fed into the burner from the top, whereas a nitrogen shroud was used in order to isolate the flame from interference with the surrounding air. Fine grids and glass beads were used to achieve uniformity of the velocity profiles of the reactants at the nozzle exits. The diameter of the nozzles was 12.5 mm, and the gap between them was 15 mm. Liquid fuel flow rate was controlled by a Kd-Scientific 780100 syringe pump that fed a 4.5 mm diameter, 1m long, electrically heated copper tube. The tape was heated to 170^0C to assure liquid fuel vaporization. Gaseous streams were controlled with flow-meters. Both liquid and gaseous fuel streams were nitrogen-diluted before mixing (when needed) at

the inlet of the counter-flow burner. The outside surface of the burner lower section was also wrapped with heating tape and its temperature reached 220^{o}C.

2.3.2 Raman spectroscopy

2.3.2.1 Spontaneous Raman scattering

Spontaneous Raman scattering is an incoherent process and as such, a single laser beam interacts with the molecules of the species along its path, generating a scattered signal. A fraction of the resulting signal is collected by the optics system over some solid angle Ω. The electrical field E of the incident electromagnetic wave induces on the dipole a dipole moment P, the expression of which depends on the type of the scattering process. The phenomenon where the photons of light are scattered by the medium without energy exchange is called Rayleigh scattering and is presented on the left of Fig.2.3. Raman scattering is inelastic scattering of light by molecules and can be distinguished in Stokes and Anti-Stokes Raman. The absorption and subsequent emission of a photon via an intermediate electron state, that constitutes the Raman effect, is shown in the same Figure. Stokes scattering occurs when the molecule absorbs energy and the resulting photon of lower energy generates a Stokes line on the red side of the incident spectrum. In the case that the molecule loses part of its initial energy, anti-Stokes Raman occurs. Then, incident photons are shifted to the blue side of the spectrum, thus generating an anti-Stokes line.

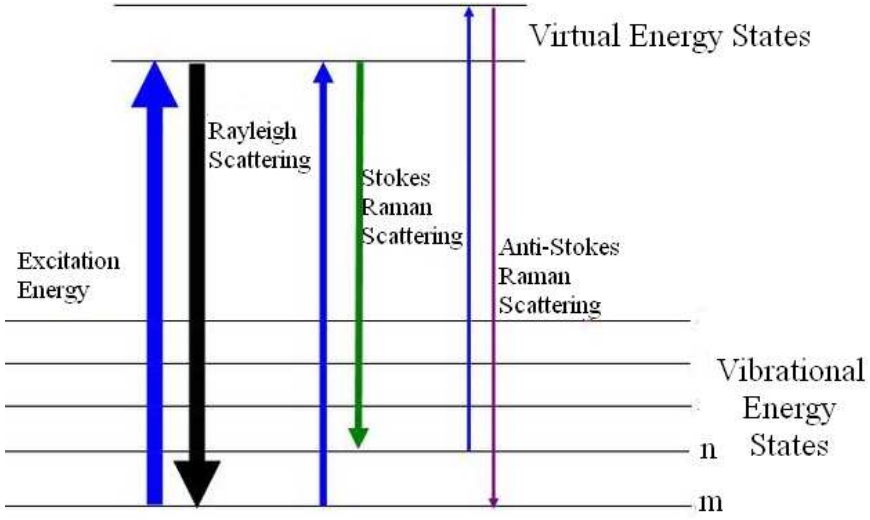

Figure 2.3 Schematic of elastic (Rayleigh) and inelastic (Raman) scattering

Anti-Stokes Raman is weak for temperatures below 1000K and as a result Stokes Raman will be considered further in this study. The excitation of a molecule due to collisions takes place from a vibrational state E_m to some "virtual" energy state and then it decays back to a vibrational state E_n. The energy of the incident photon $h\nu_o$ is capable of causing this excitation only if the following inequality is satisfied [68]:

$$h\nu_o \succ E_m - E_n \tag{2.11}$$

The energy of Raman scattered light E_s collected in a collection solid angle Ω is given by [68]:

$$E_s = E_o \cdot n \cdot \frac{\partial \sigma}{\partial \Omega} \cdot \Omega \cdot l \cdot \varepsilon \tag{2.12}$$

In this last equation, E_o is the energy of the incident light, l is the sampling length along the beam and n is the number density of scatterers, in our case the molecules of the gas under consideration. The collection efficiency is accounted by the term ε and

$\frac{\partial\sigma}{\partial\Omega}$ constitutes the differential Raman cross-section. The last term is a function of the polarization of the incident light, as well as of the angle of observation and is measured experimentally over a range of vibrational frequencies and temperatures.

The Raman lines in the scattered light spectrum vary with the wavelength of the light source but, as shown in Fig. 2.3, the shift from the excitation is independent of incident light wavelength and characteristic for every substance [69]. Equation 2.13 presents the relation between the incident λ_o and the resulting λ_s wavelength for a certain Raman shift, that is for a certain species.

$$\text{Raman Shift } (\text{cm}^{-1}) = \frac{1}{\lambda_o} - \frac{1}{\lambda_s} \tag{2.13}$$

For an excitation source of 532 nm, the wavelengths λ_s where the several major species under consideration were detected are presented in detail in Table 2.4 of the following section.

2.3.2.2 Major species concentration measurements

Major combustion species (C-H bond, O_2, N_2, CO_2 and H_2O) were measured using line Raman imaging. A schematic of the experimental set-up is presented in Fig. 2.4. A Quanta-Ray Pro-250 Nd-YAG laser delivering 300 mJ/pulse at 532 nm was used as an excitation source and the Stokes-shifted Raman signal was collected at the wavelengths shown in Table 2.4. It is noticeable that, for an incident laser beam wavelength of 532 nm, all three pure fuels have a detection wavelength around 629nm,

thus this is the wavelength selected in order to detect the C-H bond in the fuel-mixture cases (Row 4 of Table 2.4). The laser beam was focused to an approximately 500 μm thick and 60mm long horizontal line with a 1m plano-convex lens.

Table 2.4 Raman signal for the species under consideration

Species	Wavelength [nm]
C_4H_9OH	628
CH_4	629.7
C_2H_5OH	630.2
C-H bond	629
O_2	580
N_2	607.3
CO_2	571
H_2O	660.3

An Acton Research 300 mm imaging spectrograph was used for the dispersion of Raman signals. Dispersion was achieved with a 68mm x 68mm ruled grating with 1200 grooves/mm and a 500 nm blaze wavelength. The spectral images were captured using an Andor I-star ICCD which was coupled to the spectrograph using the flanges provided on the camera and the spectrograph. The horizontal images from the flame were rotated by 90° by a dove prism so that they were in-line with the vertical entrance slit of the spectrograph. The images were then focused onto the inlet mirror using a Nikon 50mm, f#1.8 lens. An OG550, 3mm thick glass filter was used to reject stray reflections from the burner hardware. The synchronization between the Nd-YAG laser and the Andor ICCD camera was controlled by a Stanford Research Systems DG-535

delay/pulse generator. The burner was mounted on a vertical translation stage so that the flame was scanned in the vertical direction.

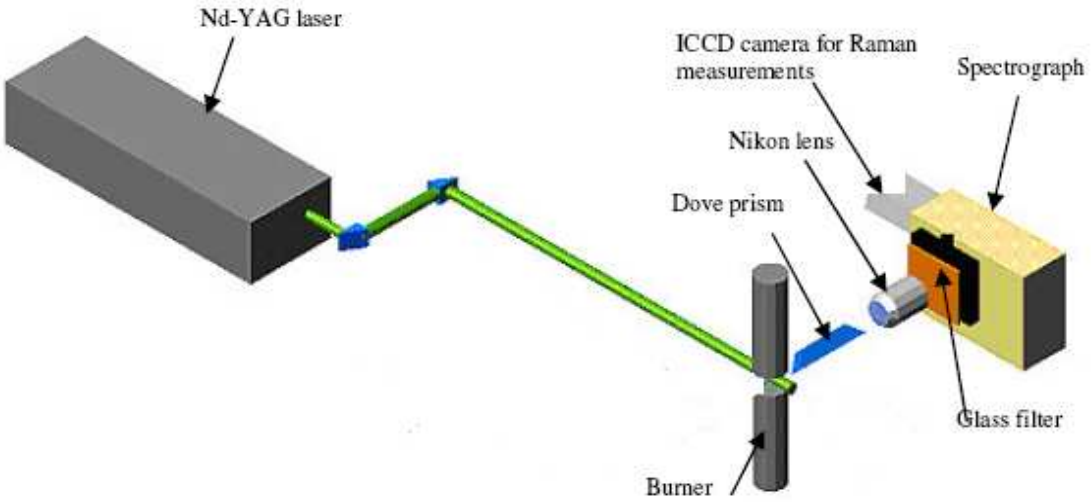

Figure 2.4 Experimental set-up

The beam was first focused at a point 7.5mm above the lower nozzle along the central axis of the tubes, where the center of the gap between the nozzles was located. When the Raman line-images were captured for this certain location, the translation stage was moved up and down in 1mm intervals along the vertical axis. For each measurement three sets of 300 Raman lines were averaged that were integrated on the chip, in order, to achieve an acceptable signal-to-noise ratio (S/N > 10).

2.3.3Flame temperature

Temperature measurements were obtained with a K-type thermocouple of 0.50mm diameter, with an increment of 1mm, starting from the fuel nozzle exit until the

whole gap between the nozzles was scanned. This was achieved with a translational stage. The thermocouple was positioned perpendicular to the burner axis, with its edge at the center of the inner annulus of the burner. The maximum temperature of the thermocouple was rated for 1473 K and the maximum flame temperature observed was 1382 K.

2.4 Kinetic Modeling

An adiabatic closed system of varying volume (piston-cylinder assembly) was considered in order to perform zero-dimensional kinetic modeling calculations of butanol and compare its combustion with the one of ethanol and n-heptane in a computational set up that resembles engine combustion. Air was used as oxidizer and the two reactants were considered to be premixed at the beginning of the cycle. No external ignition source was considered and combustion was initiated through autoignition. The compression ratio was 20:1 and the reactants were at a pressure of 0.8 atm and preheated to 350K at the beginning of the compression stroke. Two combustion simulations were performed in this analysis; one for stoichiometric and one for lean combustion of the three fuels. (ϕ = 0.7)

The code used for the simulation was in MATLAB and imported the kinetic mechanism files of the each one of the three fuels through the CANTERA software. The mechanisms of ethanol and heptane, [70, 71] respectively, were provided through Lawrence Livemore National Laboratories. The ethanol mechanism contained 50 species

and 383 reactions. It should be noted that for the n-heptane calculation, the reduced mechanism was used, with 44 species and 114 reactions. Butanol kinetic mechanism has recently been proposed in [57] and it contained 87 species and 884 reactions.

The two fundamental pathways that the initial reactions of an alcohol can follow are either H-abstraction by H, O and OH or, when active species are not available for the attack of the alcohol, the initiation is achieved due to high temperatures ~ 1000 K (unimolecular decomposition). In the first case, the attacked alcohol forms an intermediate oxygenate species, typically an aldehyde, whereas in the second case, ethene is considered to be the major intermediate species. In order to conclude which path is followed in the case of butanol, Dagaut at al. [57] proposed the kinetic mechanism, after performing an investigation for three sets of conditions.

First, for n-butanol oxidation in a stirred reactor at: P =10 atm, T=1000K, the model suggested that n-butanol was consumed primarily via H-atom abstraction from the a, b, and c carbon atoms, with each pathway accounting for approximately 22% of the total n-butanol consumption. The next most dominant pathway was H-atom abstraction from the hydroxyl group, which accounted for nearly 20% of n-butanol consumption. H-atom from the d carbon atom accounted for nearly 14%, while all the unimolecular decomposition pathways combined accounted for less than 0.5% of n-butanol consumption. Unimolecular decomposition accounted for less than 4% of n-butanol consumption and hence, it was reasonable to conclude that n-butanol consumption was dominated by H-atom abstraction.

Second, for a pressure of 1 atm and the same experimental set-up, H-atom abstraction was responsible for consuming more than 60% of the *n*-butanol, with H atoms (29%) and OH (57%) radicals being the main contributors. Over 35% of the initial *n*-butanol went to form CH_3CHO, C_2H_5 radical, C_3H_6, and CH_2OH radical, while over 40% led to the formation of 1-C_4H_8. Most of the 1-C_4H_8 broke down to form C_3H_6 via the aC_3H_5 radical. Unimolecular decomposition reactions became more important as the equivalence ratio was increased from ϕ = 1.0, but H-atom abstraction reactions were still predominant.

Finally, a third model was developed for butanol oxidation in the opposed flow diffusion-flame case and for three temperatures. For the low temperature, H-atom abstraction accounts for the nearly 100% of the fuel consumption, with abstraction being dominated by H atoms (43%), OH radicals (22%), CH_3 radicals (11%), and C_3H_5 radicals (9%). At the intermediate temperature, T = 1170 K, fuel consumption was dominated by H-atom abstraction reactions (70%) by H atoms (55%) and OH radicals (25%). The fuel radicals formed via H-atom abstraction were primarily consumed via β-scission. At the low temperature condition, over 60% of the initial fuel formed CH_3CHO, C_2H_5 radical, C_3H_6, and CH_2OH radical. Another 38% formed C_3H_7CHO, 1-C_4H_8, H atoms, and OH radicals. At the intermediate temperature condition, H-atom abstraction reactions were predominant. Then, at high temperatures, H-abstraction reactions were negligible and the energy was available to activate unimolecular decomposition reactions. However,

the amount of fuel that reached these conditions was small, and therefore these reactions did not contribute significantly to the formation of product species.

CHAPTER 3

ELECTROSTATIC SPRAYS OF BUTANOL AND BUTANOL-CONTAINING MIXTURES

Butanol is particularly appropriate for the technology of electrostatic atomization due to the –OH bond in its molecule, which, under an electrostatic field of elevated intensity, gets polarized, converting butanol into a relatively conductive molecule. The electrical conductivity, is one of the controlling properties in the formation of the e-spray and is connected to the Coulombic forces that will atomize the liquid. The electrospray forms as a result of the competition between these Coulombic forces with the cohesive forces acting on the surface of the liquid, because of surface tension. Thus, surface tension constitutes the second fundamental property for the creation of an electrospray. Other properties, namely viscosity and density play a secondary role in the e-spray formation and are also considered in the sections that follow.

In more detail, in this chapter, electrostatic butanol sprays were established and their behavior was studied and compared with other fuels of automotive interest. For that purpose, three particular tasks were performed:

- First, spray visualization was performed through high-speed imaging as well as with digital photography. Butanol electrospray phenomenology was investigated for a variety of conditions and is compared with the corresponding electrosprays of ethanol and heptane. Moreover, three

mixtures of the three fuels were generated, that had the same electrical conductivity and surface tension and imaging of their e-spray morphology was presented as well.

- For all e-sprays of pure fuel and their mixtures, droplet size and velocity measurements were pursued. E-spray structure was studied using Phase Doppler Anemometry and particular emphasis was given on the effects of fuel flow rate and applied electrical field.
- The combined analysis in terms of phenomenology and structure revealed several modes of operation for the established sprays. A stable electrospray regime was observed for low flow rates of butanol, triggering a quest for the non-dimensional parameters that characterize these sprays. An empirical expression correlating the dimensionless average diameter d*, flow rate Q* and applied voltage V* was achieved with a high degree of accuracy.

3.1 Electrospray Phenomenology

3.1.1 High-speed visualization of electrosprays of butanol, ethanol and heptane

Butanol electrospray imaging results are shown in Fig. 3.1 for flow rates 5ml/hr-35ml/hr with an increment of 5ml/hr and voltages 4, 5 and 6kV. Visualization results for ethanol and heptane with 2% Stadis are presented in Figs. 3.2 and 3.3 respectively, for

flow rates 10ml/hr-35ml/hr and voltages 4, 5 and 6kV. Each of these images was selected to be characteristic of the particular spray-movie it described, since in most of the cases the spray was unsteady. In the majority of the cases, the videos revealed a periodicity in spray behavior and the images correspond to the screenshot when most details of the spray structure were apparent. For clarity reasons, these Figures are presented in the end of this paragraph, after the corresponding discussion.

For butanol and an applied voltage of 4kV, a stable meniscus was observed only when operating at the lowest flow rate of 5ml/hr. At 10ml/hr a mild oscillation of the meniscus was observed in the direction of the capillary, which became more intense as increasing the flow rate further from 20ml/hr. Despite the oscillations, the spray operated in an intermittent regime with a single ligament and the emission phases occurred at perfectly regular time intervals as predicted in [26], with a periodicity of around 200Hz.

At higher flow rates (30-35ml/hr), the pulsed jet was, in addition, swinging around the vertical direction and slight kink instabilities started to appear. It is possible that these instabilities occur when the largest droplets have a charge which exceeds the Rayleigh limit charge [72]. This is the limit above which the Coulombic force due to the charge on a droplet exceeds the binding force due to surface tension and the droplet disrupts. The Rayleigh limit is calculated and discussed explicitly in section 3.3.1. As a result of kink instabilities, the jet was stretched out into disordered winding threads and

was thinned-out very irregularly. A different operating mode was observed though at 15ml/hr, where a meniscus break-up generated a multi-jet.

As the voltage increased to 5kV, a time-independent spray was observed for low flow rates (5-15ml/hr). Five emissive cusps were observed for 10ml/hr and 15ml/hr and a single one for 5ml/hr. Above 20ml/hr, meniscus oscillations started appearing, with increasing spray swing around the vertical direction with flow rate. The spray was continuous, not intermittent, however kink instabilities were present. For slightly higher voltages lateral kink-instabilities would appear according to [27], however no discussion was made on the effect of flow rate, the increase of which, increased the spray "swing" around the vertical direction. These instabilities, along with intense spray oscillations around the vertical direction, were observed for the highest flow rates (30-35ml/hr) at 6kV, as well. For lower flow rates, at 6kV, all sprays were operating in the multi-jet regime.

For ethanol and flow rates of 10, 20 and 30mlhr, droplet formation was due to kink instabilities and the menisci were highly oscillating in a deformed droplet form. The spraying was continuous and random and the fan of the atomized droplets was substantially broad. The meniscus oscillating period increased with increasing voltage for all cases and it was calculated to be around 385Hz for 4kV, 750Hz for 5kV and 1250Hz for 6kV. At higher voltages, the steady ligament of the spray disappeared and several emissive cusps were present, rotating around the capillary tip. In the same figure, it is shown that for 15, 25 and 35ml/hr, an initial non-atomized jet was apparent

in all cases, except for the multi-jet regime, and the fan of droplets was narrow. The spraying was pulsed, with oscillating menisci and the jets were ramified; that is, the jet formed a succession of thickened regions from which one or more fine jets emerged [27]. Similar to what observed earlier, the oscillations became more intense with increasing flow rate.

Heptane with 2% Stadis sprays are presented in Figure 3.3 and they adopt several of the unstable operating regimes described in the earlier paragraphs. At 4kV and low flow rates (10-15ml/hr), continuous oscillating sprays at the direction of the capillary, are present. As the flow rate increases, kink instabilities generate an intense flailing motion of the jets. For higher voltages, at both 5kV and 6kV, random spraying results the multicone-jet menisci.

For all three liquids, the high-speed movies revealed that no steady "cone-jet" sprays were established. The observed unsteady nature of the sprays was connected, in most of the cases, with menisci oscillations, resulting in either continuous or pulsed jets. In addition, it is reminded that in the cone-jet regime, the spray break-up occurs due to Rayleigh instabilities on the liquid ligament that is extracted from a conical meniscus, resulting in uniform size droplets. However, in most of the presented data, kink instabilities took place, where the liquid came out of a rounded or a deformed meniscus, that created a series of disordered threads, resulting to non-monodisperse sprays. Thus, the source of the unsteady spray morphology should be sought in the region of the meniscus apex and on the way it forms. For that reason, in section 3.1.2 that follows, a

particular emphasis is given in the shape of the spray meniscus and time-dependent movies are provided with focus in that region.

Another reason of establishing e-sprays in different regimes than the cone-jet, could be the combination of flow rates and voltages applied. It is noted that the popular cone-jet mode is not easy to establish [5, 6, 27] and typically requires varying the above parameters with a refined increment while experimenting. It is therefore conceivable that the cone-jet regime is "missed" while varying the experimental parameters. For that reason, butanol low flow rates are investigated in section 3.1.3 in the range of 1ml/hr-4.5ml/hr and movies are provided for small applied voltages (in the voltage region where e-sprays start appearing, also known as "onset voltage").

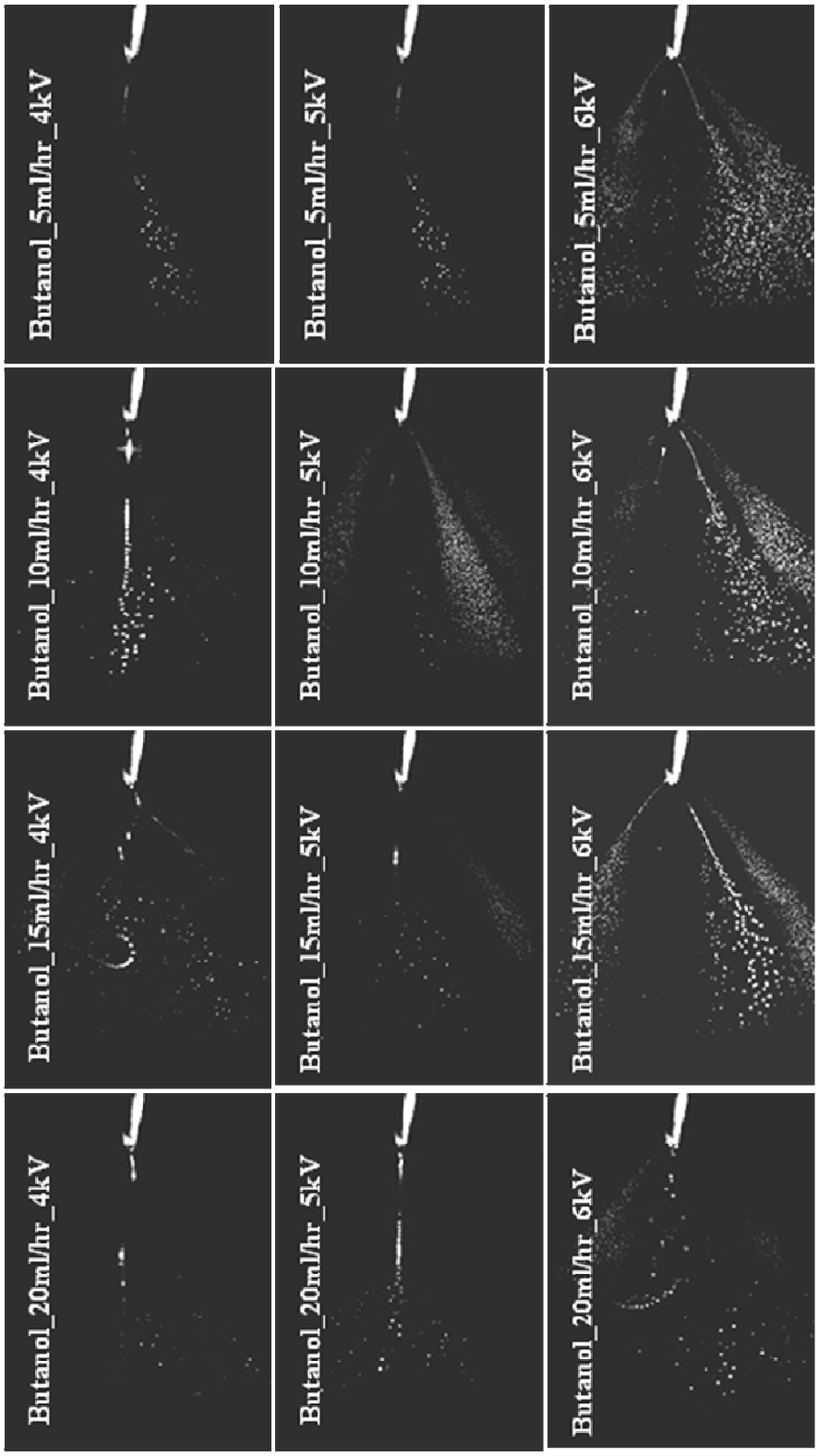

Figure 3.1 (cont. on next page)

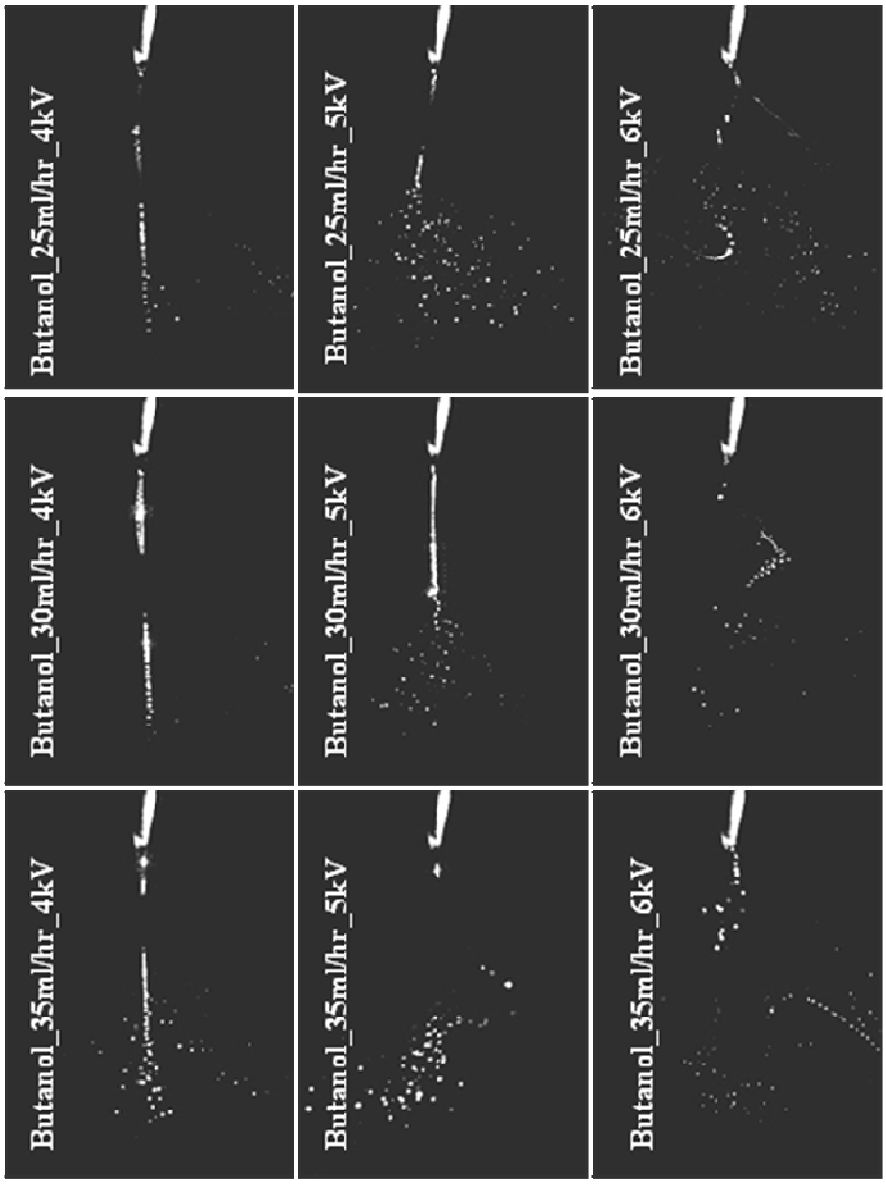

Figure 3.1 Electrospray imaging results for Butanol

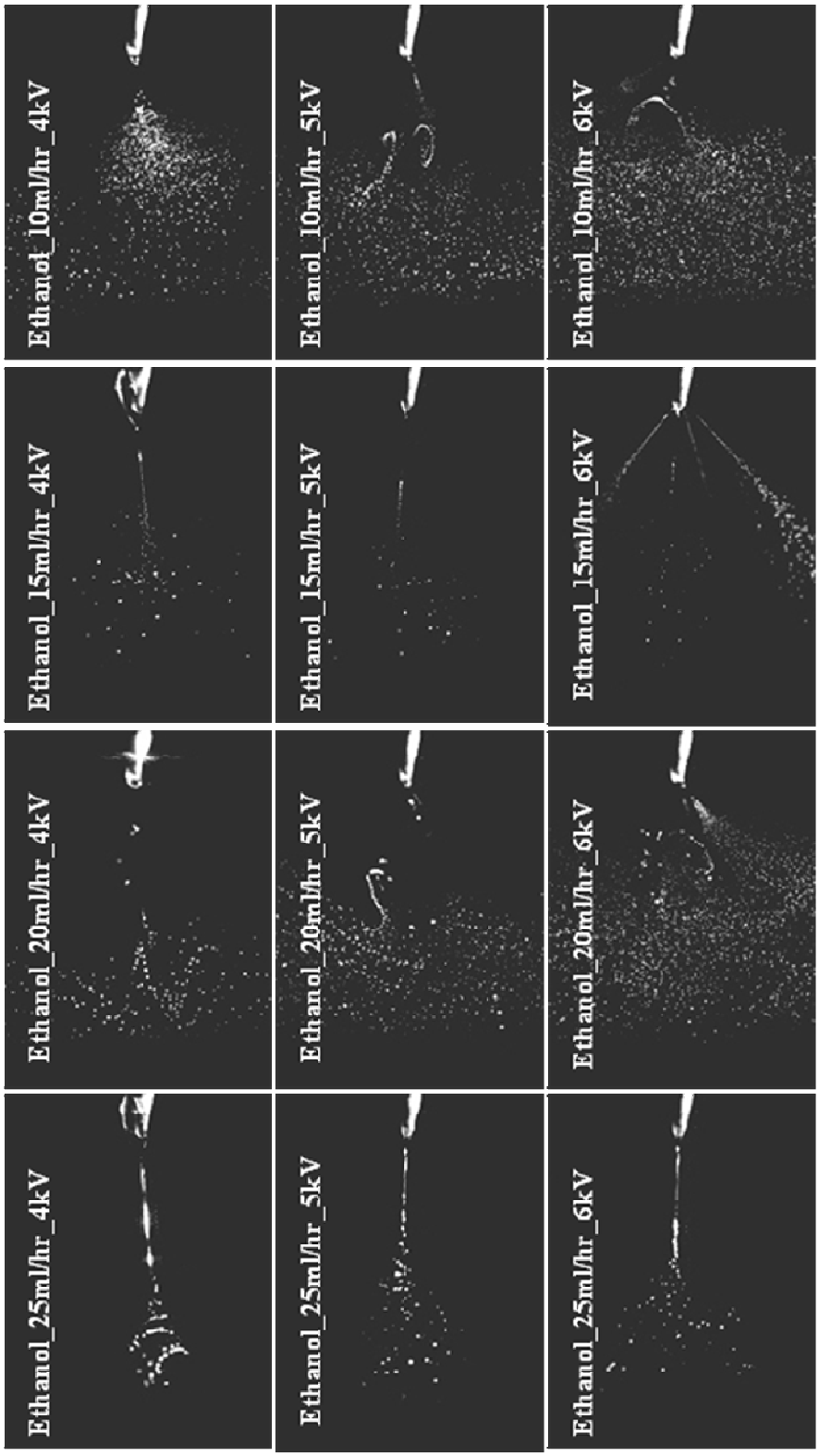

Figure 3.2 (cont. on next page)

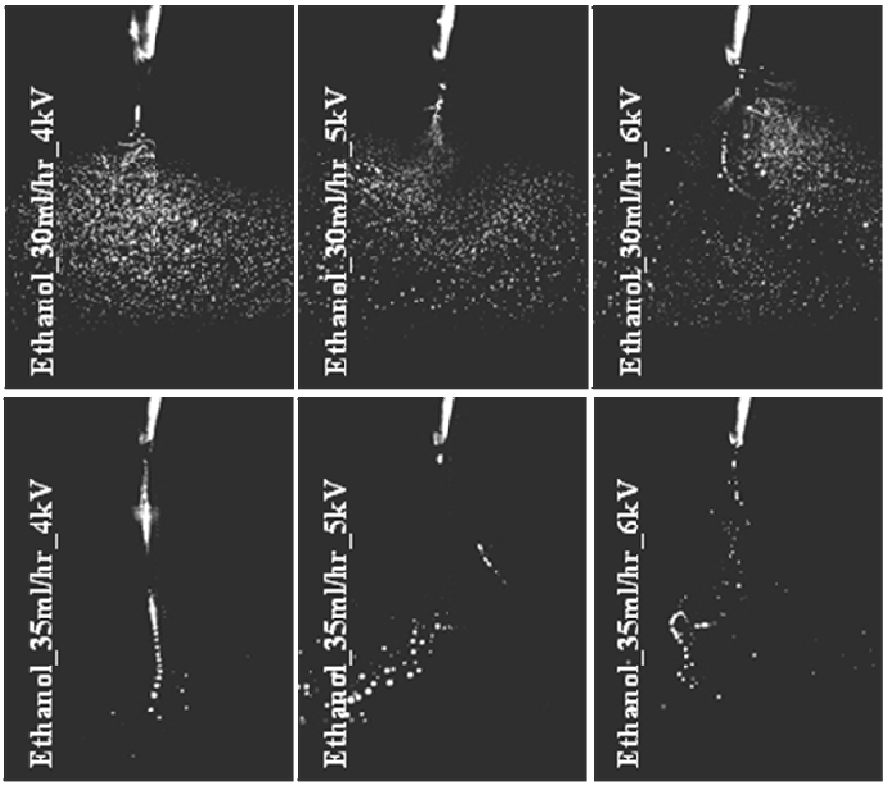

Figure 3.2 Electrospray imaging results for Ethanol

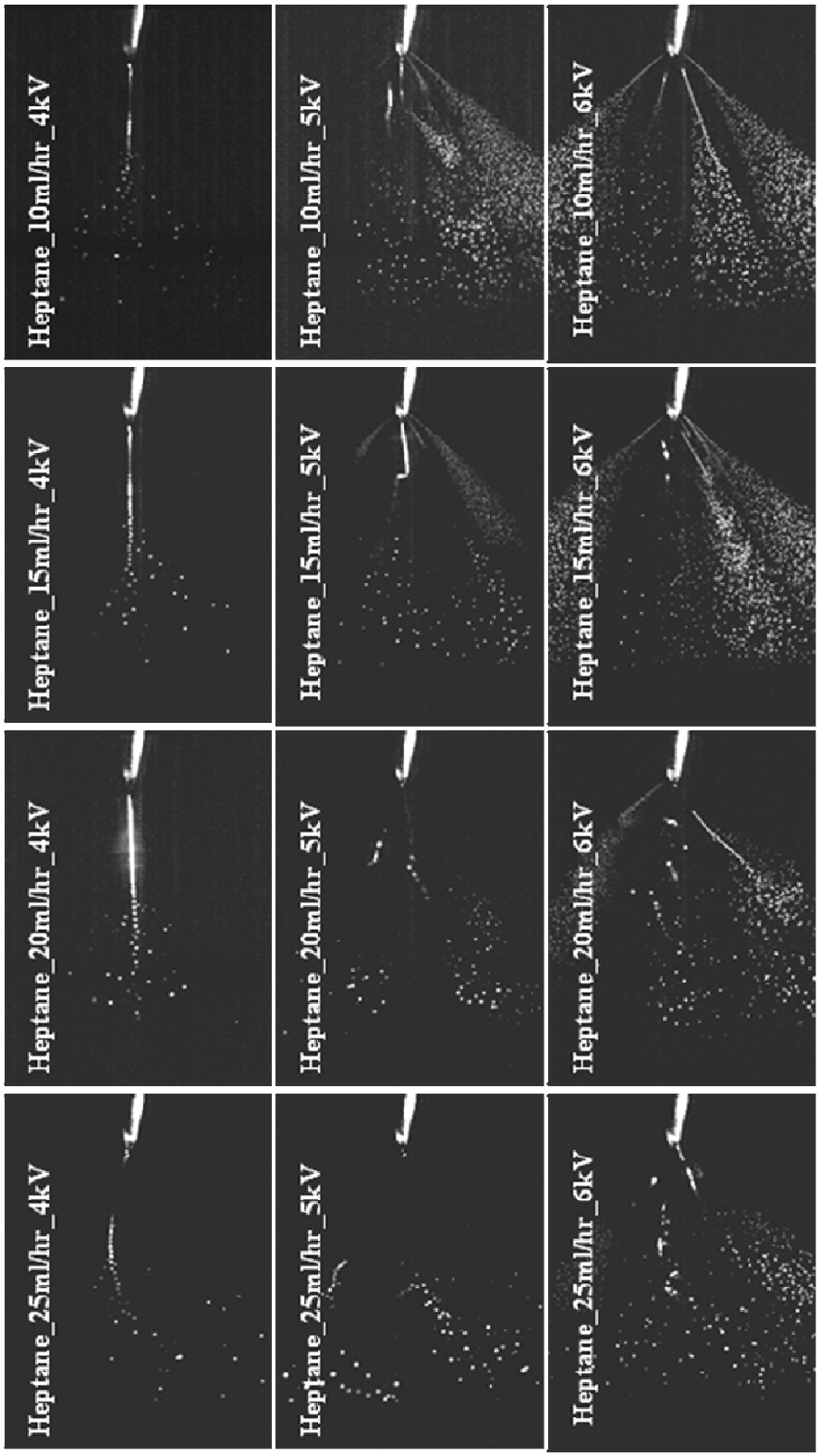

Figure 3.3 (cont. on next page)

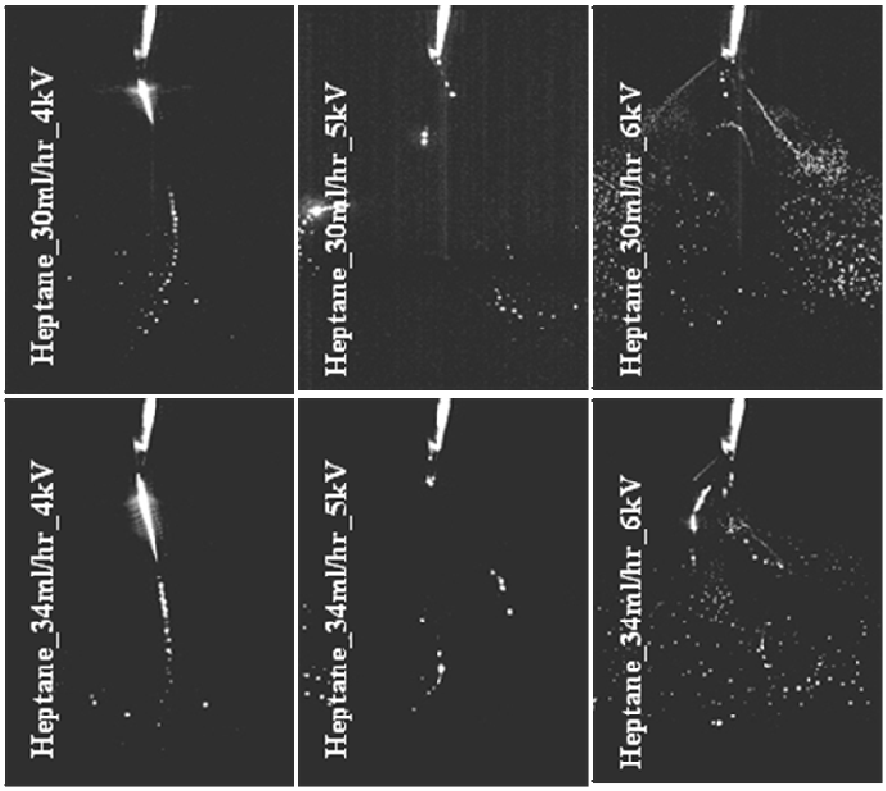

Figure 3.3 Electrospray imaging results for Heptane with 2% Stadis

3.1.2 High-speed visualization of the oscillating menisci of butanol sprays

The importance of the steady conical meniscus in order to establish cone-jet, monodisperce sprays was highlighted in the previous section. The oscillatory behavior of the meniscus in the movies showed to be responsible for generating either continuous or pulsed jets, for lower and higher flow rates respectively and is to be investigated here. In this section, particular emphasis is given to the region of the meniscus apex and to record its time variation with high-speed imaging. For that reason, two butanol electro-sprays were established, case 1: 5kV at 30ml/hr and case 2: 3.5kV at 15ml/hr, in order to demonstrate the continuous and pulsed oscillations respectively.

Figure 3.4 presents a period of one full meniscus oscillation of case 1. The eight images have a time interval of 10^{-4}s to the right and the high-speed camera acquires the videos with a rate of 10,000frames/s, thus the frequency of oscillation is 1250 Hz. Figure 3.5 presents a period of one full meniscus oscillation of case 2. The time sequence of the oscillation occurs, as before, to the right of each row. It is noticeable that no spray is present in the first and last image, indicating the pulsed nature of the spray. The 18 images have a time interval of $8 \cdot 10^{-4}$s and the frequency of oscillation here is around 74 Hz.

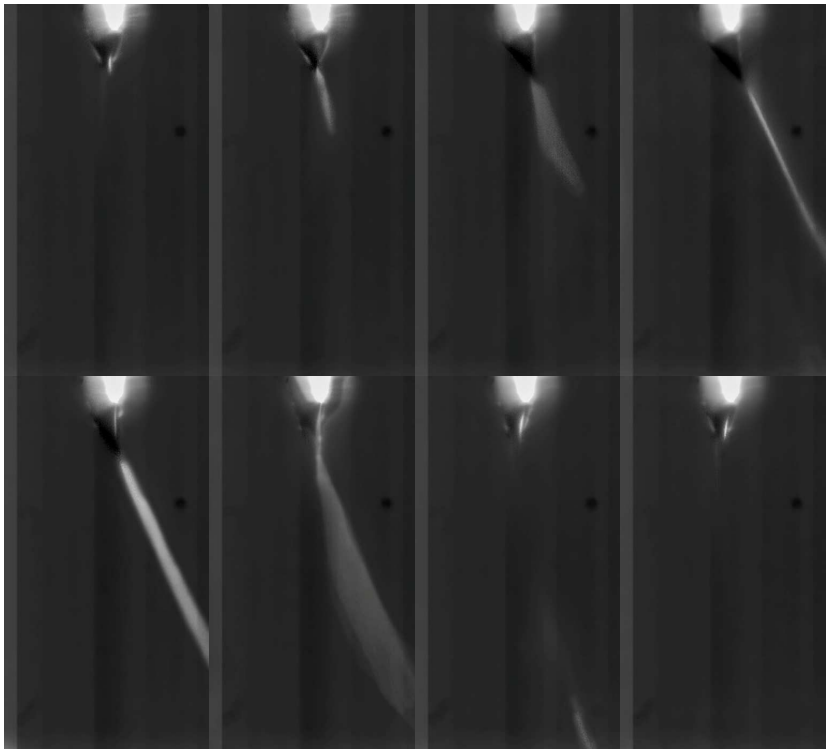

Figure 3.4 A full period of a continuous meniscus oscillation at 30ml/hr and 5kV (courtesy of Michael Penisi-undergraduate assistant)

In both Figures 3.4 and 3.5, it is verified that the shape of the menisci is not conical and is not oriented in the direction of the injector. In particular, Fig. 3.4 shows a shift to the side, which is essentially a screen-shot of the oscillations occurring on the outer surface of the capillary tip. In Fig. 3.5, the deformed shape of the meniscus is compressed and moved to the side as time varies. For both cases, pulsed or continuous, the spray is generated from a time-dependent origin, thus rationalizing its unsteady nature. In the following sections, it will be shown that this leads to poly-disperse sprays, contrary to the findings of [5, 6].

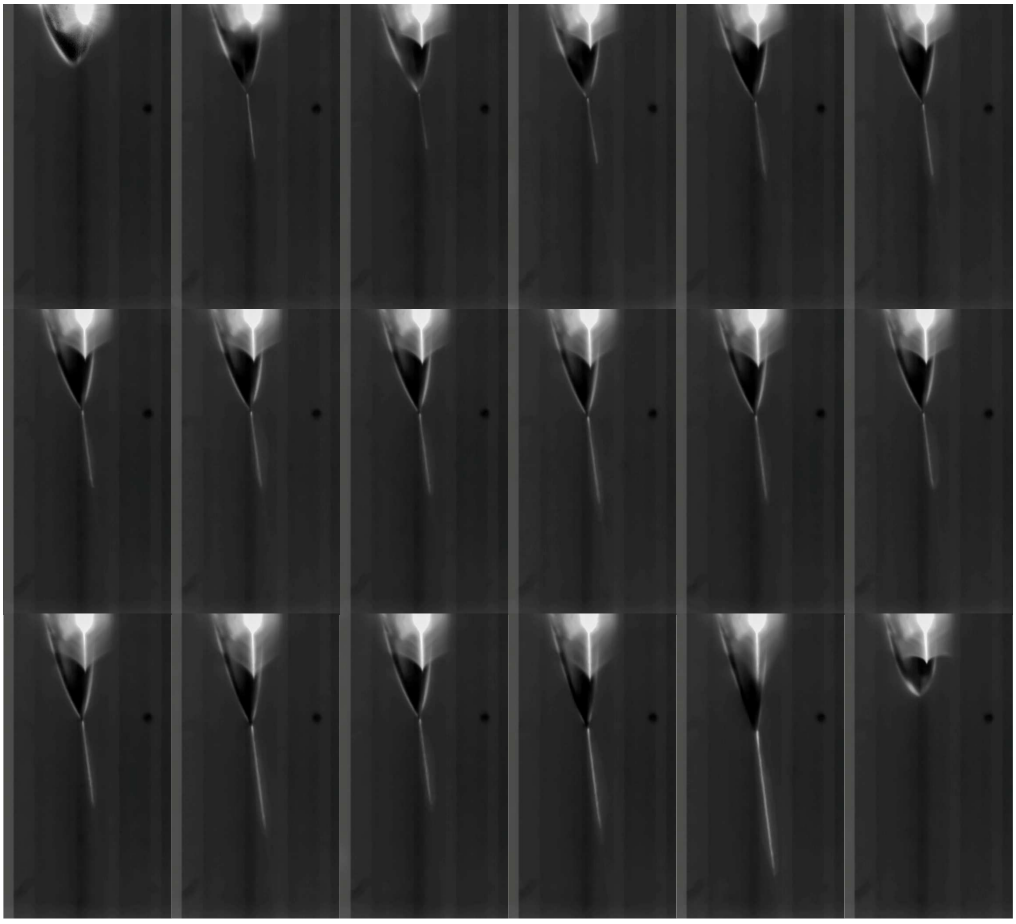

Figure 3.5 A full period of a pulsed meniscus oscillation at 15ml/hr and 3.5kV (courtesy of Michael Penisi-undergraduate assistant)

3.1.3 Electrospray high-speed visualization for low flow rates of butanol

As discussed in section 3.1.1, the establishment of cone-jet sprays may require a finer increment of flow rate and applied voltages in order to be tracked, especially for a fuel that has not been investigated from this aspect before and has potentially novel modes of e-spray operation. For that reason, smaller butanol flow rates, 1ml/hr-4.5ml/hr

were investigated, as shown in Fig. 3.6. This data was taken in the range of the minimum voltage that could support an electrospray, i.e. range 3.3kV-3.5kV. It was interesting to notice that for this low flows, the created electrosprays were **steady** with a conical stable meniscus at the outside surface of the capillary tip. In some cases, satellite droplets were present and deviated from the main body of the spray and in the rest of the cases the fan of droplets was narrower, however, atomization was similar to the results of [5, 6].

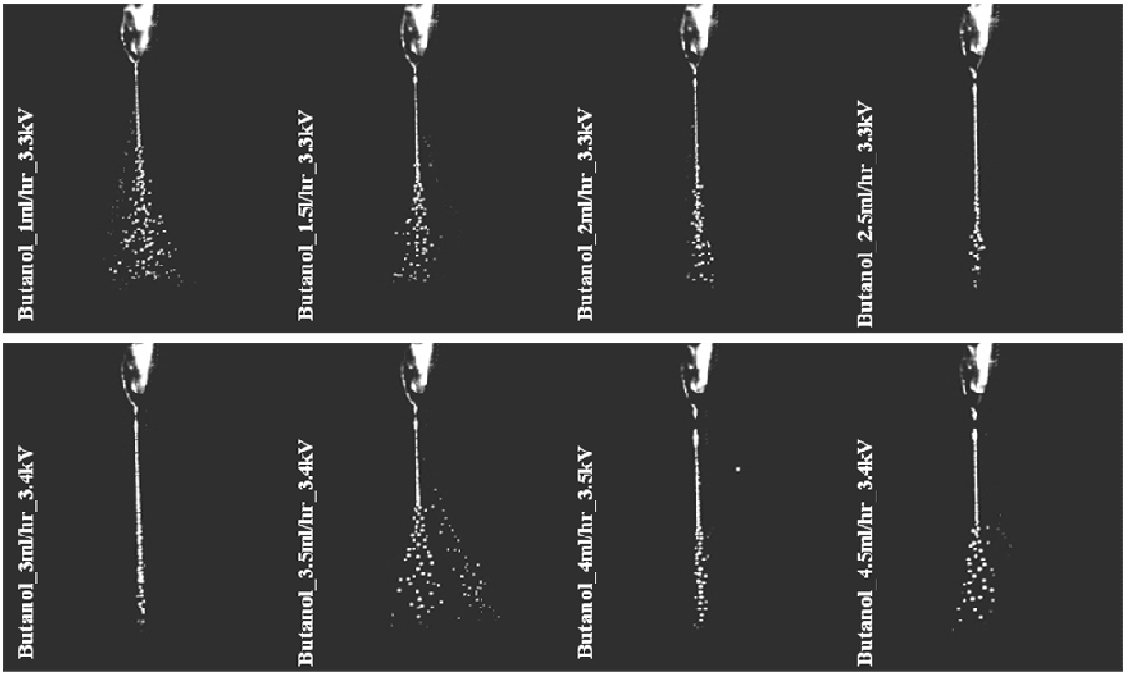

Figure 3.6 Electrospray imaging results for small flow rates of butanol

3.1.4 High-speed visualization of electrosprays of mixtures of same electrical conductivity and surface tension

The results of Figs. 3-1-3.3 show clear differences in the way the e-sprays of the three fuels behave. In order to look for the reason for these differences, a comparison was performed of three mixtures of different chemicals that have very closely the same electrical conductivity and the same surface tension. The detailed properties of these mixtures were given in Table 2.2. Imaging results are presented in Figures 3.7-3.9, for mixtures 1-3 respectively. All flow rates varied from 10ml/hr-35ml/hr with an increment of 5ml/hr and the applied voltages ranged from 4-6kV with an increment of 1kV, totaling 18 images of the spray per Figure. It is reminded here, that each of the images was selected to be characteristic of the particular spray-movie it described and it corresponded to the screenshot when most details of the spray structure were apparent. Similarly to section 3.1.1, for clarity reasons, all three Figs. are presented in the end of the paragraph after the corresponding discussion.

For an applied voltage of 4kV, even though the spray was not stable in many of the mixture cases, only one jet appeared at the apex of the meniscus. This meniscus was not conical, as it would be observed in a cone-jet mode of electrospray operation [5]. It was rounded, in the form of a deformed droplet of the liquid and slipped on the outer conical surface of the capillary tip, producing a repeatability of the spray. For Mixture 1 and for low flow rates (10-20mlhr) an intermittent mode of operation was observed, since the emission of the jet was pulsed, with an average frequency on the order of

250Hz. As the flow rate increased further, the jet became continuous and ramified, as seen in Fig 1.6d,e. For Mixtures 2 and 3 no such a change in the mode of their operation took place for the flow rates under consideration. For low flow rates (10-20mlhr), simple jets were observed [27], with large drops surrounded by satellite drops, in most of the cases. As the flow rate increased further, an interesting atomization phenomenon was revealed at 4kV, for all mixtures.

The single jet appearing for this level of voltage (4kV), had a length that increased with flow rate. For the lowest flow rates of 10 and 15 ml/hr, a narrow column jet can be seen in Figures 3.7-3.9, surrounded by a fan of droplets. For flow rates above 20 ml/hr, the liquid ligament was long enough and strongly illuminated by the laser light, indicating that atomization took place at a small region close to the electrical ground and that this region shrunk further for flow rates close to 30ml/hr. This could potentially imply an atomization issue for the structure measurements and for that purpose it will be discussed in the following section.

There are suggestions in the literature that the jet length increases, not only with increasing flow rate of the liquid, but also with increasing electrical conductivity and viscosity [27]. Given that the three mixtures under consideration are formed to be equally resistive to the applied electrical field, any differences in the jet length at the same flow rate conditions would be attributed to their different viscosities, which were shown in Table 2.2. In practice though, a negligible effect of viscosity on the jet length

was demonstrated, probably due to the small discrepancies among the viscosity values of the mixtures shown in Table 2.2.

Atomization was efficient with increasing voltage, (5kV and 6kV). For Mixture 1 and for a voltage of 5kV, an intense oscillation of the meniscus around the capillary tip was observed, which increased with flow rate. The meniscus was never split to a multi-jet, except for the lowest flow rate of 10ml/hr. In all other cases spray break-up occurred as a result of kink instabilities. As observed in earlier sections, the high-speed visualization revealed an unsteady jet that demonstrated an increasing "swing" around the vertical direction with increasing flow rate. For Mixtures 2 and 3 and for an applied voltage of 5kV, two modes of electrospray operation were observed for the range of flow rates under investigation and a passage from one mode to another occurred at 25ml/hr. For both mixtures, the mode corresponding to the low flow rates (10-20ml/hr) was that of the multi-cone jet. The corona of the spray was split in several emissive cusps, three in most of the cases, allowing a free rotation of the spray around the conical surface of the capillary exit. For higher flow rates (25-35ml/hr), sprays of Mixture 2 converged into a single continuous jet, the length of which increased with flow-rate, similarly to sprays at 4kV, however atomization seemed not be an issue. For Mixture 3, convergence of the various jets in a single one was observed as well, but the corresponding mode was that of a whipping jet, with an increasing area of random spraying around the jet with increasing flow rate. Increasing the applied voltage further, at 6kV, all sprays for all mixtures were operating in the multi-jet regime.

Figure 3.7 (cont. on next page)

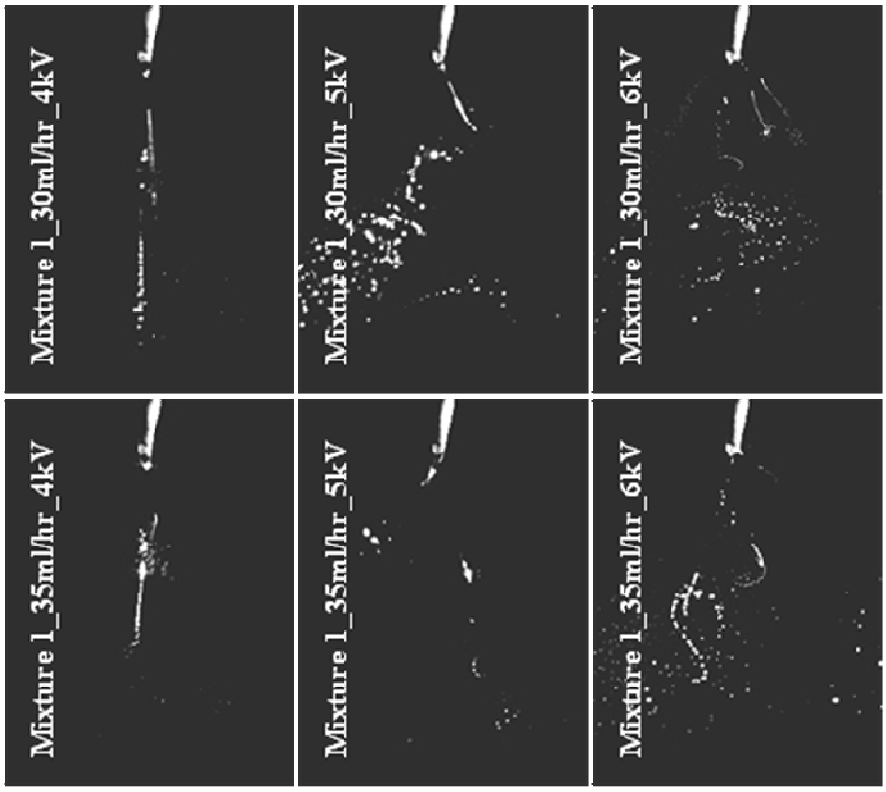

Figure 3.7 Electrospray imaging results for Mixture 1

Figure 3.8 (cont. on next page)

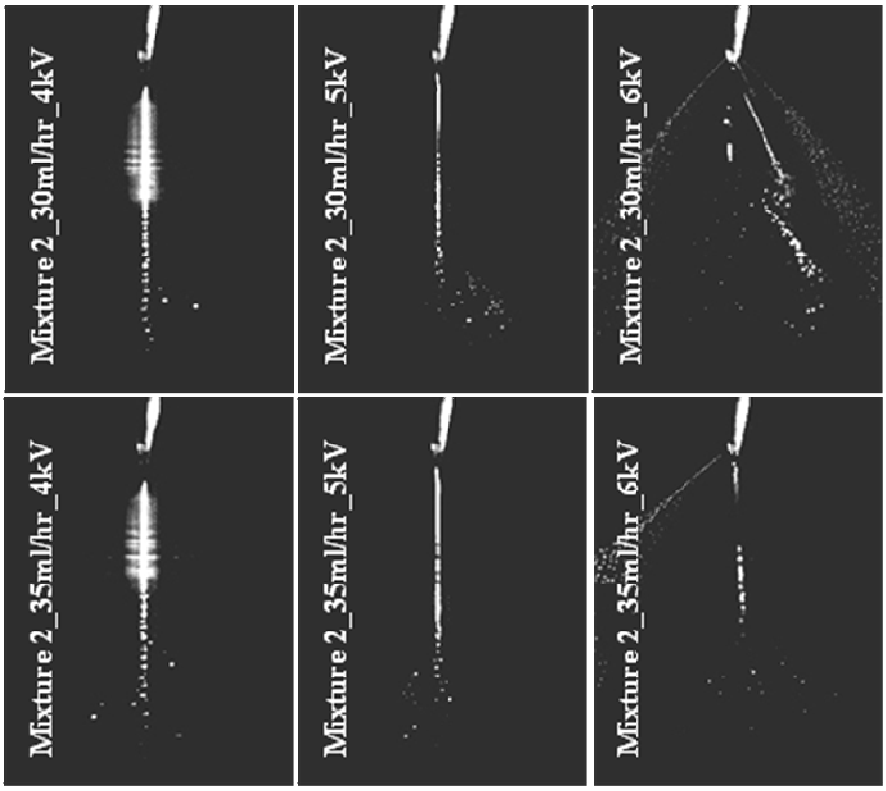

Figure 3.8 Electrospray imaging results for Mixture 2

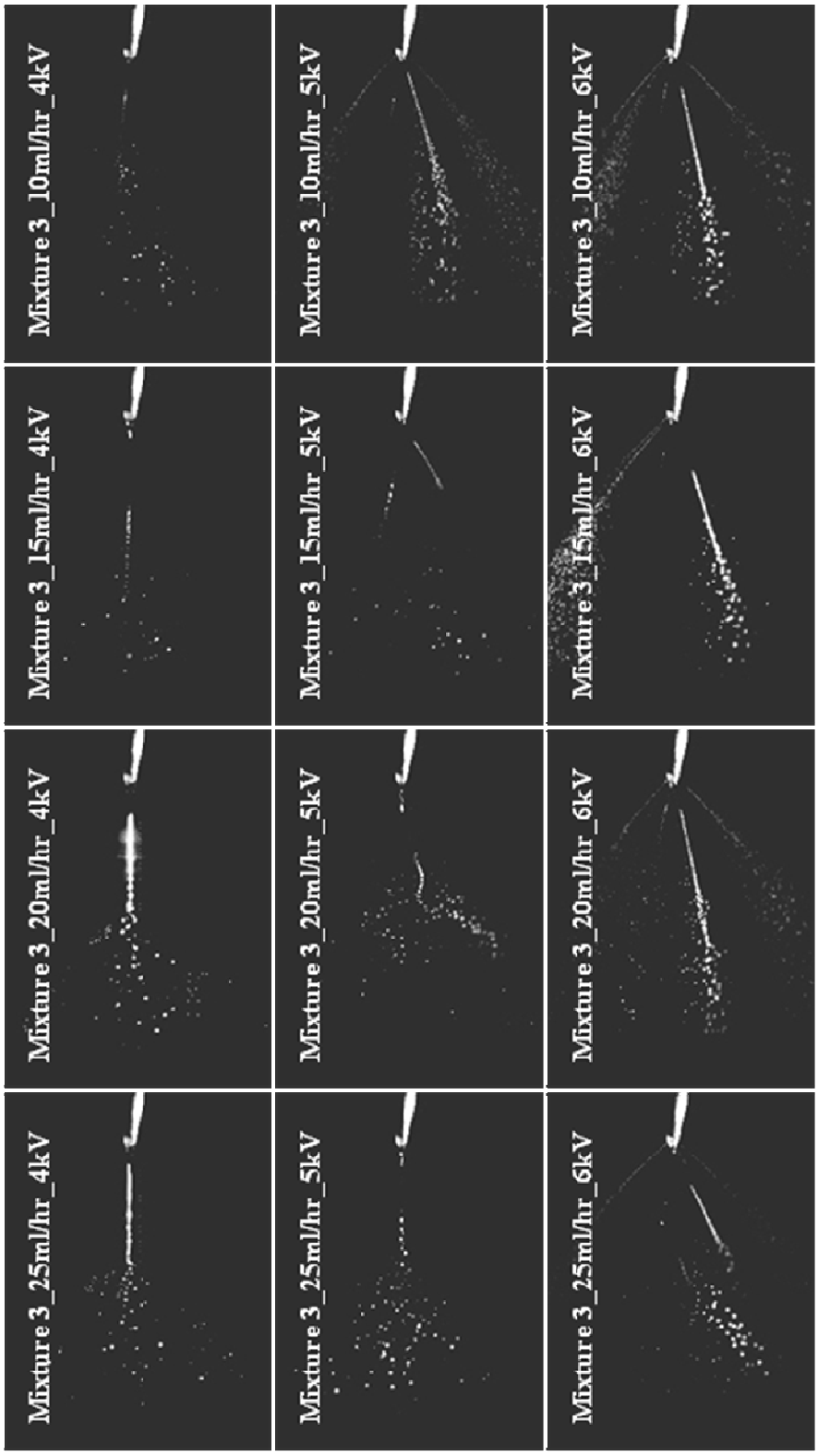

Figure 3.9 (cont. on next page)

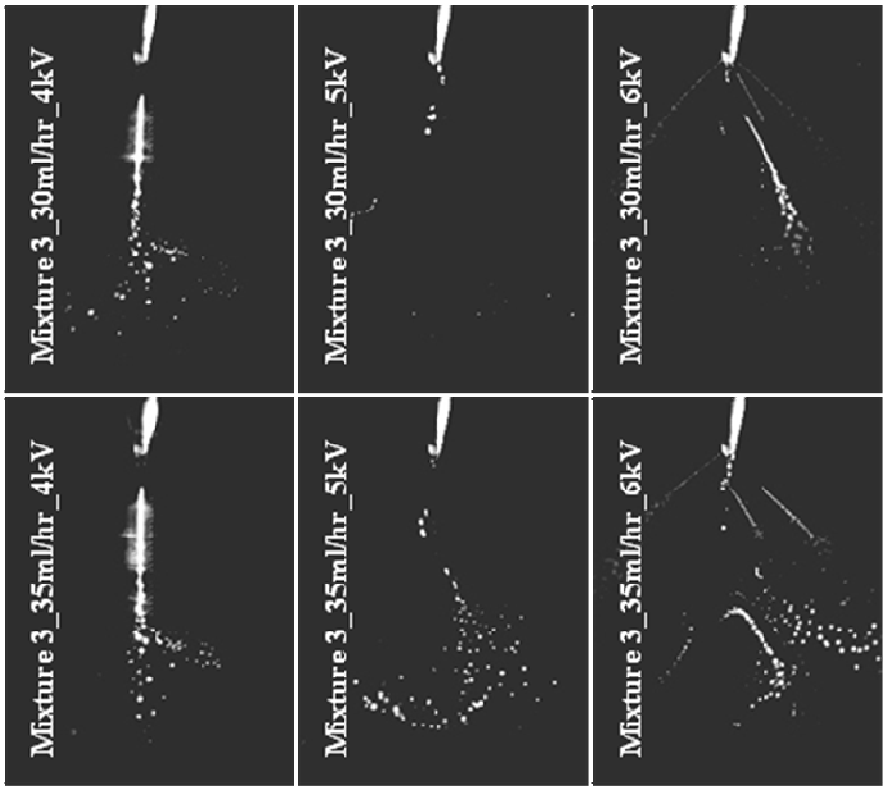

Figure 3.9 Electrospray imaging results for Mixture 3

The overall electrospray behavior of mixtures with the same conductivity, the same surface tension, but different composition did reveal some similarities among their actual modes of operation, however, substantial differences were demonstrated as well. It is noted that as long as the instability that will ultimately lead to the break up of the liquid column and the generation of the spray has not developed fully, i.e. when the voltage is low (4 kV) the sprays exhibit similar behavior. Once the instability occurs (>5 kV), there are occasional differences. The sprays were mostly generated through kink instabilities, hence the electrosprays were unstable and ramified the liquid column into streams of liquid droplets. In comparing these unstable behaviors, it is not reasonable to expect a precise similarity for initial conditions that are very closely similar – this would violate the very definition of instability.

The exact regime for each set of conditions was characterized by the same randomness that corresponded to the ways an instability could propagate, i.e. unstable behaviors between sprays of different mixtures were as similar as sprays coming from the same mixture. In other words, the fundamental properties in the electrospray creation, namely electrical conductivity and surface tension did influence the onset of the instability but did not determine the exact temporal evolution of the resulting spray pattern. Similarities have to be sought only in the qualitative sense. This explains why the mixtures have increased similarities for the same applied voltage. For example at lower voltages (5 kV), the results of Figs. 3.7-3.9 suggest that whipping jets prevail, whereas when the voltage increases (6 kV), multi-jet spraying occurs. However, if the

randomness caused by the instability were the sole source of difference among the three mixtures, only the visualization data would differ, whereas droplet size statistics should be the same. This will be discussed in section 3.2.3.

3.2 Electrospray Structure (I) : Droplet Size Measurements

3.2.1 Butanol droplet size distributions

The droplet size distribution of butanol electrosprays as a function of mass flow rate per spray and applied voltage is shown in Fig. 3.10a-g. Results are presented for flow rates from 5 to 35ml/hr with an increment of 5 ml/hr and applied voltages between 3 and 6 kV with an increment of 500V.

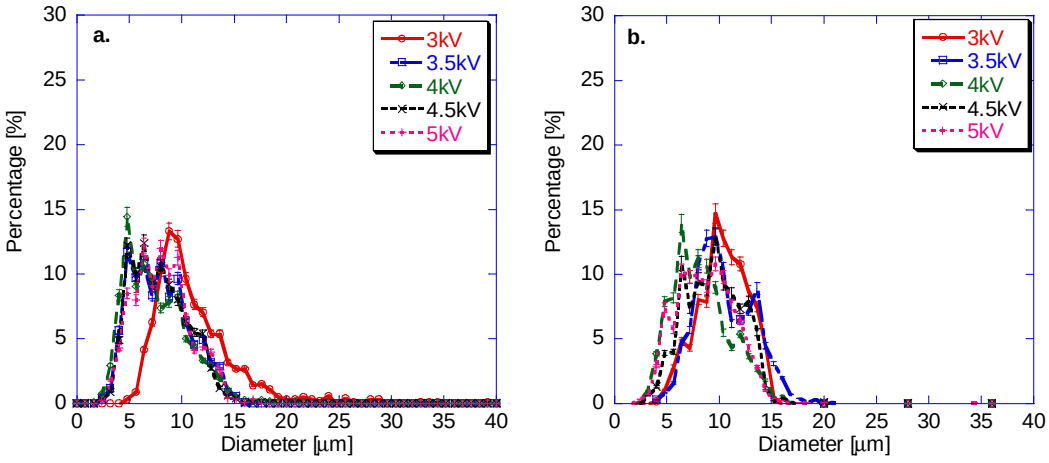

Figure 3.10 (cont. on next page)

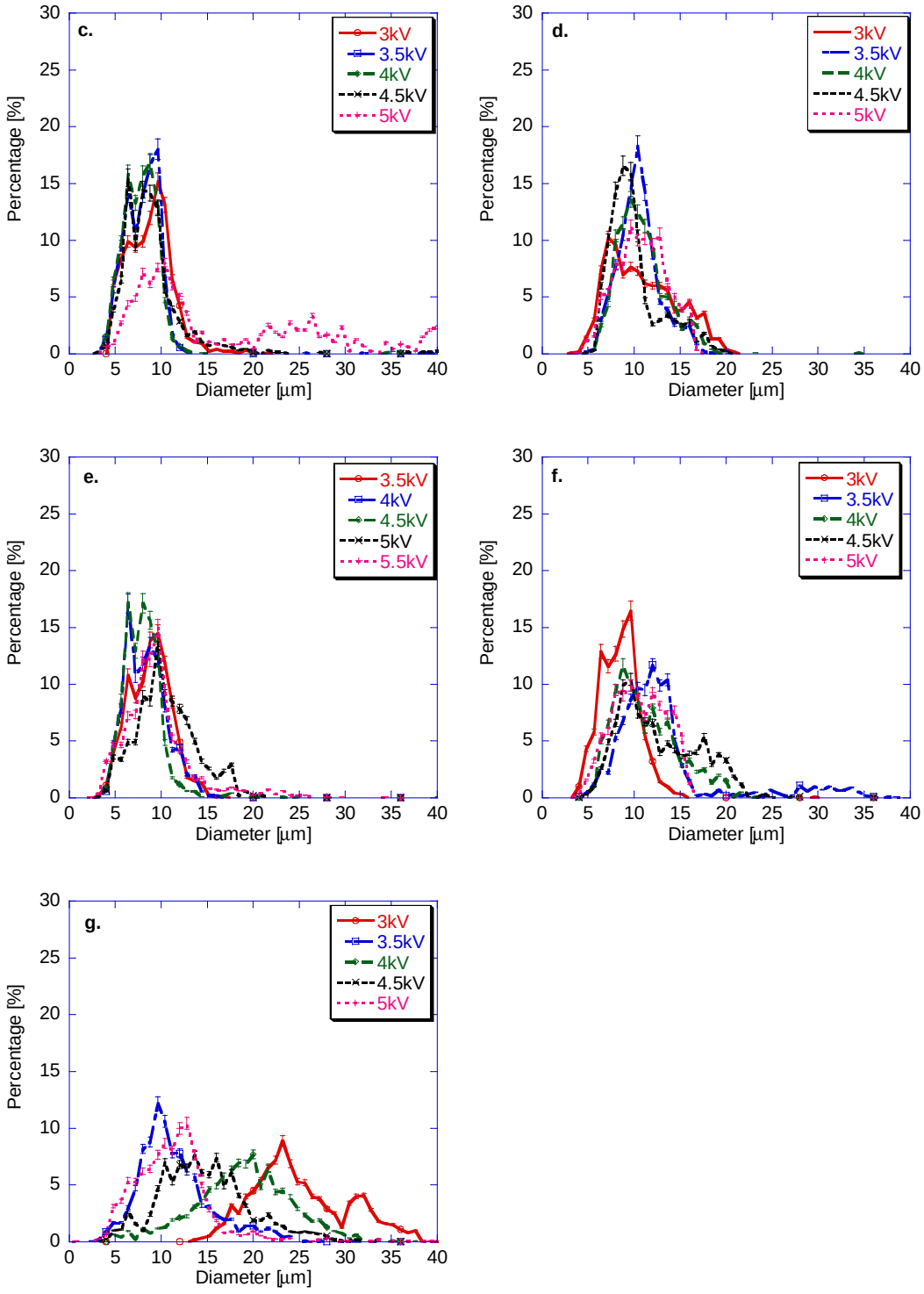

Figure 3.10 Distribution of the droplet diameter of Butanol for flow rates (a) 5ml/hr, (b) 10ml/hr, (c) 15ml/hr, (d) 20ml/hr, (e) 25ml/hr, (f) 30ml/hr and (g) 35ml/hr

First, it can be observed that, contrary to the findings of [5-6, 23-25], butanol electrosprays are not monodisperse. The 10% ratio of the standard deviation of the distributions over the mean droplet diameter reported in previous studies [6] is not observed here and the size distribution is far from being a "Dirac"-type function. For the two lower flow rates, the size distribution is almost equally narrow for all applied voltages. The droplet size becomes more sensitive to the electrical field as the flow rate increases and broader distributions are observed for all voltages. The increase in size dispersion with increasing flow rate is very mild until 25ml/hr and becomes considerable at 35ml/hr. Similarly, the narrowest size distribution (at 3.5 kV) is practically unaffected by flow rate. This result constitutes a second important difference from previous published results that indicate a minor effect of applied voltage on hydrocarbon electrosprays, for which fluid conductivity varied between 0.7 and 9.8×10^{-8} $(\Omega cm)^{-1}$ [5, 6].

The observed polydispersion relates closely to the unsteadiness of the sprays revealed by the high-speed movies of section 3.1.1. The uniformity in droplet size is, in practice, destroyed by any oscillation or instability of the meniscus, which is what is verified by the droplet size measurements. Similar findings are shown in the paragraphs that follows for ethanol and heptane. The structure measurements define the degree of polydispersion, however its presence was expected after studying the spray phenomenology results.

In order to minimize any differences with previous studies [5, 6, 23] due to the experimental set-up, droplet size distributions were also measured for ethanol and heptane. The results are presented in Figs. 3.11a-c and 3.12a-c respectively, for flow rates of 15, 25 and 35ml/hr. Results for ethanol electrosprays in Fig. 3.11, indicate a polydisperse behavior similar to butanol.

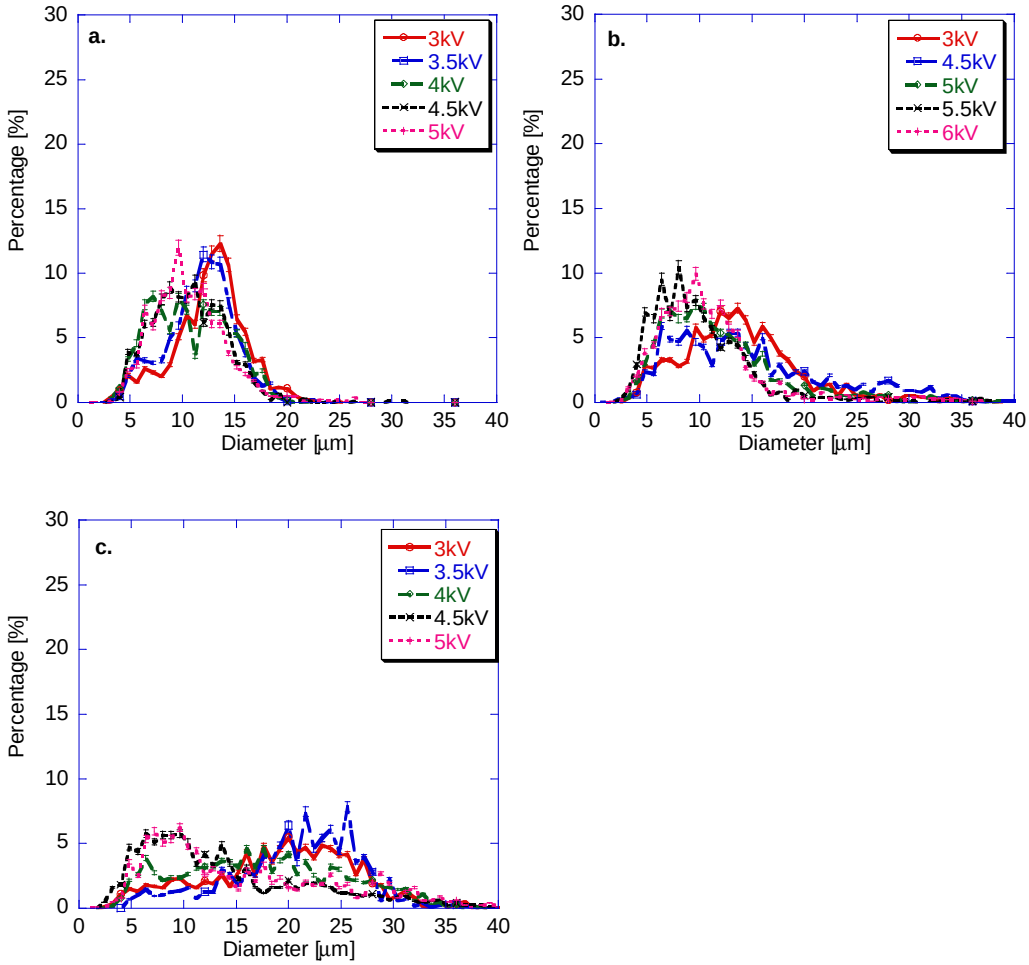

Figure 3.11 Distribution of the droplet diameter of ethanol for flow rates (a) 15ml/hr, (b) 25ml/hr and (c) 35ml/hr

In these cases, the droplet size distribution has a greater standard deviation for the same number of counts compared to butanol, indicating larger dispersion. As the flow rate increases, the distributions become broader, with most of the high voltage lines decreasing symmetrically as the flow rate rises. Thus, in the case of ethanol the effect of the applied electrical field is again not as significant as the flow rate in the formation of the spray. In contrast, in the case of heptane, Fig 3.12, the spray is not sensitive to changes in the applied electrical field only for the lowest flow rate.

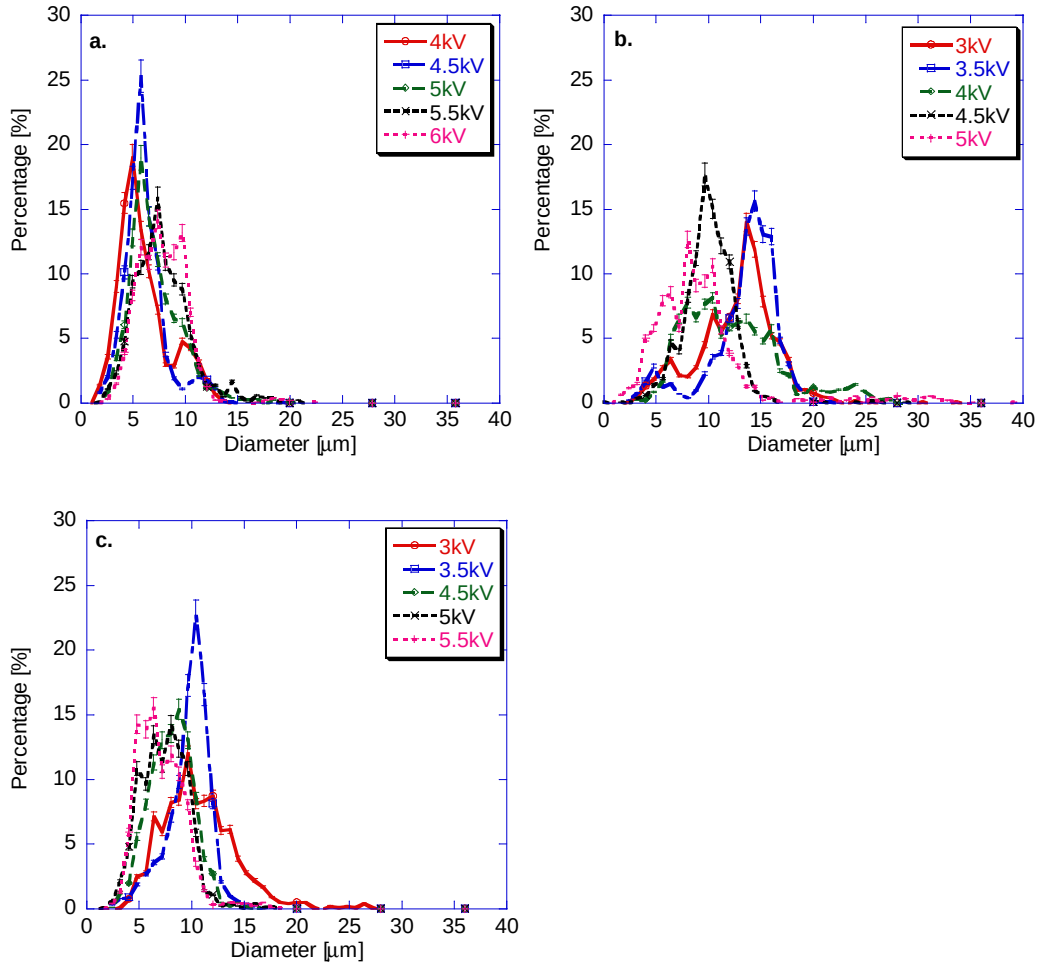

Figure 3.12 Distribution of the droplet diameter of heptane for flow rates (a) 15ml/hr, (b) 25ml/hr and (c) 35ml/hr

Heptane sprays show a narrower droplet distribution compared to the other two fuels, however they cannot be considered monodisperse either. For most of the high voltage cases, an increase in dispersion is observed with increasing the flow rate, similarly to what was observed for ethanol and low conductivity liquids in [5, 6, 23]. The differences between the present experimental findings and results published in the literature [5, 6] deserve further investigation. Notwithstanding the poly-dispersion of the distributions, the dependence of average diameter on both applied voltage and flow rate was investigated. Related results are presented in Figs. 3.13 and 3.14 that report measurements of the average diameter (d_{10}) as a function of these two parameters for the three liquids under consideration.

For a constant flow rate, the average droplet diameter shows, in most of the cases, a mild decrease with increasing applied voltage. These findings agree to previously published results for hydrocarbon electrosprays [5, 6], which indicate an insensitivity of heptane droplet size to voltage for a set flow rate at flow rates smaller than an order of 10 ml/hr (the precise value was determined by the amount of conductivity enhancer added to the heptane). Figure 3.14 shows that this observation holds for the liquids under investigation, since for the lowest flow rate the average diameter is shown to be flat verifying the negligible effect of voltage.

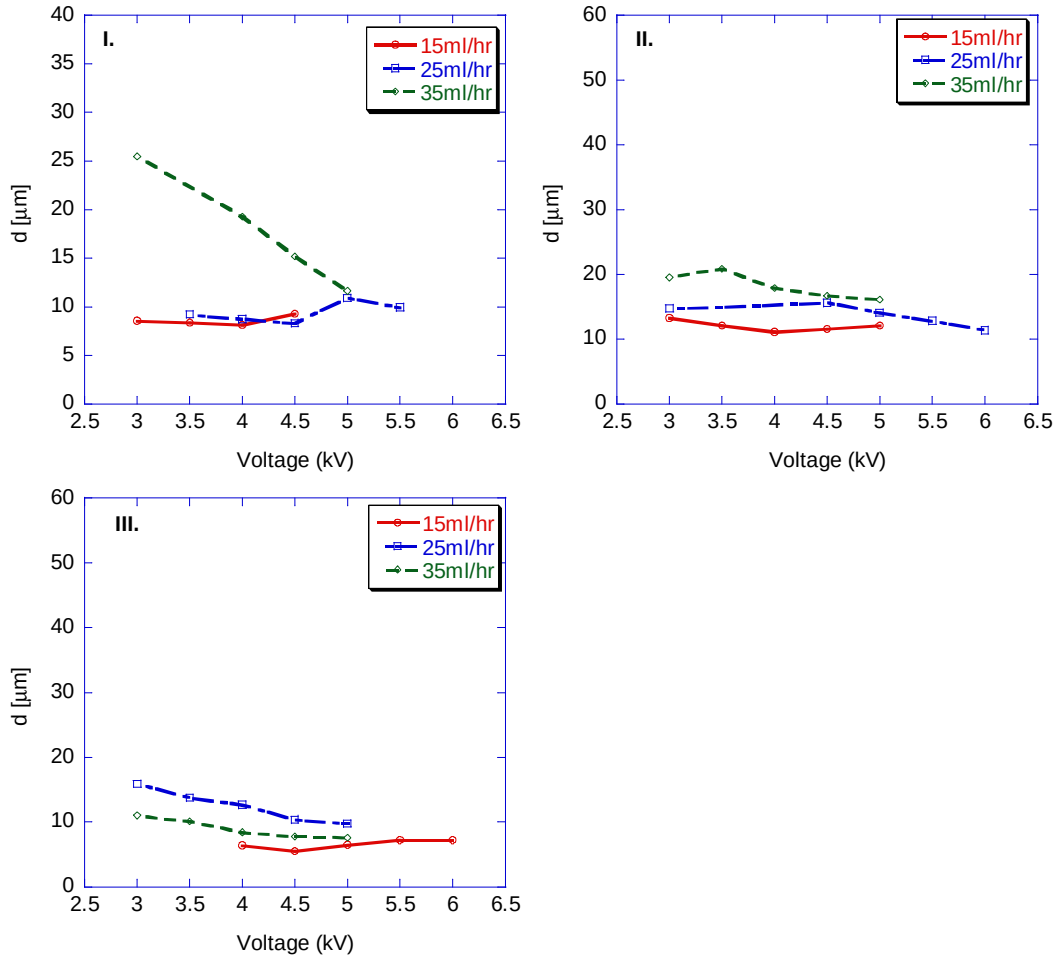

Figure 3.13 Effect of applied voltage on the mean droplet diameter for (I) Butanol, (II) Ethanol and (III) Heptane with 2% Stadis

Furthermore, under constant voltage, there is an increase in droplet size with increasing flow rate for butanol and ethanol, which is in agreement with the established finding that droplet size can be decreased with diminishing flow rates [5, 6]. In the case of heptane, we observe a decrease in the average diameter when decreasing the flow rate from 25 to 35 ml/hr. It has been suggested that the dependence on flow rate can be fitted

by a power law with exponent equal to 0.68 and 0.62 for lower and higher electrical conductivity values respectively [5, 6], however, subsequent work [24, 25] has already established that these exponents are not universal and can vary significantly from substance to substance. A power law dependence cannot be fitted in the results of Figure 3.14, since more points are necessary for such a calculation.

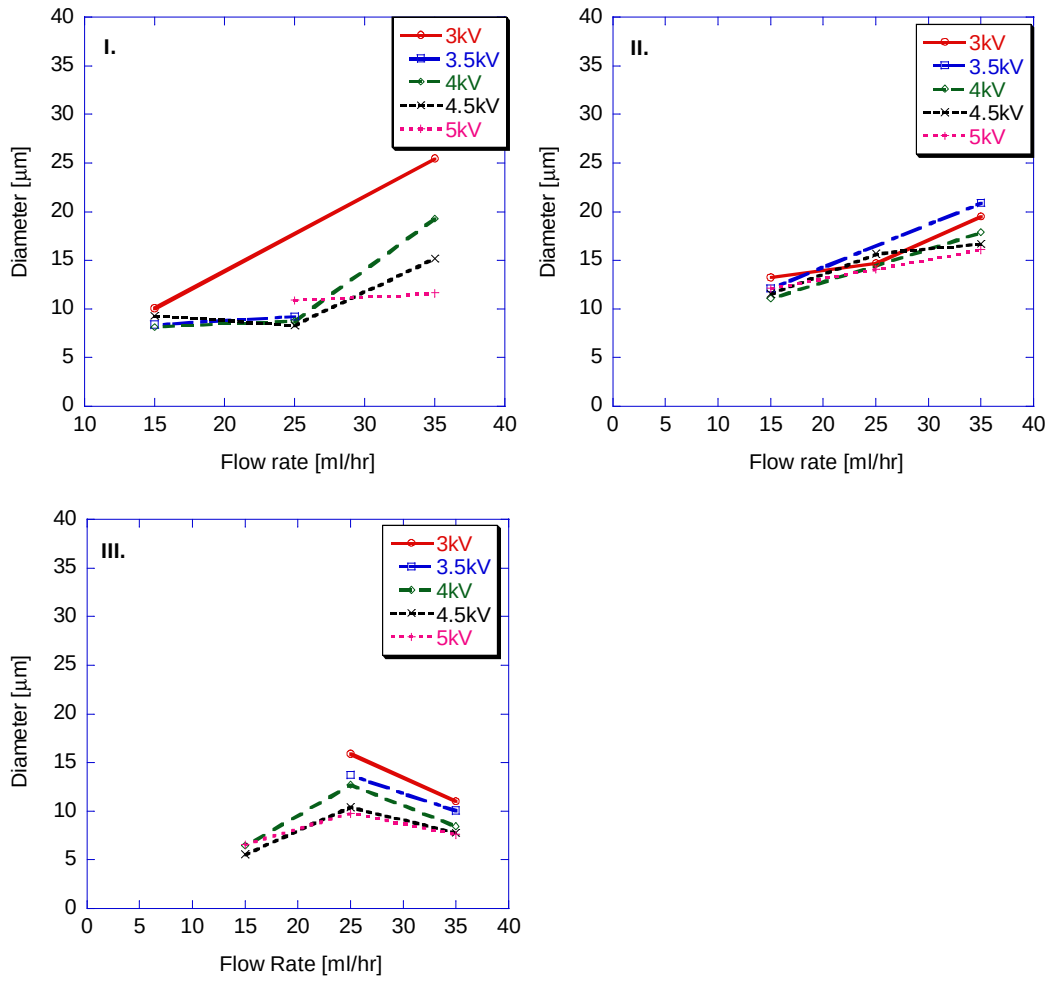

Figure 3.14 Effect of the liquid flow rate on the mean droplet diameter for (I) Butanol, (II) Ethanol and (III) Heptane with 2% Stadis

3.2.2 Low butanol flow rates

Due to the stability of the sprays demonstrated for low flow rates of butanol, droplet size distribution results were obtained for flow rates from 1ml/hr to 4.5ml/hr with an increment of 0.5ml/hr. The applied voltages varied from 3.4kV to 4.6kV, with an increment of 100V. The goal here was to investigate the possibility of monodisperse sprays, the existence of which, is conditioned on the stability of the conical menisci at the injector tip. Probability density function results of the droplet diameter are presented in Fig. 3.15, for the 13 applied voltages.

Contrary to the insensitivity of droplet size on applied voltage observed in the previous section for the lowest flow rate and to the similar literature findings of [5, 6], a dependence on voltage was clearly observed for low flow rates of butanol. In order to capture this dependence, small increments of voltage were selected. The investigation took place for the voltages that did generate a spray. For example, for the lowest flow rates (1ml/hr-2ml/hr), an electrospray could not be established for a voltage lower than 4.6kV.

First, it is observed that at the lowest voltages (3.4kV, 3.5kV) the distribution of flow rates from 1-3ml/hr is narrow. Hence, at the vicinity of voltages where the electrosprays start forming, a behavior close to the cone-jet and the monodispersity is favored. However, what is even more worth highlighting is that after a departure from the narrow distributions (cases 3, 4, 5) the established electrosprays return to approach

the cone-jet regime around 4.3kV and this occurs for all flow rates, not only for the lower ones as in case (1). In these distributions even though the 10% monodispersity ratio of the standard deviation over the average diameter [6] is not achieved, however the corresponding 18% could predict similar trends.

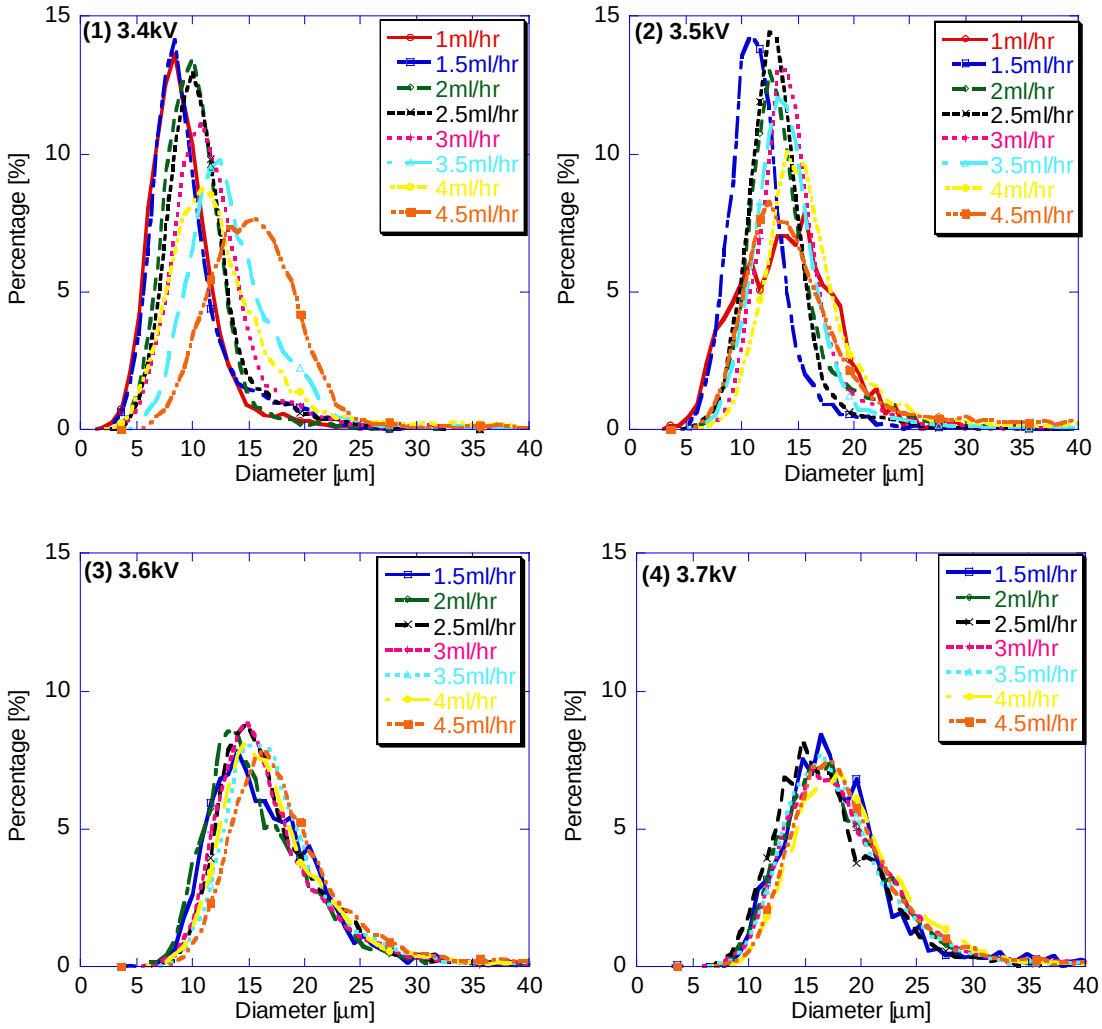

Figure 3.15 (cont. on next page)

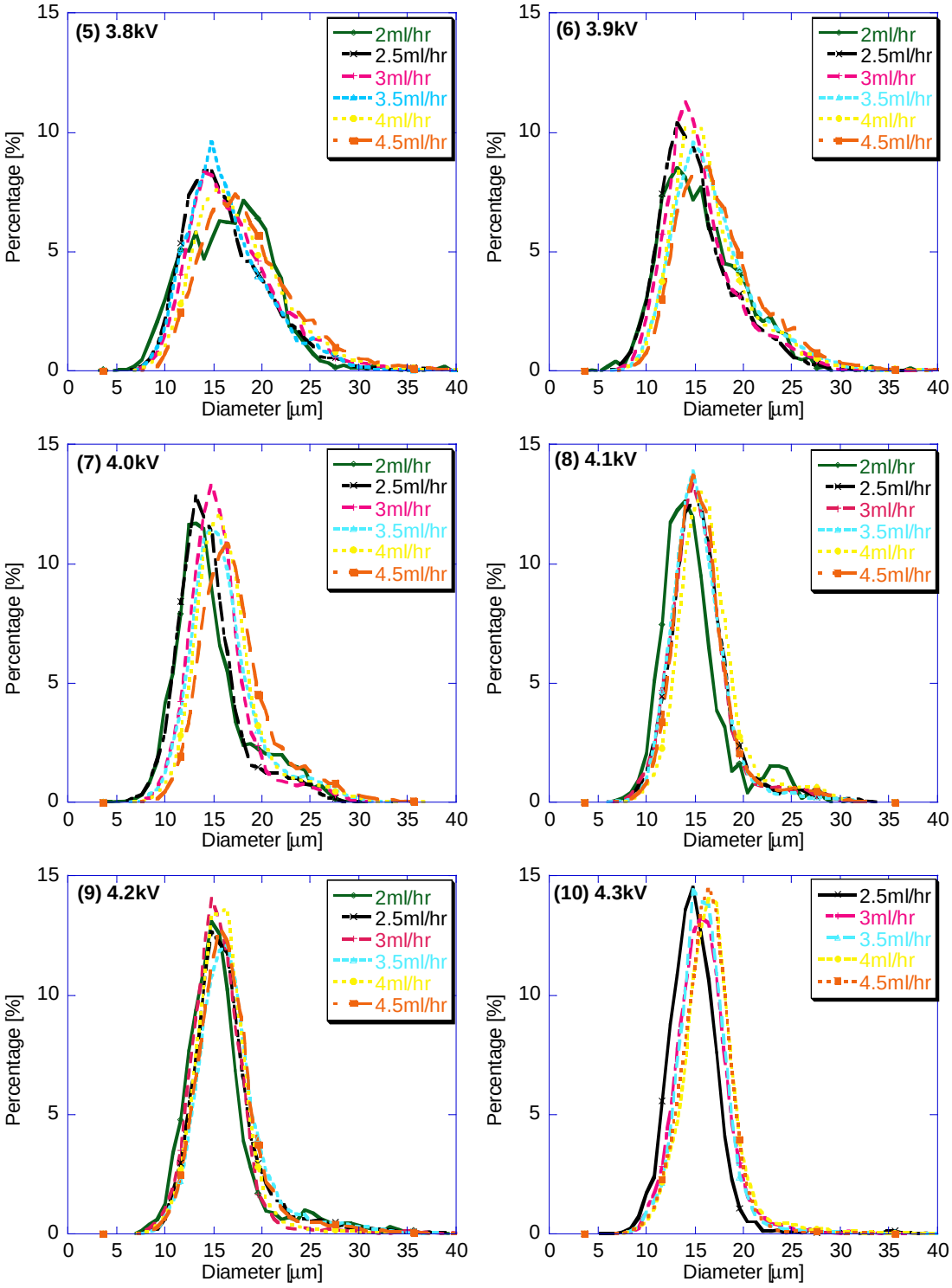

Figure 3.15 (cont. on next page)

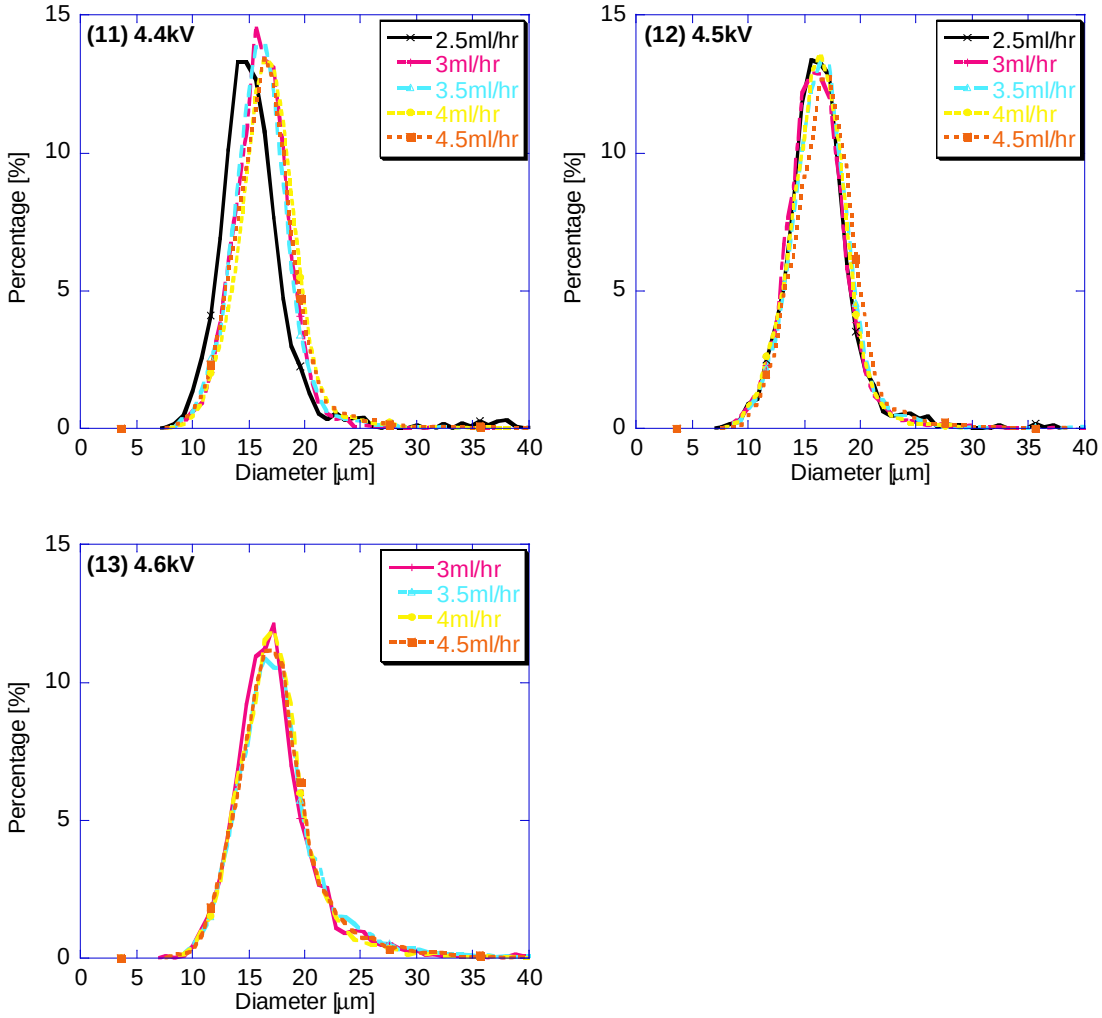

Figure 3.15 Distribution of the droplet diameter of low flow rates of Butanol for voltages (1) 3.4kV, (2) 3.5kV, (3) 3.6kV, (4) 3.7kV, (5) 3.8kV, (6) 3.9kV, (7) 4.0kV, (8) 4.1kV, (9) 4.2kV, (10) 4.3kV, (11) 4.4kV, (12) 4.5kV and (13) 4.6kV

For a constant flow rate, Fig. 3.16 shows the dependence of droplet size on voltage. It is interesting to observe that, contrary to earlier findings of this or of literature [5, 6] work, this relation is not monotonic. An increase of droplet size is observed which peaks in the vicinity of 3.7 kV, then an abrupt decrease until a minimum value in the region of 4.3kV and then an increasing trend is again observed. It is noticeable that the

voltages where the minima are observed in Fig. 3.16 correspond to the narrowest droplet size distributions of Fig. 3.15. The effect of voltage is dominant, as mentioned earlier, contrary to the insensitivity predicted for heptane in [5, 6] at flow rates smaller than approximately 10 ml/hr.

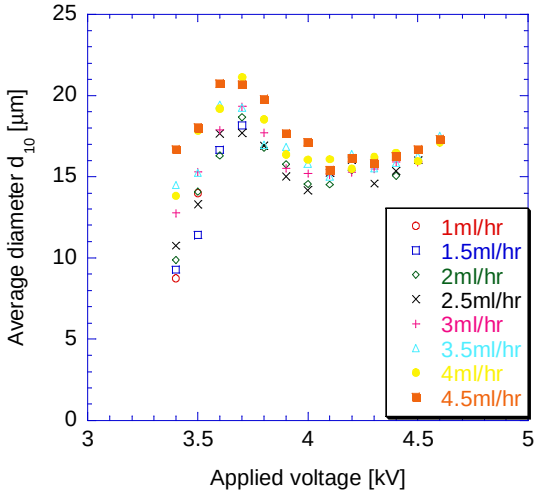

Figure 3.16 Effect of applied voltage on the mean droplet diameter of Butanol

The effect of liquid flow rate is investigated in Figs. 3.17a and 3.17b, where under constant voltage, there is an increase in droplet size with increasing flow rate. These findings are in agreement with the already established finding that droplet size can be decreased with diminishing flow rates [5, 6]. The power law dependence discussed in the earlier section, was obtained with a satisfactory regression coefficient for many of the cases investigated here. The equation used for the regression was of the form $y = \alpha \cdot x^{\beta}$, where α is a constant and β is an exponent. The values of β and the corresponding regression coefficients R^2 are presented in Table 3.1.

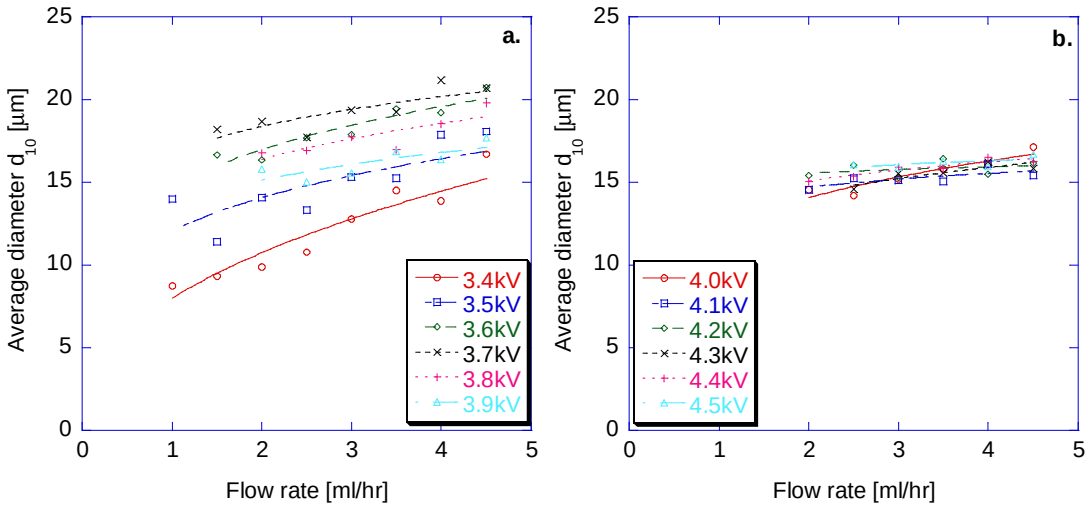

Figure 3.17 Effect of flow rate on the mean droplet diameter of Butanol for: (a) Voltages 3.4-3.9kV and (b) 4.0-4.5kV

Table 3.1 Overall exponent of the power law and the corresponding regression constant R^2 for all test cases

Case →	3.4kV	3.5kV	3.6kV	3.7kV	3.8kV	3.9kV	4.0kV	4.1kV	4.2kV	4.3kV	4.4kV	4.5kV
Exponent β	0.43	0.22	0.21	0.13	0.18	0.15	0.21	0.80	0.35	0.15	0.11	0.53
Regression Coefficient R^2	0.95	0.80	0.93	0.82	0.83	0.79	0.93	0.72	0.37	0.87	0.94	0.63

3.2.3Droplet size distribution of e-sprays of mixtures of the same electrical conductivity and surface tension

The electrospray droplet size distributions of the mixtures presented in section 3.1.4 as a function of mass flow rate and applied voltage are shown in Figs. 3.18-3.20. Results are presented for flow rates from 10 to 35ml/hr with an increment of 5 ml/hr and five applied voltages between 4 and 7 kV.

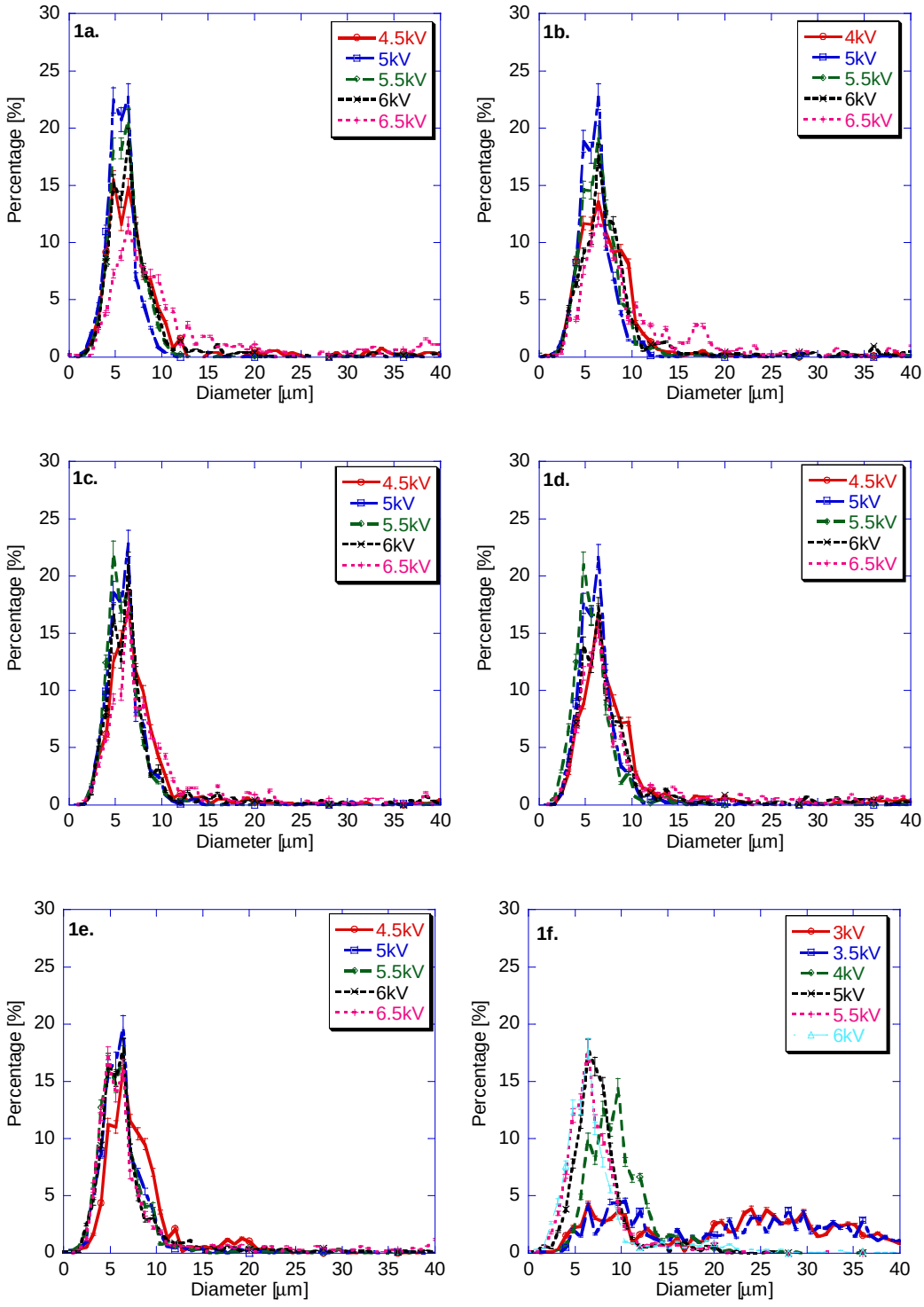

Figure 3.18 Distribution of the droplet diameter of Mixture 1 for flow rates (1a) 10ml/hr, (1b) 15ml/hr, (1c) 20ml/hr, (1d) 25ml/hr, (1e) 30ml/hr and (1f) 35ml/hr

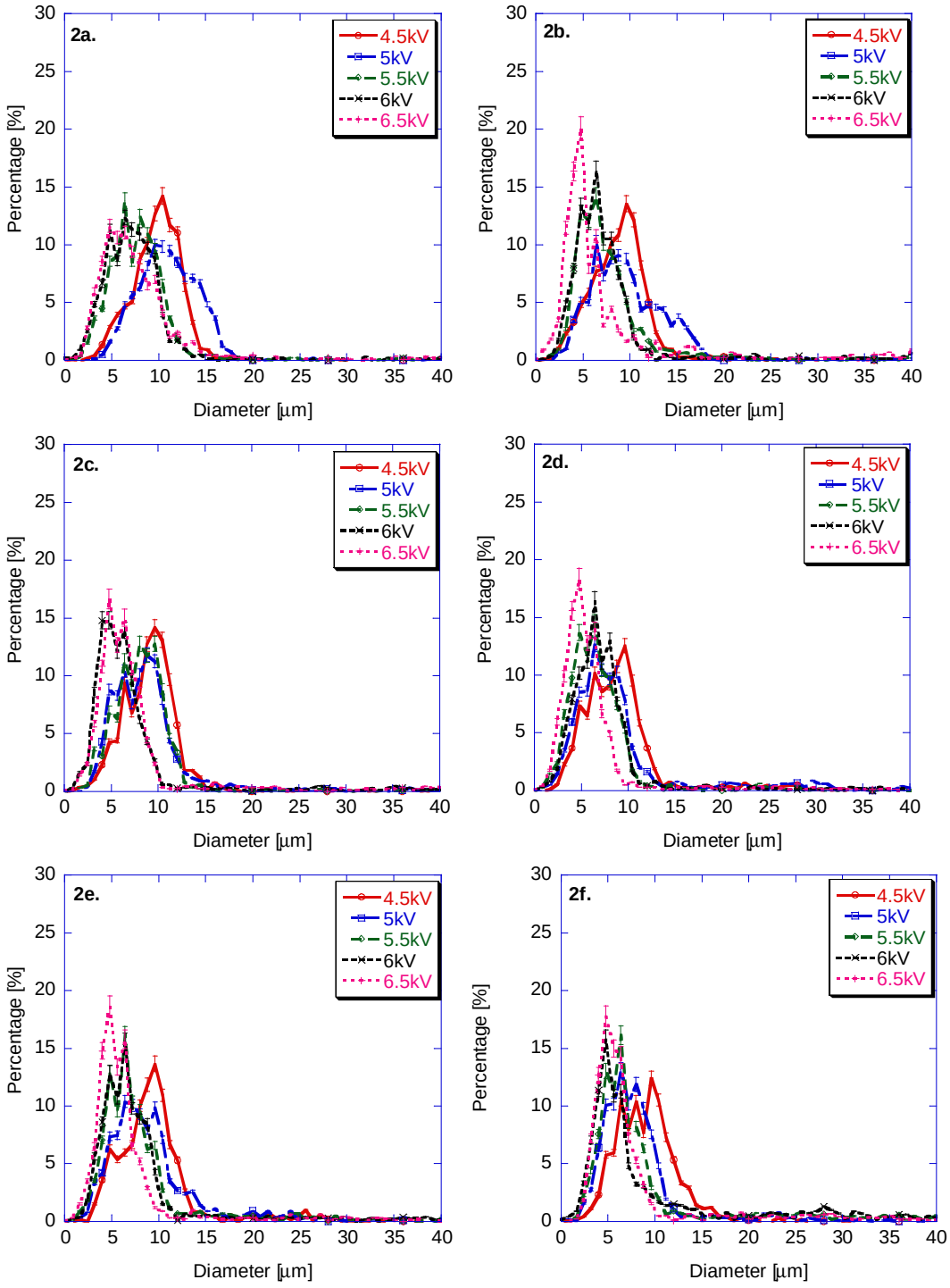

Figure 3.19 Distribution of the droplet diameter of Mixture 2 for flow rates (2a) 10ml/hr, (2b) 15ml/hr, (2c) 20ml/hr, (2d) 25ml/hr, (2e) 30ml/hr and (2f) 35ml/hr

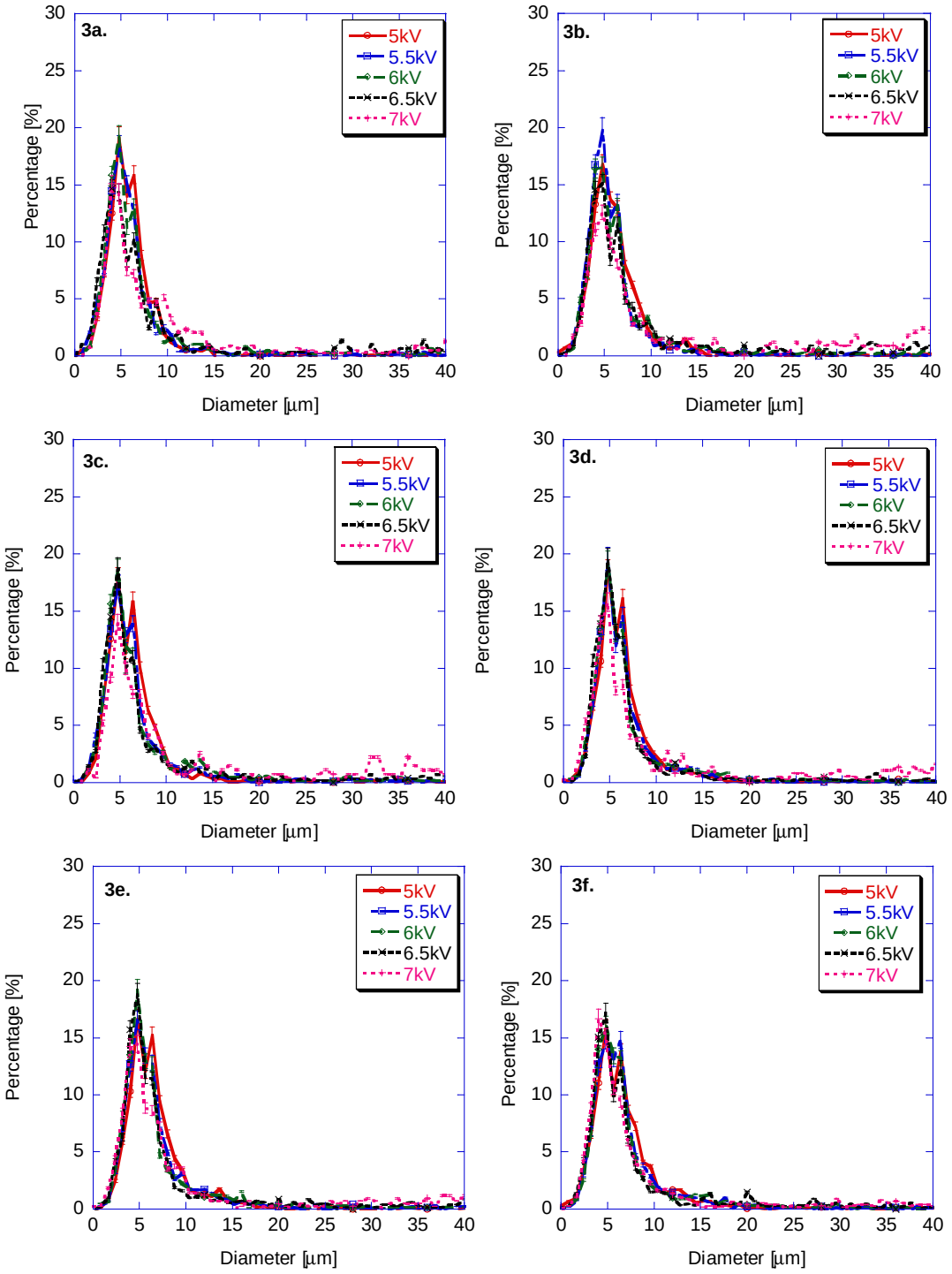

Figure 3.20 Distribution of the droplet diameter of Mixture 3 for flow rates (3a) 10ml/hr, (3b) 15ml/hr, (3c) 20ml/hr, (3d) 25ml/hr, (3e) 30ml/hr and (3f) 35ml/hr

Similarly to the pure liquids of section 3.2.1 presented in Figs. 3.10-3.12, the mixture electrosprays show a polydisperse behavior as well. As in the case of the pure liquids, the polydispersion revealed by the high-speed movies was verified through the droplet size measurements. For mixtures 1 and 3, the droplet size distribution is almost equally narrow for all applied voltages and it develops around the same average value for most values of voltage. The droplet size shows a higher sensitivity to the electric field in the case of mixture 2, where the distributions for each applied voltage move towards lower average droplet sizes for a constant flow rate. This is similar to the findings of the previous sections where the average droplet diameter decreased with increasing voltage. The increase in size dispersion is observed only for mixture 2 and this occurs for decreasing voltage for a constant flow rate.

It is noted that mixtures with the same surface tension and electrical conductivity produce different droplet size distributions. This means that, despite their dominant role, these two properties do not determine fully the spray behavior. In addition to electrical conductivity, liquid dielectric constant ε is a property that incorporates effects rising from Coulombic forces, thus constituting a controlling factor in the establishment of an electrospray. As presented in Table 2.1, its value is substantially lower for heptane compared to alcohols and as a result, the formed mixtures have different dielectric constants. This could explain the possible differences at the formation of the e-sprays as well as the increased similarities between mixtures 2 and 3, which both contain heptane. In addition, the mixtures are characterized with different viscosities and densities,

properties that influence the cohesive forces developed on the droplet forming at the capillary tip. Hence, the electrical conductivity and surface tension do not assure similar e-spray formation since this also depends on dielectric constant, density and viscosity.

3.2.4 The Rayleigh limit

Another possible explanation for the spray polydispersion observed in sections 3.2.1 and 3.2.3 in addition to the instability of the menisci of the sprays, is that the droplets contain Coulombic charge above the Rayleigh limit and as a result they disrupt through Coulombic fission [6]. In this section we investigate this probability by calculating the charge conveyed to the droplet and comparing with the Rayleigh limit.

On the surface of the droplets produced by electrostatic atomization a net charge is present, thus Coulomb repulsion forces reduce the binding force due to surface tension that holds the droplet together. If the surface charge density is sufficiently high, the electrostatic force overcomes surface tension and the droplet disrupts [6]. This unstable condition, termed Coulomb fission, was first studied theoretically by Rayleigh [72] who determined that it should occur when q, the total charge on the droplet surface, reached a limiting value, the Rayleigh limit, given by:

$$q^2 = 8 \cdot \pi^2 \cdot \varepsilon_0 \cdot \sigma \cdot d^3 \qquad (3.1)$$

where ε_0 is the permittivity of the medium surrounding the droplet, σ is the liquid surface tension, and d is the droplet diameter.

For butanol, the Rayleigh limit charge density was calculated from eq.(3.1) after dividing q with the volume of the droplet and is plotted in Fig.3.21 as a function of droplet diameter. In the same figure, the measured droplet charge is presented as well.

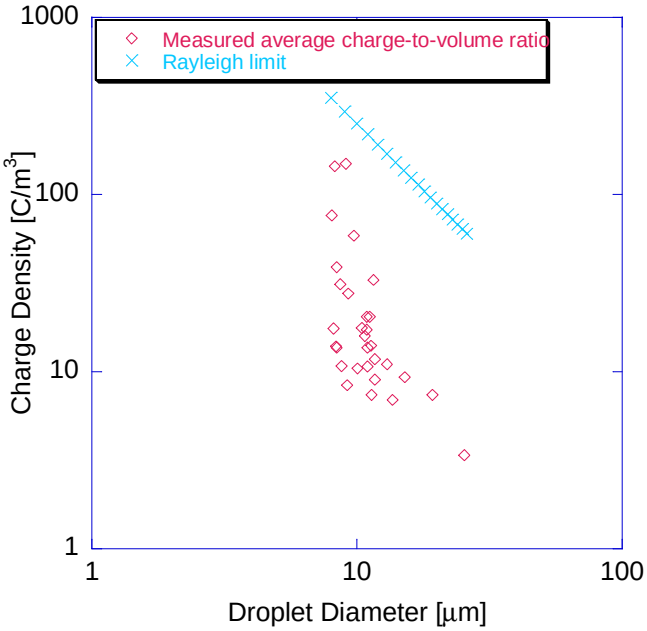

Figure 3.21 Log-log plot of the average charge-to-volume ratio (◊) versus droplet diameter. The Rayleigh limit charge (x) is calculated from eq. (3.1)

The droplet charge was calculated by dividing the measured electrical current flowing through the droplets by the liquid volumetric flow rate. A Keithley 6485 electrometer was connected in series with the electrospray circuit in order to perform the electrical current measurement. Each measured point corresponded to different flow rate and voltage conditions, since these are two parameters used to vary the average droplet diameter. As seen in Fig. 3.21, even for the highest values of charge density

(combinations of high voltage with low flow rates), the Coulombic charges remain below the Rayleigh limit, hence, no droplet break-up occurs due to fission.

3.3 Electrospray Structure (II): Velocity Measurements

In this section, the effects of aerodynamics on spray atomization will be investigated, using the velocity distributions obtained from the Phase Doppler Anemometer. For this purpose velocity probability density functions were generated and Reynolds (Re) and Weber (We) numbers were calculated based on average quantities. Results for butanol sprays are presented in the following paragraphs, whereas data corresponding to ethanol, heptane and the butanol-containing mixtures can be found in Appendix A.

3.3.1 Velocity distributions of butanol electrosprays

Velocity distributions for butanol e-sprays are shown in Fig. 3.22 for flow rates 15ml/hr, 25ml/hr and 35ml/hr. The distributions for the intermediate flow rates (5ml/hr, 10ml/hr, 20ml/hr and 30ml/hr) are provided in Fig. A.1 of Appendix A, where the corresponding information for ethanol and heptane can be found as well (Fig A.2). Velocity distributions of the three mixtures of Table 2.2 are presented in Figs. A.3-A.5 of Appendix A.

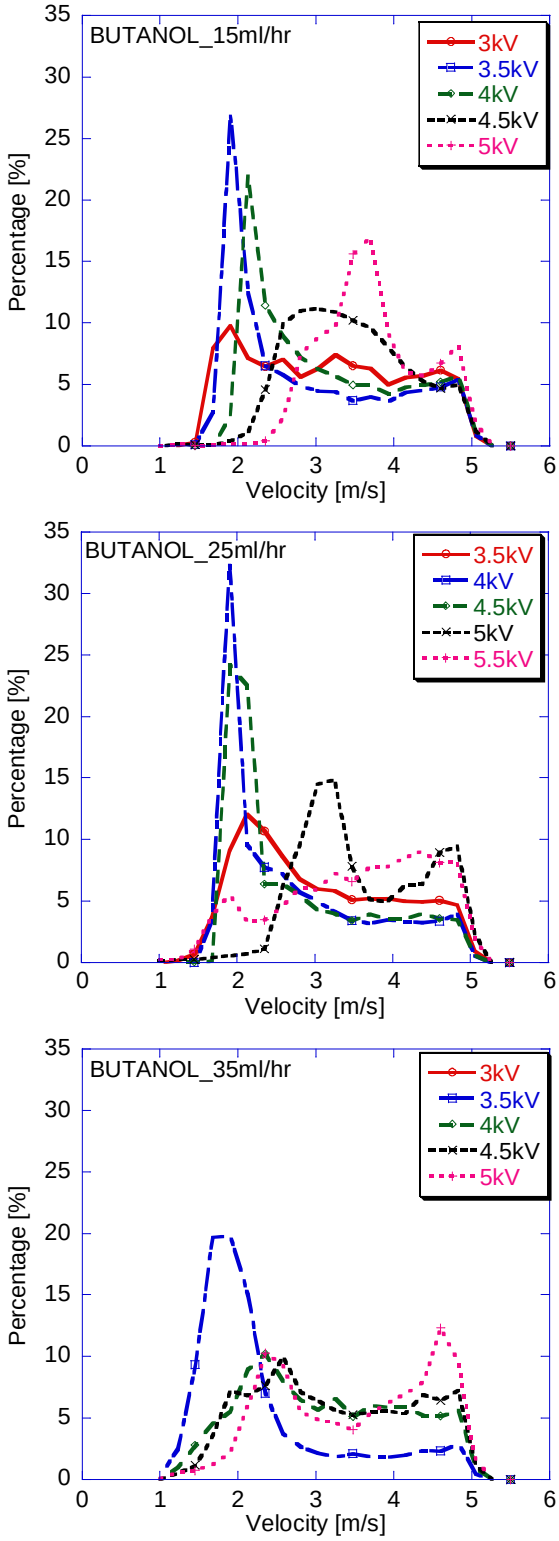

Figure 3.22 Velocity distribution of Butanol for flow rates 15ml/hr, 25ml/hr and 35ml/hr

Fig. 3.22 shows that the non-uniformity in droplet size observed in the earlier paragraphs, pertains to the droplet velocity as well. In most of the cases, the distributions form a plateau without a clearly distinguished maximum. In few cases, a peak velocity value is observed, usually corresponding to single-jet regimes. The effect of flow rate and voltage on the average velocity is presented in Fig 3.23 for butanol and the effect of voltage on the average velocity is given in Fig. A.6 of the Appendix A for both ethanol and heptane. The corresponding Figs. A.7-A.9, for mixtures 1-3 respectively, are located in the Appendix A section as well.

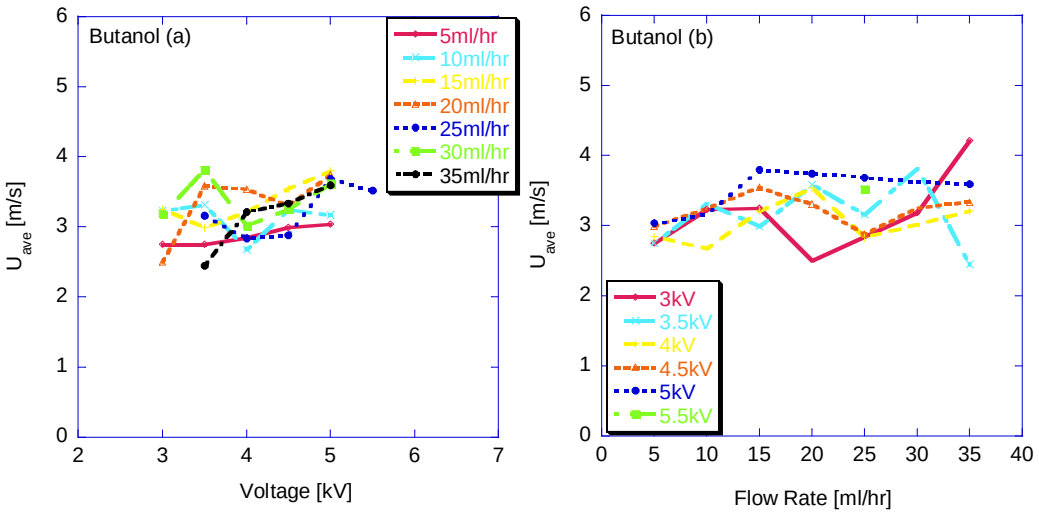

Figure 3.23 Effect of (a) voltage and of (b) liquid flow rate on the mean velocity for Butanol e-sprays

In order to study the aerodynamic effects on the spray formation, two dimensionless numbers, namely Reynolds and Weber numbers, are calculated:

$$\mathrm{Re} = \frac{U_{AVE} \cdot d}{\nu} \tag{3.2}$$

$$We = \frac{\rho \cdot U_{AVE}^{\ 2} \cdot d}{\sigma} \tag{3.3}$$

where U_{AVE} and d is the droplet average velocity and diameter respectively, ν is the kinematic viscosity, ρ is the density and σ the surface tension. For butanol, the calculated *Re* and *We* as a function of both flow rate and applied voltage are presented in Figs.3.24 and 3.25 respectively. The corresponding calculations for ethanol and heptane are given in Figs. A.10-A.11. The Reynolds number calculation determines a transient regime for the flows under investigation. On the other hand, the Weber number offers substantial information about the droplet break-up mechanism.

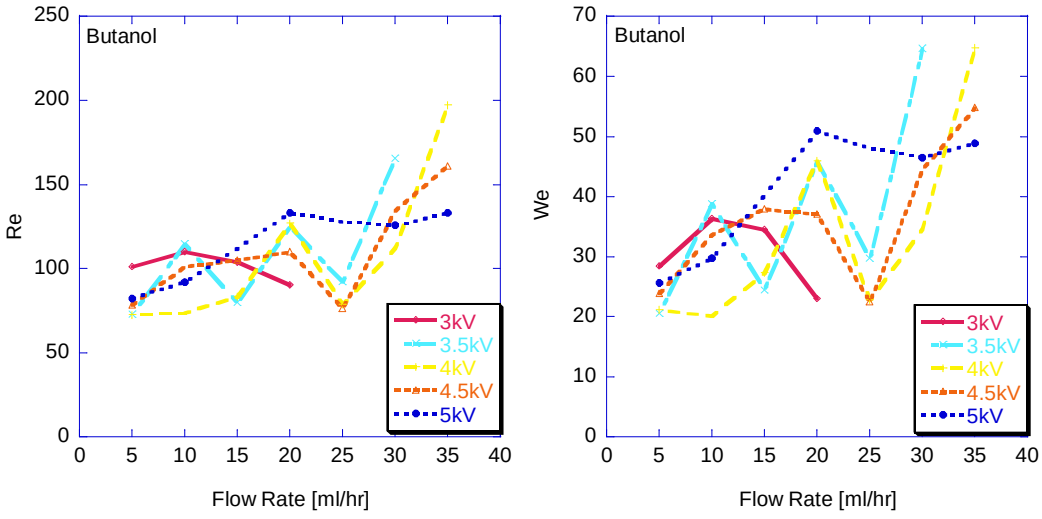

Figure 3.24 Effect of Butanol flow rate on Re and We numbers

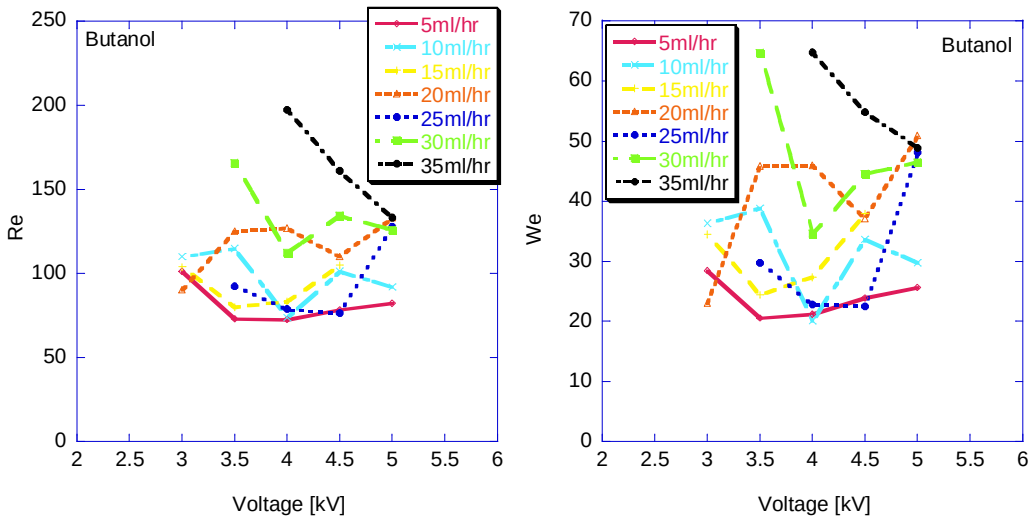

Figure 3.25 Effect of voltage on Re and We numbers for Butanol

A fundamental step in the characterization of a spray flow is droplet disintegration under the effect of inertial forces when a certain droplet size is achieved [77]. For the electrospray study, these forces have resulted in different break-up mechanisms, namely such as Rayleigh and kink type instabilities. Independently of the type of instability that initiates spray break-up, the evolution of the droplets is a function of the *We* number and the observed categories were summarized in [77] and are presented in Fig. 3.26. According to that figure, in butanol electrosprays under investigation, droplet break-up occurs either in the *bag* or in the *bag and stamen* break-up regimes, since We numbers were calculated to be within the range of 20-60. It is possible that these break-up regimes could be responsible for the polydispersion observed in the previous section (3.2), since they do not favor the creation of uniform size droplets, as seen for example in the *vibration* break-up regime. It should also be noted that it is

conceivable that the actual We for these droplets is even higher, since the surface tension is effectively reduced because of the electrostatic effect.

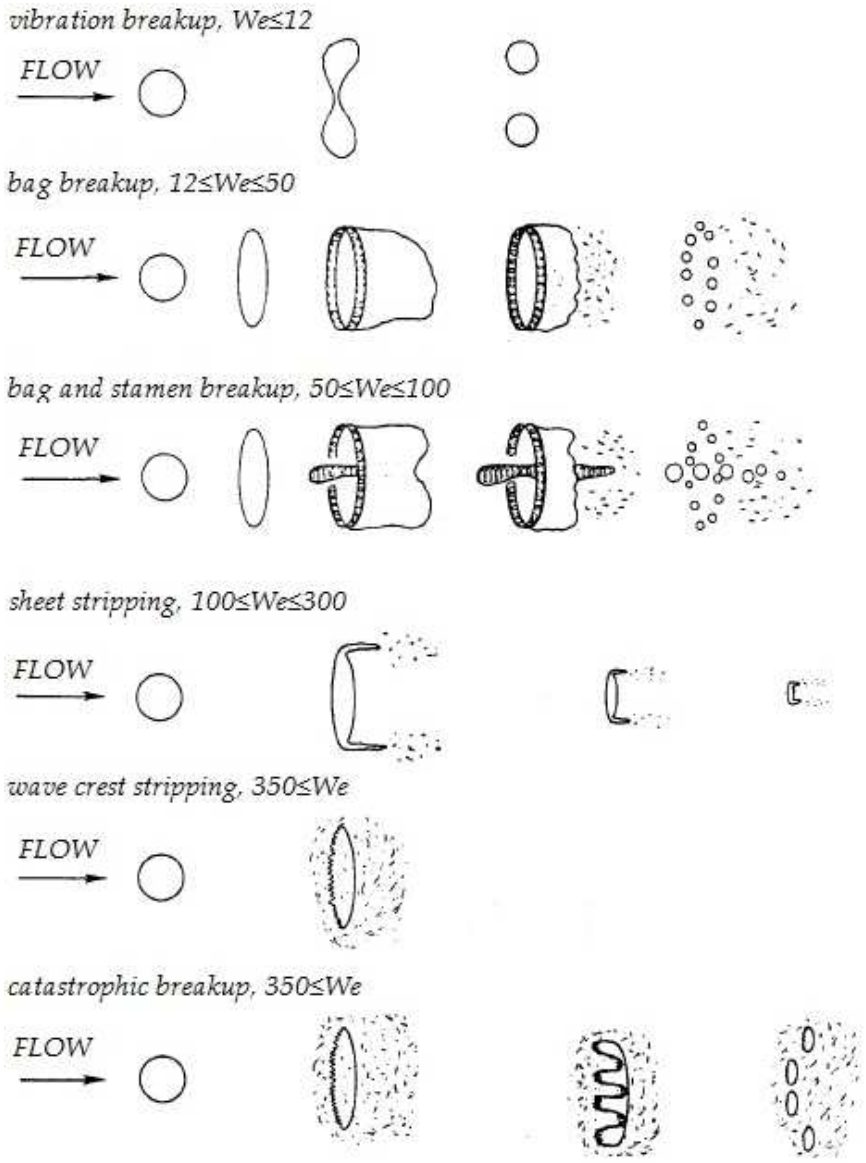

Figure 3.26 Break-up mechanisms as a function of We [77]

3.3.2 Velocity distribution of low butanol flow rates

Since particular emphasis was given in butanol electrosprays operated at relatively low flow rates, it is interesting to observe the velocity variations under these conditions. For that purpose, velocity distributions are provided in Fig. 3.27. In the Figure six plots are presented and are selected to be representative of the regions where close to "cone-jet" behavior was observed in the previous section. As a reminder, these where the regions around 3.4kV and 4.3kV. The velocity distributions for the rest of the applied voltages are located in Appendix A, in Fig. A.12. Narrow distributions are observed in the cases of very low flow rates at the lowest voltages, whereas with increasing voltage the distributions become equally broad showing insensitivity on mass flow rate.

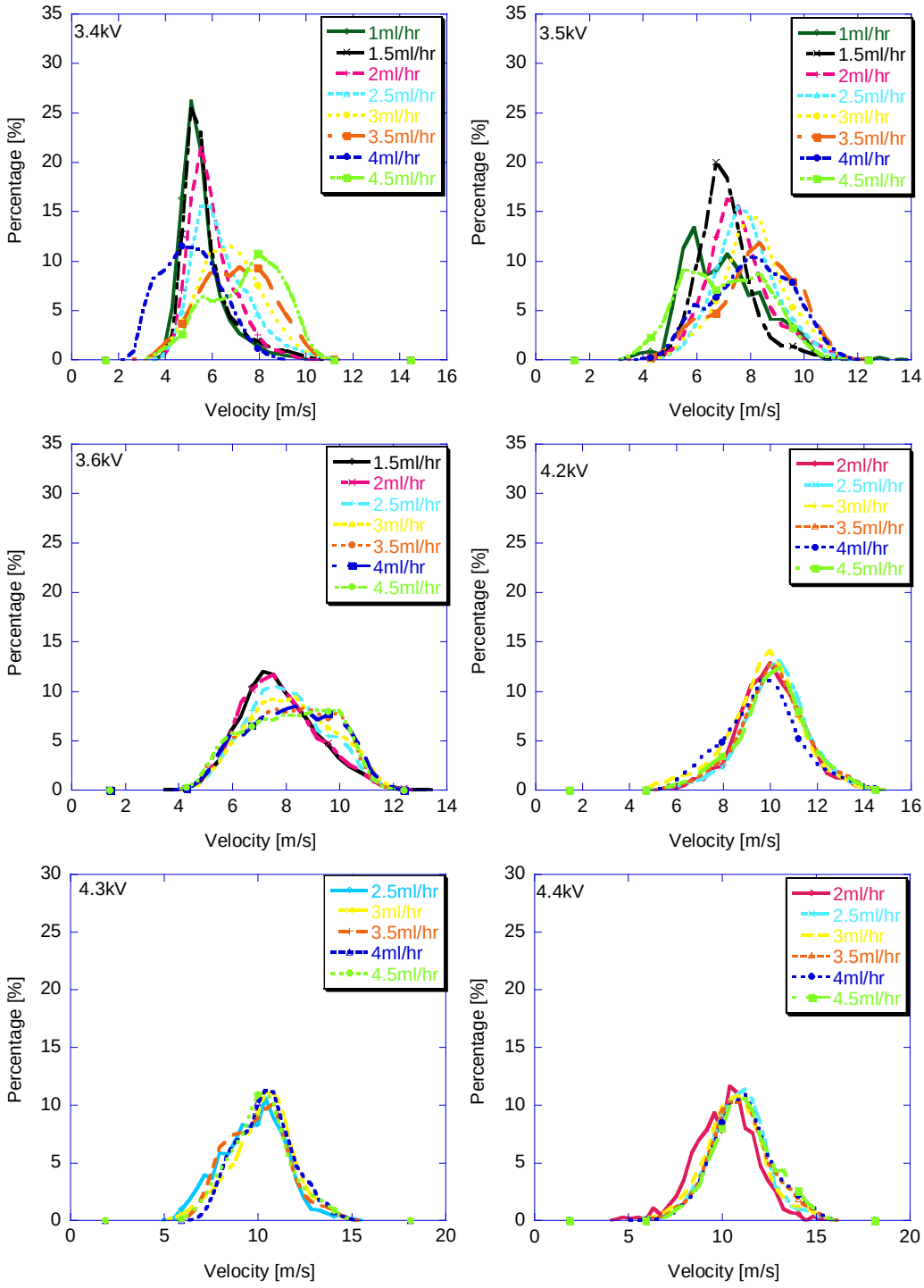

Figure 3.27 Velocity distribution for Butanol at low flow rates and voltages 3.4kV, 3.5kV, 3.6kV, 4.2kV, 4.3kV and 4.4kV

The effects of voltage and flow rate on the average velocity are shown in Fig. 3.28. An increase in droplet velocity is observed with increasing voltage, irrespective of flow rate. Contrary to the negligible flow rate effect, the voltage effect is substantial and translates to higher velocities for higher applied voltages.

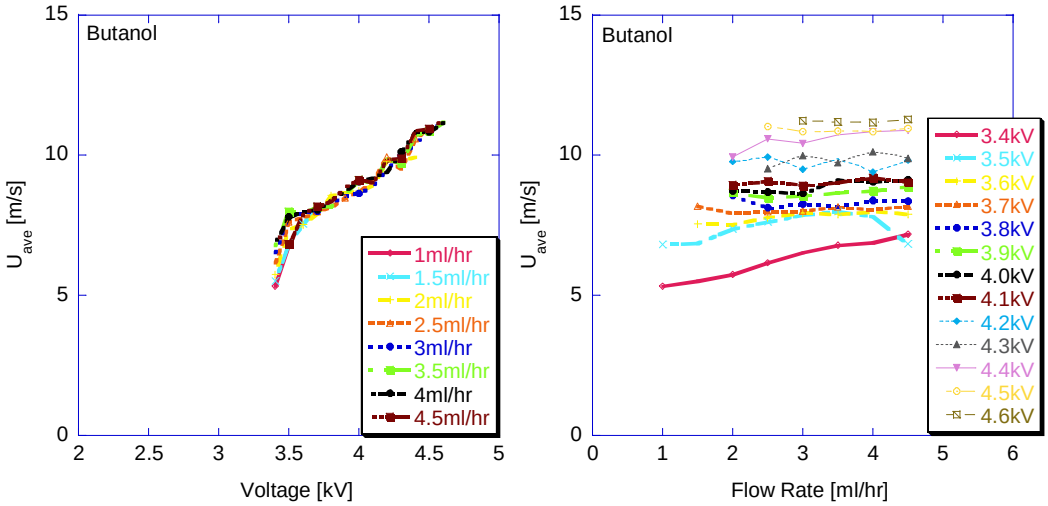

Figure 3.28 Effect of voltage and of liquid flow rate on the mean velocity of Butanol for low flow rates

Similarly to the previous paragraph, Re and We numbers were calculated and are presented in Figs. 3.29 and 3.30 for a constant voltage and flow rate respectively. Following the trends observed in Fig.3.28, Re and We numbers increase with increasing voltage. A transitional flow regime is clearly observed for all cases and Fig. 3.30 shows two regions of monotonic behavior and a drop around 4kV for all flow rates.

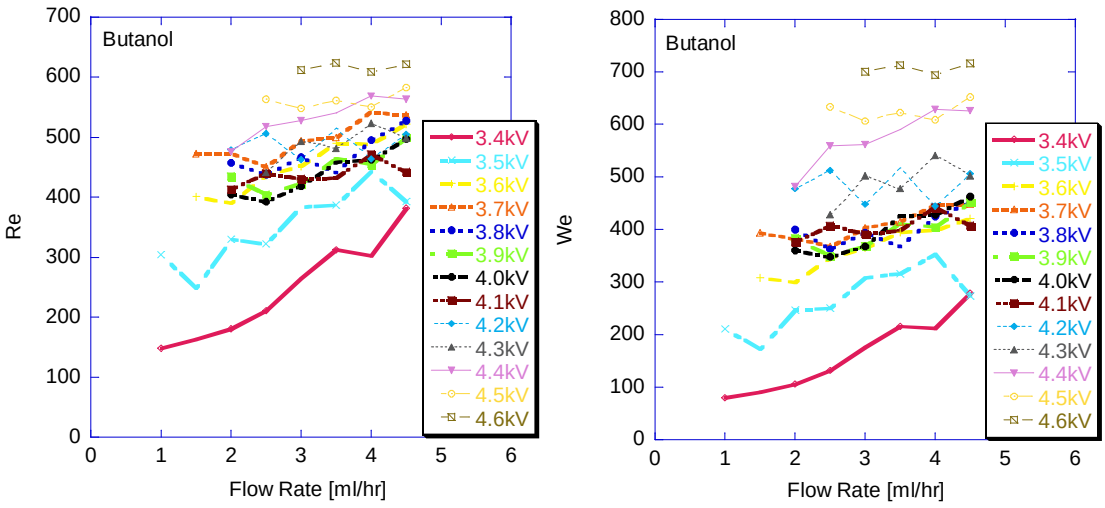

Figure 3.29 Effect of flow rate on Re and We numbers for low Butanol flow rates

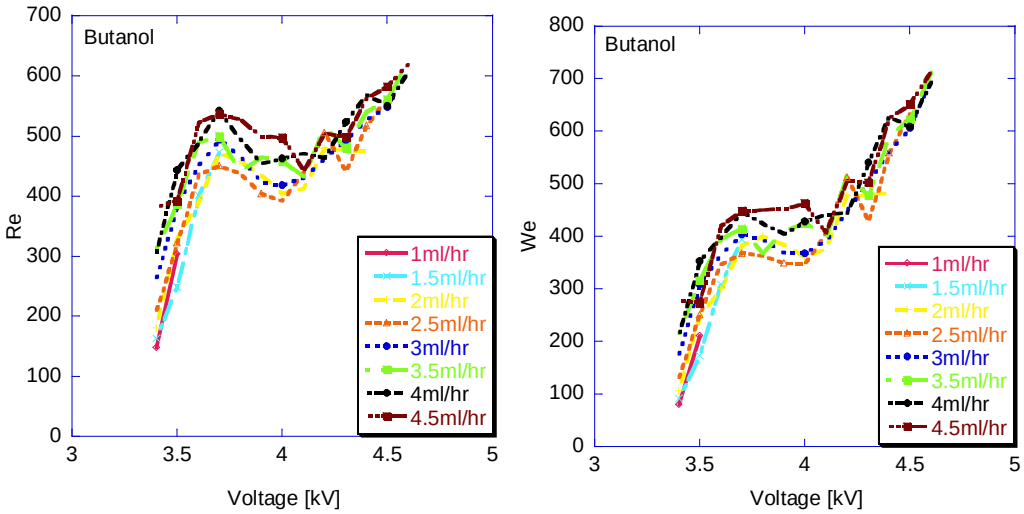

Figure 3.30 Effect of voltage on Re and We numbers for low Butanol flow rates

The Weber number calculation enhances the prediction of the droplet break-up mechanism according to [77]. The We number values are substantially increased when compared with the butanol results of the previous paragraph (Figs. 3.24 and 3.25),

mainly due to the higher average velocities observed for the range of lower flow rates. For that same range, it is reminded, that even though the droplet size distributions revealed an ~18% uniformity in size distribution, which was significantly improved compared to higher butanol flow rates, they were still polydisperse. The source of polydispersion can be attributed to the break-up mechanism for We≥350, which is the *catastrophic* break-up regime. Regions with We≤350 correspond to voltages below 3.6kV, where the narrowest droplet size distributions are observed as well. The *sheet stripping* break-up regime may, for that purpose, enhance the creation of almost uniform size droplets.

3.4 Non-dimensional Controlling Parameters

In this section the possibility is investigated of producing empirical relations among the three governing parameters in the establishment of an electrospray: the droplet diameter, the voltage and the flow rate. According to [23] the non-dimensional droplet diameter is a function of the non-dimensional voltage and flow-rate as well as of the dielectric constant ε of the liquid:

$$d^* = f(Q^*, V^*, \varepsilon) \tag{3.4}$$

Thus, for a specific liquid, d* is a function of V* and Q*. The formulation of the non-dimensional parameters is dependent on the mode of operation of the electrospray and for a stable cone-jet regime it is [23]:

$$Q^* = \frac{\rho \cdot \lambda \cdot Q}{\varepsilon \cdot \varepsilon_0 \cdot \sigma} \tag{3.5}$$

$$V^* = \frac{V - V_0}{V_0} \tag{3.6}$$

$$d^* = \left(\frac{\rho \cdot \lambda^2 \cdot d^3}{(\varepsilon \cdot \varepsilon_0)^2 \cdot \sigma} \right)^{1/3} \tag{3.7}$$

In the above relations, ϱ is the density of the liquid, ε_0 is the electrical permittivity of air and V_0 is the onset voltage, that was taken to be 3kV for this analysis. Expressions 3.5 and 3.7 come from dimensional analysis. It is noted that the expression for d* has some formal resemblance with the Weber number. As indicated in the previous sections, electrosprays of low butanol flow rates present a stable behavior, even though the 10% monodispersity observed in previous studies was not confirmed. It is reminded that for butanol and relatively low flow rates (1-4.5ml/hr), in the vicinity of 3.4kV and 4.3kV the respective percentage was on the order of 18-23%. Thus, in order to calculate the regression coefficients for this analysis, butanol data demonstrating a higher droplet size dispersion, namely cases 3, 4 and 5 (3.6kV-3.8kV) of Fig. 3.15, were neglected from this study. Conducting a surface fit over the non-dimensional data, an empirical relation was generated that correlated d*, V* and Q*. This expression (3.8) was a third order polynomial with a regression coefficient R^2=93.14% and the resulting surface fit is shown in Fig. 3.31. All coefficients of the polynomial are given with 95% confidence bounds.

$$d^* = 3.216 + 36.57 \cdot V^* + 0.02068 \cdot Q^* - 167.3 \cdot V^{*2} - 0.1811 \cdot Q^* \cdot V^* + 0.000565 \cdot Q^{*2} + 209.3 \cdot V^{*3} + 1.305 \cdot Q^* \cdot V^{*2} - 0.006392 \cdot Q^{*2} \cdot V^* + 7.538 \cdot 10^{-6} \cdot Q^{*3} \quad (3.8)$$

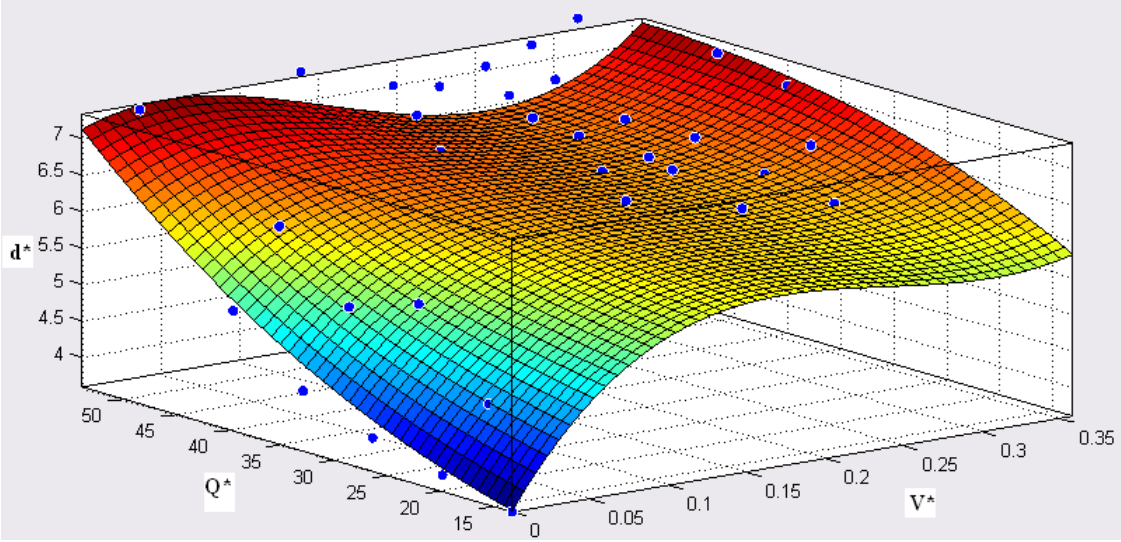

Figure 3.31 Surface fit over the d*=d*(V*,Q*) data

In addition, non-dimensional parameters can be used in order to classify flow regimes as shown in Fig. 3.32. Three different electrospray regimes are presented in the figure, namely intermittent single-jet, continuous single-jet and multi-jet, corresponding to the modes observed with the high-speed videos. Notably, all of them are unsteady and Fig. 3.32a presents the results for the pure substances whereas Fig. 3.32b presents the results for mixtures. In case (a.), it can be seen that heptane appears at low Q*, then butanol occupies an intermediate region of the plot in terms of Q* and finally ethanol is characterized by high Q*. The increase of V* favors multi-jet electrospray regimes, whereas at lower V* continuous single-jet sprays are mostly observed. The intermittent regime is favored in the region of intermediate values of Q* and V*. Notably, this regime

appears only for mixture 1 at the right panel of the figure. In this plot, it can be also seen that multi-jet regimes appear exclusively at high V*. At intermediate V* and low Q* the multi-jet regime is favored as well. Finally, at low V* continuous single-jets appear.

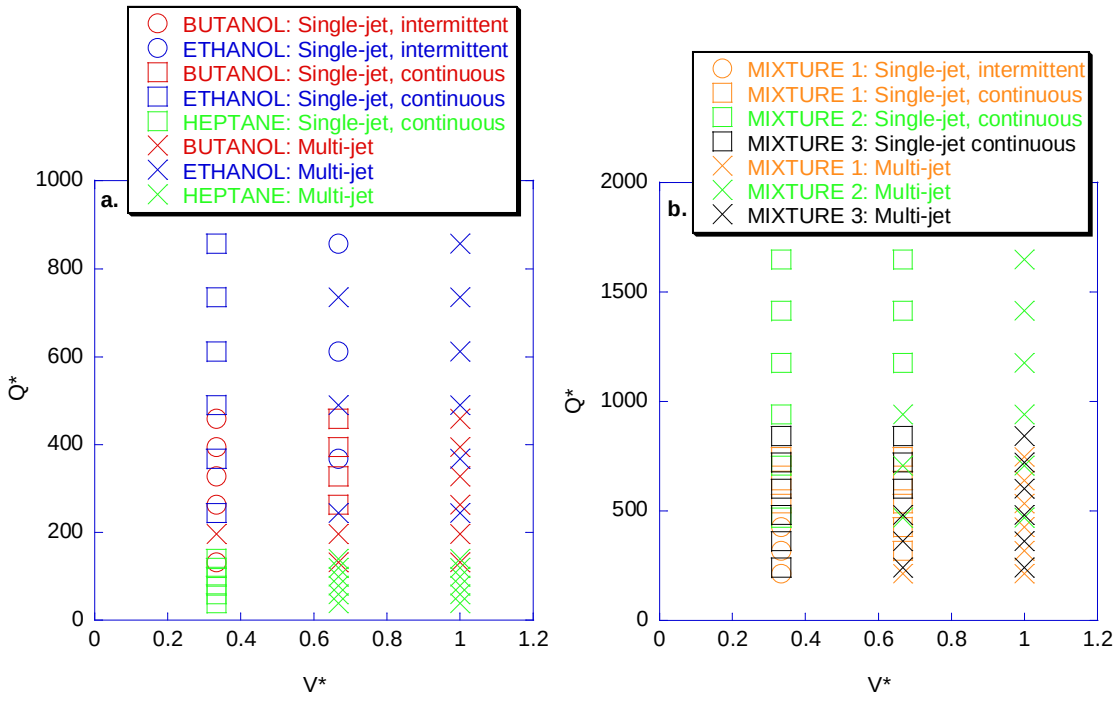

Figure 3.32 Electrospray regimes for a. butanol, ethanol, heptane and b. mixture 1, mixture 2 and mixture 3, based on non-dimensional flow rate Q* and voltage V*

3.5 Butanol Sprays Generated with Steel Injectors

As pointed out in Chapter 2, a series of butanol e-sprays were established using steel capillaries. These capillaries were manufactured using EDM (electrical discharge machining) for the creation of the conical tip. The technique of melting the material changes the surface texture, but it was able to keep the hole of the capillary relatively flat with few obstructions at the edge of the hole. However, this process could not provide

sufficient accuracy with respect to the location of the nozzle-hole on the conical surface, given the small diameter of the nozzles (0.0010 in), as shown in the image of Fig. 3.33.

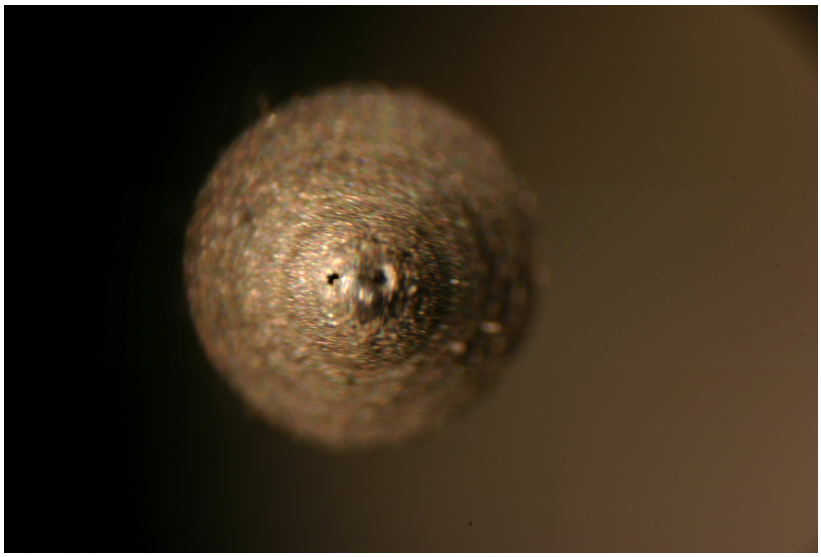

Figure 3.33 The nozzle hole location on the conical tip after EDM process

Given that the electrical field can be enhanced locally by sharp features of the surface roughness [5, 6, 21], there was increased suspicion that the quality of the results could have been influenced. Compared to glass injectors used to overcome this difficulty, steel nozzles are much cheaper and sturdier and therefore worthy of investigation. A comparison related to both injector types is provided in section 3.5.3.

3.5.1 Electrospray visualization of butanol e-sprays from steel capillaries using digital photography

Spray imaging was conducted using the Canon EOS Digital Rebel camera and laser light as illumination source. In Fig. 3.34 these results are presented and each row corresponds to a different flow rate.

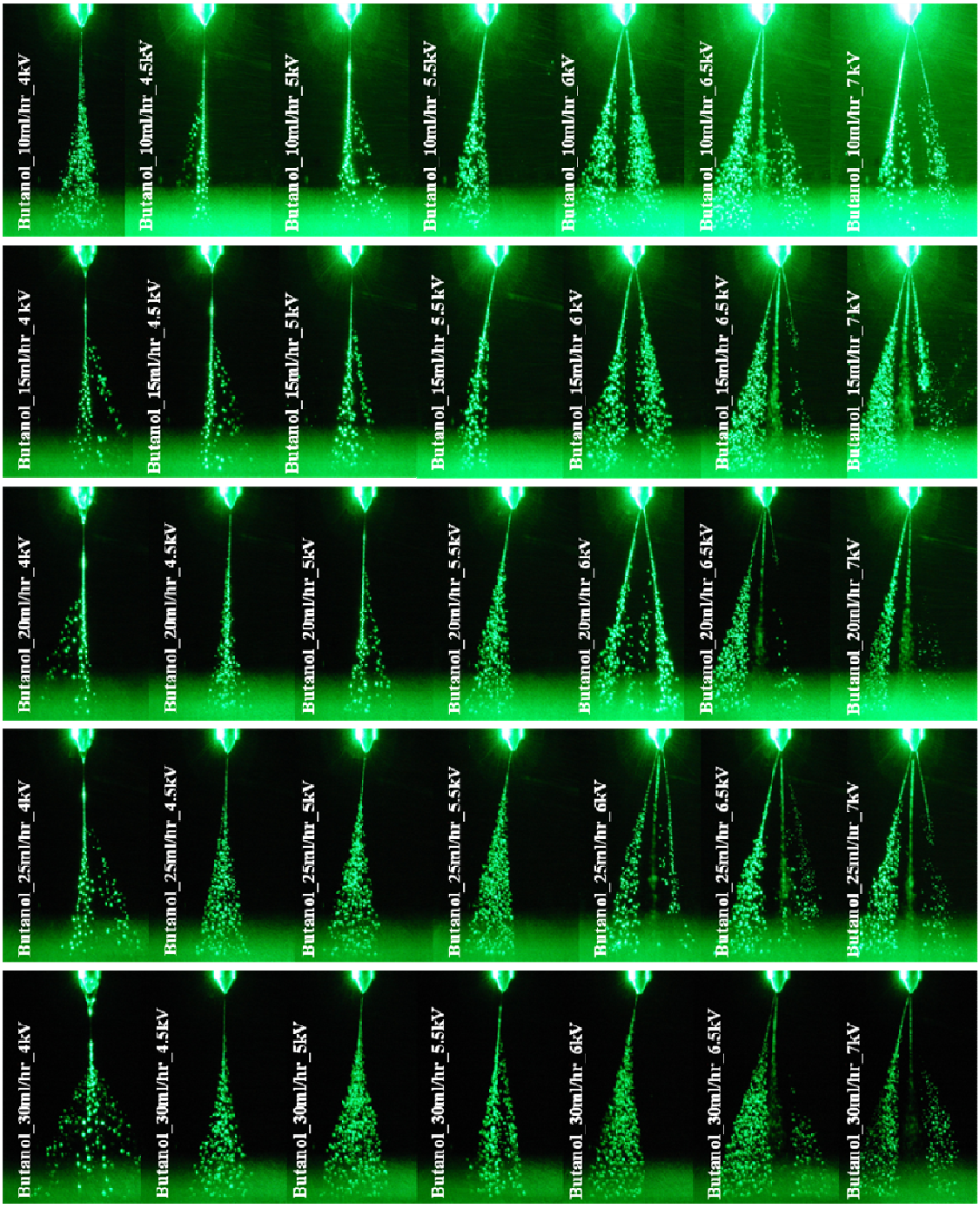

Figure 3.34 Butanol e-spray imaging with the Canon EOS Digital Rebel camera

These flow rates start from 5ml/hr and progress to 30ml/hr with an increment of 5ml/hr. The columns represent different applied voltages, which vary from 4kV-7kV with an increment of 500V. For voltages below 6kV, one emissive cusp is observed for all flow rates. The single jet is developing in the vertical direction for the lowest voltages (4-4.5kV), whereas, spray shifting occurs starting at 5kV and is more intense for higher flow rates. Multi-jet sprays appear at voltages above 6kV for all flow rates, revealing an unsteady behavior similar to the one observed in the previous sections through high-speed imaging.

3.5.2Structure of e-sprays emitted from steel capillaries

For the butanol electrosprays generated using steel capillaries, distributions of droplet size as a function of mass flow rate per spray and applied voltage are shown in Fig. 3.35a-f. Results are presented for flow rates of 5-30 ml/hr with an increment of 5ml/hr and applied voltages between 4 and 7 kV. Establishment of the electrospray was not possible for lower voltages, whereas for higher voltages, several unsteady spray configurations were observed that do not belong in the “cone jet” mode. Even for such sprays, several important differences were observed with previous results published with both ethanol and low-conductivity fuels [5, 6, 23, 25].

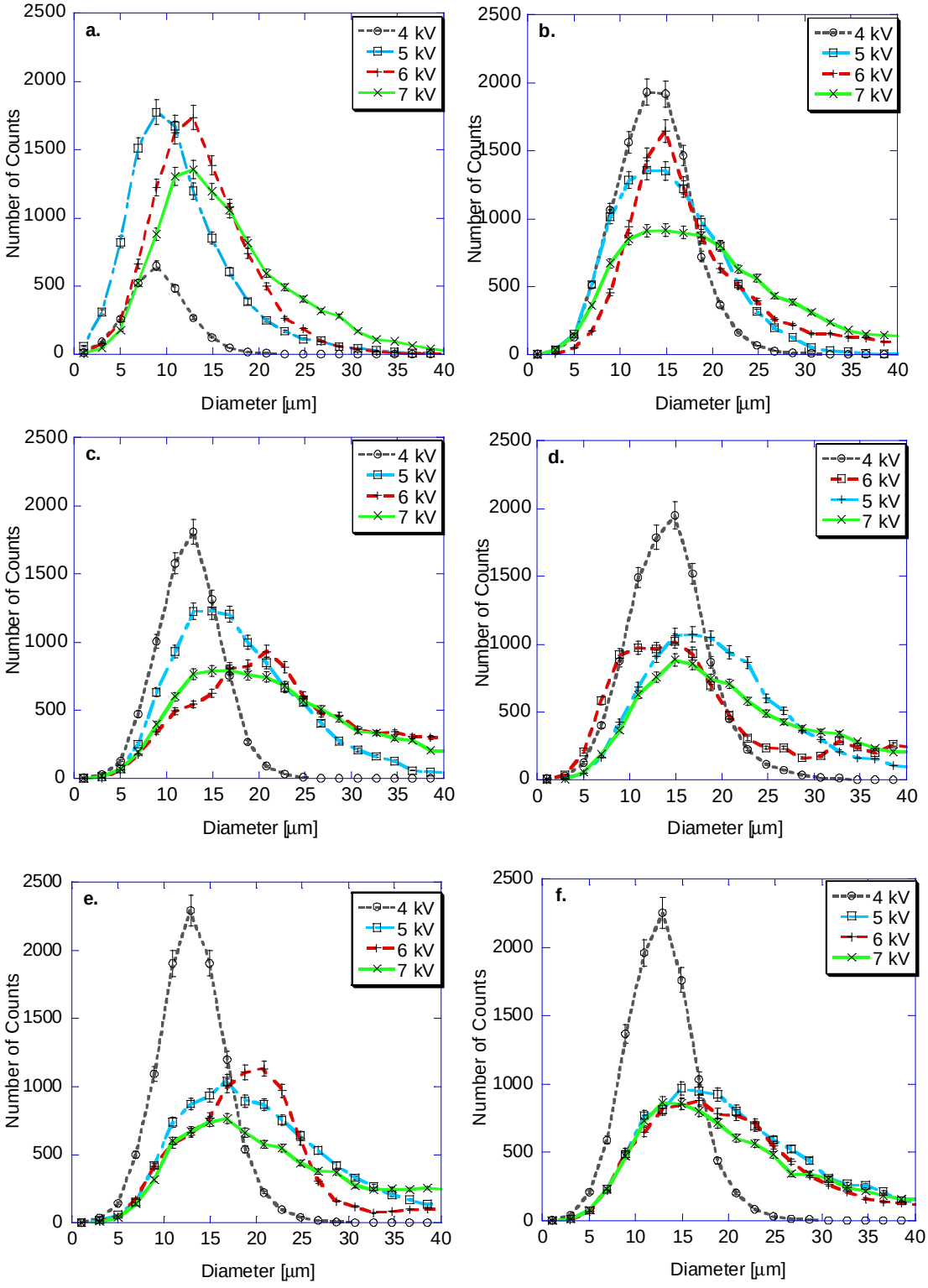

Figure 3.35 Distribution of the droplet diameter for flow rates (a) 5ml/hr, (b) 10ml/hr, (c) 15ml/hr, (d) 20ml/hr, (e) 25ml/hr and (f) 30ml/hr

First, it is shown that the butanol electrosprays under consideration are not monodisperse. For all flow rates, the size distribution was narrowest at the lowest applied voltage (4 kV), but even at this voltage it is far from been a "Dirac"-type function. As flow rate increases, increase in size dispersion is observed for intermediate values of voltage (5-6kV). Notably, for an applied voltage of 7kV, the droplet size distribution is unaffected by mass flow rate. Similarly, for the lowest applied voltage of 4kV, the dependence of size distribution on flow rate is very mild and the narrowest size distribution is practically unaffected by flow rate. This result constitutes a second important difference from previous published results that indicate a minor effect of applied voltage on hydrocarbon electrosprays, for which fluid conductivity varied between 0.7 and 9.8 x 10^{-8} $(\Omega cm)^{-1}$ [5, 6].

The dependence of droplet size on both flow rate and applied voltage was further investigated. Results are presented in Figs. 3.36 and 3.37 that report measurements of Sauter mean (d_{32}) and average (d_{10}) diameters respectively as a function of these two parameters. A first observation that can be made is that under constant applied voltage, there is an increase in droplet size with increasing flow rate. For the average diameter, this trend is demonstrated in Fig. 3.37, whereas the few points indicating a decrease in Sauter mean diameter with flow rate are probably due to the poly-dispersion indicated in Fig. 3.35. Since for this mean, a calculation of d^3 is necessary, the effect of large droplets is exacerbated and may skew the calculation. In

general, the results are in agreement with the already established finding that droplet size can be decreased with diminishing flow rates.

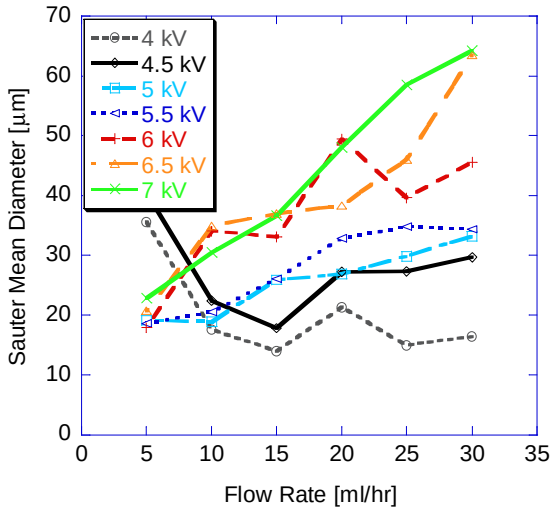

Figure 3.36 Variation of the droplet Sauter mean diameter (d_{32}) with mass flow rate, for applied voltages 4-7kV

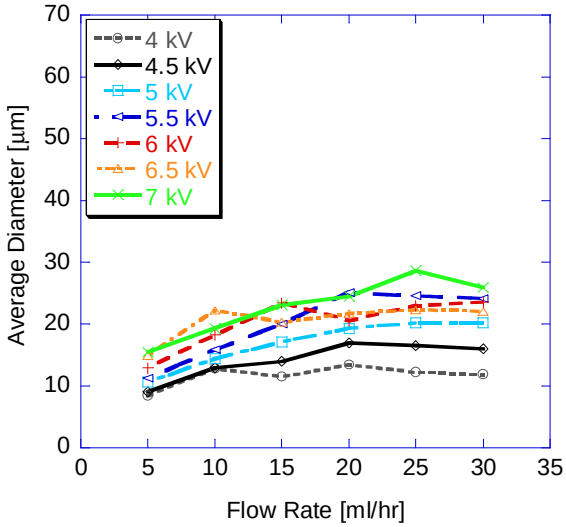

Figure 3.37 Variation of the droplet average diameter (d_{10}) with mass flow rate, for applied voltages 4-7kV

Equally important are the results that relate to the dependence of d_{10} and d_{32} on voltage that are reported in Figs 3.38a,b-3.39a,b. For each definition of the mean

diameter, a set of relatively large and relatively small flow rates is presented, for the purposes of clarity.

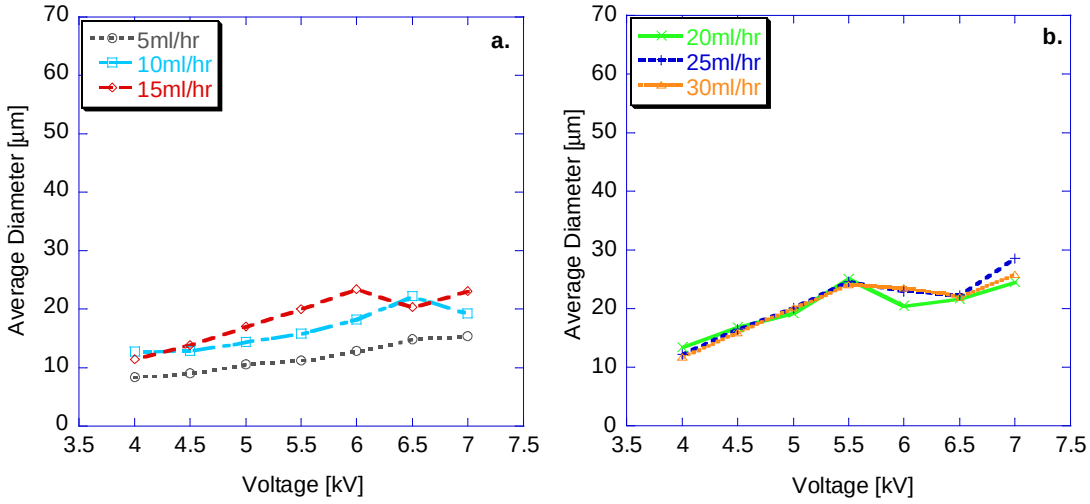

Figure 3.38 Droplet average diameter (d_{10}) as a function of applied voltage, for flow rates (a) 5-15ml/hr, (b) 20-30ml/hr

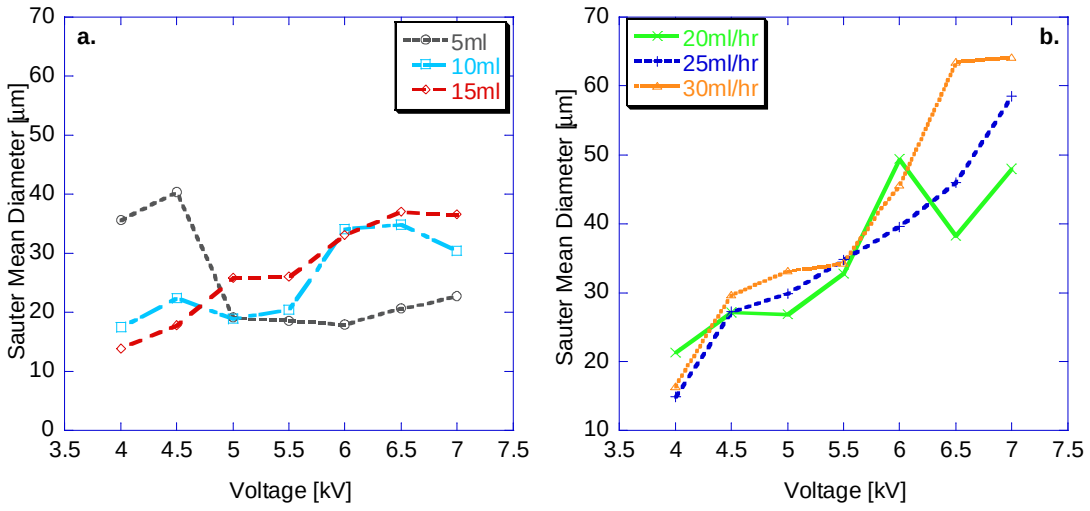

Figure 3.39 Droplet Sauter mean diameter (d_{32}) as a function of applied voltage, for flow rates (a) 5-15ml/hr, (b) 20-30ml/hr

Two points are worth highlighting with regard to comparison with results in hydrocarbon electrosprays: First, it is noted that there is an increase in droplet size with increasing applied voltage. This is in contradiction with the results of [5, 6] which show, that when there is an effect of the applied voltage, this tends to lead to diminishing droplet diameter with applied voltage. It is also noted that non-monotonic phenomena are observed in the vicinity of 5-5.5 kV which may signify a transition between the regimes of electrospraying outlined in [27]. Second, for relatively high flow rates (20-30 ml/hr) the dependence of droplet size on applied voltage seems not to depend significantly on the particular flow rate. (For the case of d_{10}, this is a much stronger conclusion than for the case of d_{32}. The difference is due to the poly-dispersion of the sprays). For lower flow rates though (5-15 ml/hr), the dependence on voltage is different for different flow rates. This compares interestingly with the findings of [5, 6] that show an insensitivity of heptane droplet size on voltage for a set flow rate at flow rates smaller than an order of 10 ml/hr. For higher flow rates, those results recorded a decrease of droplet size with increasing voltage, as discussed in the previous paragraph.

3.5.3 Comparison of steel and glass capillaries

As seen in the previous paragraphs, the electrosprays generated by steel injectors were polydisperse for all applied conditions. The source of this polydispersion could have been the surface roughness at the capillary tip, however other factors should also have contributed to this effect, as shown by the analysis based on We in section 3.3. In

these data, the difficulty of producing droplets of uniform size was demonstrated, even when it was investigated in a narrow range of voltages and flow rates. In general, it can be stated that using nozzles of significantly reduced surface roughness does improve monodispersity, but only mildly. Even when surface roughness was virtually eliminated with use of glass, monodispersity was not achieved.

3.6 Butanol Conductivity Measurements

In order to investigate further the possible causes of polydispersion of butanol electrostatic sprays, another factor deserves further study. Specifically, the results of Fig. 3.40 show a significant increase in the measured conductivity of butanol as a function of the applied electrical field.

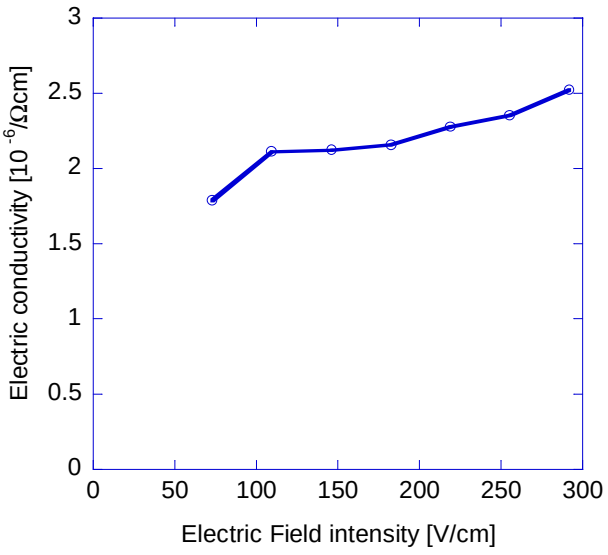

Figure 3.40 Variation of the electrical conductivity σ of butanol with electrical field intensity

Electrical conductivity was measured with the use of the apparatus of Fig. 2.1 and equations (2.9) and (2.10). The electrical field intensity is equal to the voltage applied to the butanol cell of Fig. 2.1 divided by the cell length. The measured values of conductivity are on the same order of magnitude like the ones reported in [73]. It can be seen however, that there is a possibility of an increase in electrical conductivity on the order of 30% for an increase of the applied electrical field intensity to a value of 300 V/cm, which is moderate compared to the electrical fields used in [6, 17, 18, 22].

In all these previous studies electrical conductivity was treated as a constant property of the fluid. This can be potentially very important since the "cone-jet" mode that is necessary for the establishment of mono-disperse sprays is directly affected by fluid conductivity. In previous studies, it has been established that the *domain* of conditions (voltages and flow rates) for which the cone jet mode can be sustained shrinks with increasing fluid conductivity [74-76]. Actually, there is a conflict in the existing literature concerning whether or not there exists an upper limit to the liquid electrical conductivity for the establishment of stable electrosprays [5, 23, 74-76]. As a result, the recorded increase of butanol conductivity may lead to an electrospray *domain* of operation (voltages and flow rates), where it is infeasible to establish "cone-jet" electrosprays.

At the heart of the matter lies the fact that butanol is a liquid of intermediate conductivity. Specifically, the conductivity of butanol is on the order of $3 \cdot 10^{-4}$ $1/\Omega m$, whereas the conductivity of heptane with the addition of conductivity enhancers is on

the order of 10^{-6} 1/Ωm and of an electrolyte 10^{-2} 1/Ωm. So, butanol e-sprays develop in a manner that is different than these two widely studied groups of liquids.

3.7 Summary

In summary, it can be stated that sprays of bio-butanol are amenable to electrostatic manipulation. However, the monodispersion that was perceived as an important advantage of previous e-spray applications (e.g. analytic chemistry) is practically non-achievable for the range of droplet sizes, velocities and nozzle configurations that should pertain to automotive applications. This was supported by results of electrospray phenomenology and structure obtained for butanol, demonstrating a polydisperse behavior, whereas stable butanol electrosprays were achieved within a narrow region of low flow rates. Extensive comparisons were performed between electrosprays of butanol, ethanol and heptane with a 2% Stadis enhancer. In addition, the electrospray behavior of three mixtures of the aforementioned fuels that had the same electrical conductivity and surface tension was investigated. Several factors were identified that were responsible for this lack of monodispersity, namely the e-spray menisci oscillations, the instabilities initiating the droplet break-up, secondary droplet break-up because of high We and finally the degree to which butanol electrical conductivity was constant.

However, it is noted that monodispersity may actually not even be desirable. These adverse effects of spray instability and high-We droplets on monodispersity are

most probably outweighed by enhanced mixing prior to combustion. It is also noted that the flow rates under consideration (5-30 ml/hr), were not of the same order of magnitude as in existing automotive applications. A possible way to overcome this caveat is multiplexing the electrosprays on distributors that will be micro-fabricated on silicon similar to [78] so that they consist of hundreds of independent sprays and hence, realistic flow rates on the order of 1-10 l/hr are achieved.

CHAPTER 4

BUTANOL COUNTER-FLOW FLAMES

In the following sections, counter-flow flame results on the performance of this novel biofuel are presented and are divided into four categories.

- First, extinction strain rates were measured experimentally and compared with the corresponding values for already well-established fuels (ethanol and methane), as well as with butanol-methane mixture combinations. This is an important measure of the capability of butanol flames to withstand extinction in practical, turbulent flow fields.
- Then, major combustion species were measured across the counter-flow flames so that their structure is determined as a function of the imposed strain rate. The species concentration measurements were obtained using line-Raman imaging for O_2, N_2 and C-H bond.
- In addition, temperature distributions across the counterflow-flames are provided.
- Finally, in the last section of this chapter, an important combustion parameter, the scalar dissipation rate, is approximated through the mixing layer thickness δ, which was estimated using two different approaches.

In this analysis, strain rate, composition of the counter-flowing streams, total heat released from combustion and overall equivalence ratio were the controlling

parameters, so a brief discussion is necessary on how these quantities were determined before specific results are presented.

4.1 Calculation of Controlling Parameters

The data that were measured directly during the experimental process were mass flow rates of the reacting streams and temperatures at the axis of the burner, in between the nozzles. In order to estimate the strain rate K for each test case, as suggested in [37], the densities and speeds of the fuel and oxidizer flow streams at the exit nozzles had to be calculated. Assuming mixture of ideal gases at the exit of the burner, the density ρ was calculated through the equation:

$$\rho_i = \frac{\dot{m}_{tot}}{\dot{V}_{tot}} = \frac{P_{atm} MW_{mix\,i}}{\overline{R} T_i} \tag{4.1}$$

The subscript i denotes either the fuel or oxidizer stream, $\dot{m}_{tot}$ and $\dot{V}_{tot}$ are the total mass and volumetric flow rates reaching the nozzle respectively, $\overline{R}$ is the ideal gas constant (8314 J/kmol K), T is the measured temperature and P_{atm} is the atmospheric pressure. MW_{mix} is the molecular weight of the mixture, calculated as:

$$MW_{mix} = \frac{1}{\sum_{1}^{j} \frac{y_j}{MW_j}} \tag{4.2}$$

where y_j and MW_j are the mass fraction and molecular weight of the species *j* in either the fuel or the oxidizer stream. It is noted that y_i is known because the mass flow

rate of each of the metered components is known. Once ρ_i is known from eq. (4.1), the speeds U_i of the counter-flowing streams can be calculated through:

$$U_i = \frac{\dot{m}_{tot,i}}{\rho_i A} \tag{4.3}$$

where A is the surface area at the nozzle exit location. Then, the strain rate K was estimated using the approximation that was suggested in [37]:

$$\mathrm{K}=\frac{2U_{ox}}{d}\left[1+\frac{U_{fuel}}{U_{ox}}\left(\frac{\rho_{fuel}}{\rho_{ox}}\right)^{\frac{1}{2}}\right] \tag{4.4}$$

The calculation of the overall equivalence ratio ϕ, for each of the fuels under consideration, was based on the global combustion reactions for butanol, methane and ethanol respectively:

$$C_4H_9OH + 6O_2 \rightarrow 4CO_2 + 5H_2O \tag{4.5}$$

$$CH_4 + 2O_2 \rightarrow CO_2 + 2\,H_2O \tag{4.6}$$

$$C_2H_5OH + 3O_2 \rightarrow 2CO_2 + 3H_2O \tag{4.7}$$

Then, eq. 4.8 was used to calculate ϕ:

$$\varphi = \frac{F/O}{(F/O)_{st}} \tag{4.8}$$

where (F/O) is the fuel to oxidizer ratio and $(F/O)_{st}$ the stoichiometric one and was calculated from the metered mass flow rates of fuel and oxidizer. In the test cases of butanol-methane mixture flames both combustion reactions (4.5, 4.6) were considered in the calculation of ϕ. Finally, the total combustion heat release Q_{tot} was calculated based

on the lower heating values of the fuels which are equal to 33.1 MJ/kg for butanol, 50.0 MJ/kg for methane and 28.9 MJ/kg for ethanol [63].

4.2 Butanol Extinction Strain Rate Measurements

4.2.1 A comparison with flames of ethanol, methane and a butanol-methane mixture

Extinction strain rate measurements were performed for three cases of butanol mass flow rates equal to $6.289 \cdot 10^{-6}$, $7.187 \cdot 10^{-6}$ and $7.861 \cdot 10^{-6}$ kg/s (cases A, B, and C respectively) - see Table 4.1. Strain rates at extinction are reported in Figs. 4.1 and 4.2 as a function of the overall equivalence ratio from ϕ=0.70 to ϕ=1.3. A brief discussion is necessary of the use of the overall equivalence ratio as a controlling parameter. It is of course realized that the flames under consideration are non-premixed, so the reactants always mix at a stoichiometric proportion at the flame. However, as discussed in [79, 80], this does not diminish the importance of the overall fuel/oxidizer proportion, which determines e.g. the relative position of the flame and the stagnation plane. Overall F/O in the non-premixed flame does not control the energetics of the flame (flame temperature, flame speed etc.) but has a strong effect on the mixing and is therefore a relevant parameter.

In Figs. 4.1 and 4.2, extinction strain rates of butanol are compared with the corresponding extinction strain rates of a series of other fuels for a range of overall

stoichiometries. Focusing on the butanol flames for a moment, in each flame, the amount of fuel was kept constant and the oxidizer varied in order to vary overall ϕ. In this manner, the total heat released by each flame case remained unaffected. The flame was kept in the middle of the gap between the nozzles by appropriately adjusting the flow of the diluent (nitrogen). Then, the same process was followed for methane, ethanol, and a mixture of butanol and methane that was 63% per mass in butanol, a composition that was arbitrarily selected. For each of the three panels (a, b and c) in Fig. 4.1, the total heat release is equal to the one of the corresponding butanol case. In Table 4.1, the flow rates used in order to establish each of the flames for an overall equivalence ratio of 1.0 are presented in detail. Tables containing this information for the other overall equivalence ratio values can be found in Appendix B.

Butanol, ethanol, methane and the butanol/methane mixture are denoted with the appropriate subscript and indicate the flames in Fig. 4.1, for which the heat release is the same for all fuels with the additional subscript "HR". Similarly, in Fig. 4.2 (a, b, and c) flames of the four fuels for which the fuel flow rate (not the total heat release) is kept constant and equals the corresponding butanol one are compared. These cases are indicated in Table 4.1 with the subscript "FFR". In addition to the mass flow rates for each flame configuration, Table 4.1 presents, in the last two columns, the estimated strain rate K, as well as the total heat release from combustion Q_{tot}.

Table 4.1 Mass flow rates at extinction, extinction strain rates and total heat released for flames of an overall equivalence ratio ϕ=1.0. Butanol, methane, ethanol and a butanol-methane mixture are considered and compared for cases of equal total heat released (HR) and equal total fuel flow rate (FFR)

Test Case	Alcohol	N_2 in alcohol stream	CH_4	Total Fuel	N_2 in CH_4 stream	O_2	N_2 in O_2 stream	K_{ext}	Qtot
	[x10^{-6}kg/s]	[x10^{-6}kg/s]	[x10^{-6}kg/s]	[x10^{-6}kg/s]	[x10^{-6}kg/s]	[x10^{-6}kg/s]	[x10^{-6}kg/s]	[s^{-1}]	[W]
A but_HR	6.29	9.41	0.00	6.29	27.35	16.31	19.84	110.0	208.0
A meth_ HR	0.00	0.00	4.14	4.14	35.28	16.58	37.15	149.4	207.2
A eth_ HR	7.19	12.16	0.00	7.19	21.62	9.99	19.84	99.9	207.5
A mixt_ HR	3.37	12.16	1.92	5.29	33.69	16.42	26.66	134.7	207.6
A meth_ FFR	0.00	0.00	6.29	6.29	60.06	25.12	45.71	181.3	314.0
A eth_ FFR	6.29	12.16	0.00	6.29	21.98	8.73	13.31	87.6	181.6
A mixt_FFR	4.02	12.16	2.27	6.29	31.08	19.45	26.66	136.1	246.2
B but_HR	7.19	9.41	0.00	7.19	32.07	18.67	26.66	131.2	237.7
B meth_ HR	0.00	0.00	4.75	4.75	65.12	18.79	25.29	176.4	237.6
B eth_ HR	8.24	12.16	0.00	8.24	22.72	11.45	26.66	115.1	237.9
B mixt_ HR	3.84	12.16	2.21	6.05	37.14	18.79	33.47	154.2	237.5
B meth_ FFR	0.00	0.00	7.19	7.19	71.91	28.72	58.09	219.7	359.0
B eth_ FFR	7.19	12.16	0.00	7.19	21.62	9.99	19.84	99.9	207.5
B mixt_FFR	4.60	12.16	2.59	7.19	38.65	22.32	26.66	151.7	282.1
C but_HR	7.86	9.41	0.00	7.86	25.95	20.33	33.47	135.8	260.0
C meth_ HR	0.00	0.00	5.19	5.19	59.42	20.44	37.15	192.5	259.7
C eth_ HR	9.01	12.16	0.00	9.01	20.12	12.53	26.66	113.6	260.0
C mixt_ HR	4.27	12.16	2.38	6.65	41.56	20.55	33.47	163.5	259.9
C meth_ FFR	0.00	0.00	7.86	7.86	74.34	31.46	64.41	236.4	393.2
C eth_ FFR	7.86	12.16	0.00	7.86	27.70	10.94	19.84	110.5	227.1
C mixt_FFR	5.03	12.16	2.83	7.86	55.54	24.31	33.47	189.8	307.3

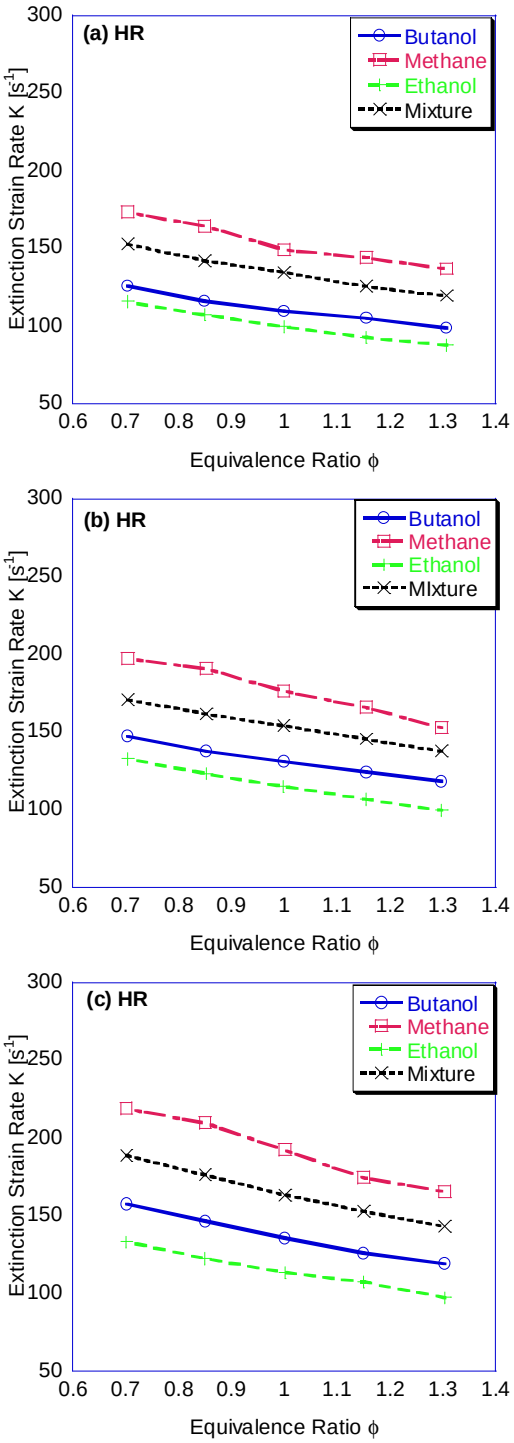

Figure 4.1 Extinction strain rates as a function of the overall equivalence ratio for four different fuels. Heat release (HR) is equal to 208W for (a), 238W for (b) and 260W for (c)

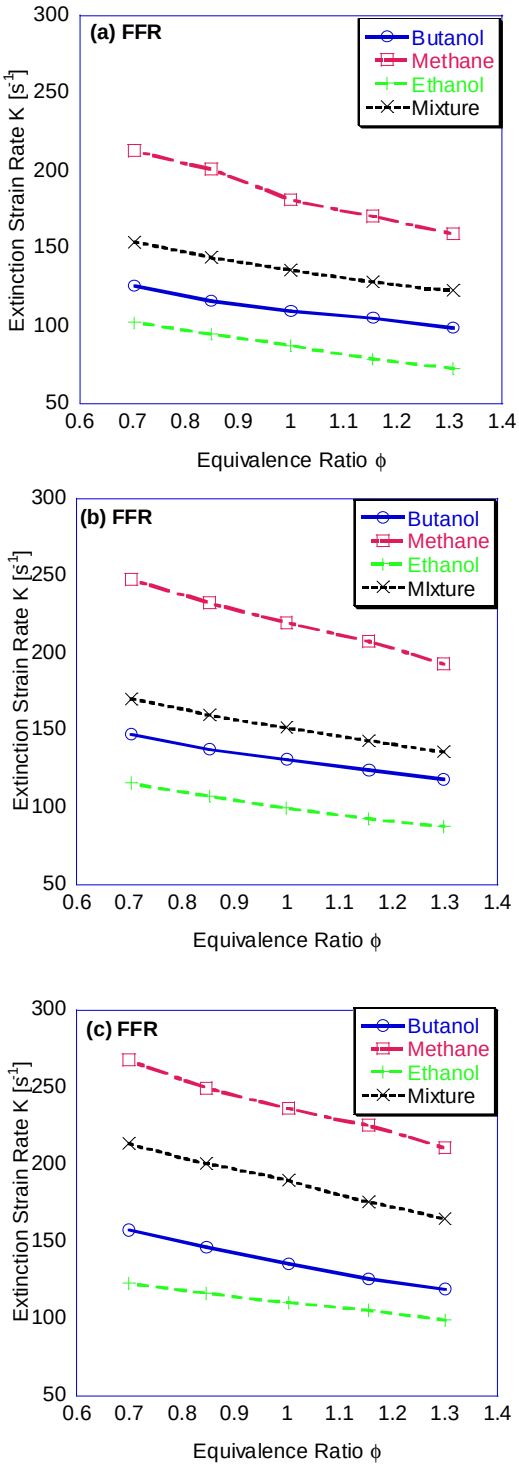

Figure 4.2 Extinction strain rates as a function of ϕ for four different fuels. Fuel flow rates (FFR) are equal to 6.289E-6kg/s for (a), 7.187E-6kg/s for (b) and 7.861E-6kg/s for (c)

The results of Figs. 4.1 and 4.2 show that methane flames are the ones that can sustain the highest strain rates, whereas ethanol flames are the ones extinguishing at the lowest strain rates. Extinction strain rates for butanol lie between the ones of the other pure fuels, thus revealing a behavior significantly improved compared to ethanol. Perhaps the most intuitive results to explain are the ones with constant fuel flow rate in Fig. 4.2. Methane is the fuel with the highest heating value, since it contains no oxygen in its molecule, hence its combustion is more vigorous than that of both butanol and ethanol delivered at the same flow rate. From the energy content perspective, methane is followed by butanol, which has a longer carbon chain than ethanol, and its molecule has a significantly lower percentage of oxygen.

The results of Fig. 4.1 show that the differences between the various fuels are smaller than the ones observed in Fig. 4.2, however the relative ranking of several fuels still persists and this can be explained using the data of Table 4.2. There, we examine the hypothetical case of a flame of overall stoichiometric composition that would release 1 kW of heat. It can be seen that for a constant heat release, the methane flame employs a higher flow rate of oxygen, which means that it sustains a higher strain rate. The argument can be extended to any overall stoichiometry, thus showing that the methane flames sustain higher strain rates for the same heat release.

Table 4.2 Oxygen and fuel flow rates for a hypothetical flame of overall stoichiometric composition that would release 1 kW of heat

Fuel	Lower heating value [MJ/kg of fuel]	F/O [kg fuel/ kg oxygen – stoichiometric]	Fuel flow rate for a total heat release of 1 kW [x10^{-5} kg/s]	Oxygen flow rate for a heat release of 1 kW [x10^{-5} kg/s)]
Methane	50.0	4.00	2.00	8.00
Butanol	33.1	2.59	3.02	7.82
Ethanol	28.9	2.10	3.46	7.27

For all fuels under consideration, the extinction strain rate decreases monotonically as the overall equivalence ratio increases. This trend is contrary to the one observed in premixed flames where extinction strain rate presents a maximum in the vicinity of stoichiometric combustion following the shape of the adiabatic flame temperature distribution [81]. It is noted however, that in the case of non-premixed flames, overall stoichiometry relates to mixing, not to heat release from the flame. The overall "richer" the composition, the farther the stoichiometric surface (where the diffusion flame will be established) lies from the stagnation plane into the oxidizer stream. This means that the parent fuel has to be carried farther against a counter-flowing stream and an increasing temperature gradient, which will start pyrolizing the fuel. This would make overall "richer" flames more vulnerable to extinction.

In Fig. 4.3, the experimentally measured extinction strain rate of a non-premixed butanol-methane flame is compared with the result of two calculations. Specifically, the weighted average of the extinction strain rates of the flames of the two pure components based on both the molar and the mass fractions of the components of the mixture are calculated.

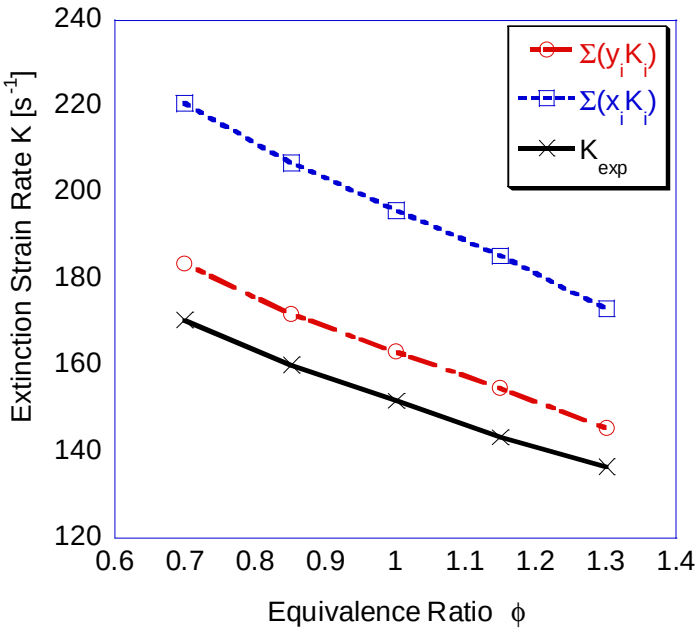

Figure 4.3 Experimentally measured strain rate of extinction of a butanol-methane mixture flame (x) compared with a weighted average of the extinction strain rates of the flames of the pure components on a molar (□) and a mass (o) basis

It is worth highlighted that the experimentally measured strain rate of extinction is smaller than both averages would predict, i.e. that the mixture is more vulnerable to extinction than any "reasonable" linear combination of its components. Notably the experimental result is much closer to a mass-based average, which is expected since strain is fundamentally connected to convective mass transport.

4.2.2 A comparison with butanol, methane-assisted, flames

In this section, six butanol-methane mixture cases are considered. They are named M1-M6 and their flow rates at extinction are presented in Table 4.3. The mixture

molar composition in butanol is presented in column 2. In addition, six flames of pure butanol were established and the related information is presented in Table 4.4. The pure butanol flames (cases B1-B6) were selected such that they had the same overall equivalence ratio and total heat released with cases M1-M6 respectively, as shown in the last two columns of tables 4.3 - 4.4.

Table 4.3 Mass flow rates for the butanol-methane flame configurations at extinction

Test Case	Butanol mol fraction	C_4H_9OH	N_2 for C_4H_9OH	CH_4	N_2 for CH_4	O_2	N_2 for O_2	Overall ϕ	Qtot
	[%]	[x10^{-6}kg/s]	[x10^{-6}kg/s]	[x10^{-6}kg/s]	[x10^{-6}kg/s]	[x10^{-6}kg/s]	[x10^{-6}kg/s]		[W]
M1	10	1.12	12.16	2.21	45.87	24.42	6.79	0.5	148
M2	36	2.25	12.16	0.87	27.35	19.18	13.31	0.5	118
M3	40	3.37	12.16	1.08	38.65	27.04	13.31	0.5	165
M4	56	4.94	12.16	0.84	45.10	25.73	13.31	0.6	206
M5	58	4.49	14.89	0.69	36.11	25.73	19.84	0.6	183
M6	86	5.61	14.89	0.19	44.31	32.28	6.79	0.5	195

Table 4.4 Mass flow rates for the pure butanol flame configurations at extinction

Test Case	C_4H_9OH	N_2 for C_4H_9OH	N_2 for CH_4	O_2	$N_2$for O_2	Overall ϕ	Qtot
	[x10^{-6}kg/s]	[x10^{-6}kg/s]	[x10^{-6}kg/s]	[x10^{-6}kg/s]	[x10^{-6}kg/s]		[W]
B1	4.492	12.158	32.396	24.423	6.788	0.5	148
B2	3.594	12.158	27.003	19.184	6.788	0.5	118
B3	5.008	12.158	32.721	27.043	6.788	0.5	165
B4	6.289	12.158	42.400	25.733	6.788	0.6	206
B5	5.547	12.158	38.047	25.725	6.788	0.6	183
B6	5.907	12.158	36.521	32.355	6.788	0.5	195

Temperature measurements necessary for the calculation of strain rate at extinction were obtained at both nozzle exits just before the flame extinguished. The calculated extinction strain rates for both M1-M6 and B1-B6, are presented in Table 4.5.

Table 4.5 Extinction strain rates for butanol-methane mixtures and for pure butanol flames

Test Case	Kext [s^{-1}]	Test Case	Kext [s^{-1}]
M1	128.56	B1	108.82
M2	105.08	B2	93.70
M3	132.45	B3	113.15
M4	140.87	B4	126.10
M5	141.77	B5	183.48
M6	140.74	B6	195.37

In addition, Fig. 4.4 presents the extinction strain rate values as a function of the total combustion heat release of each flame configuration. In all six cases, pure butanol flames are more vulnerable to extinction than butanol-methane mixture flames with the same overall equivalence ratio and total combustion heat release. Furthermore, a monotonic behavior is observed with increasing heat release, which is evident both in pure butanol and in the mixture cases.

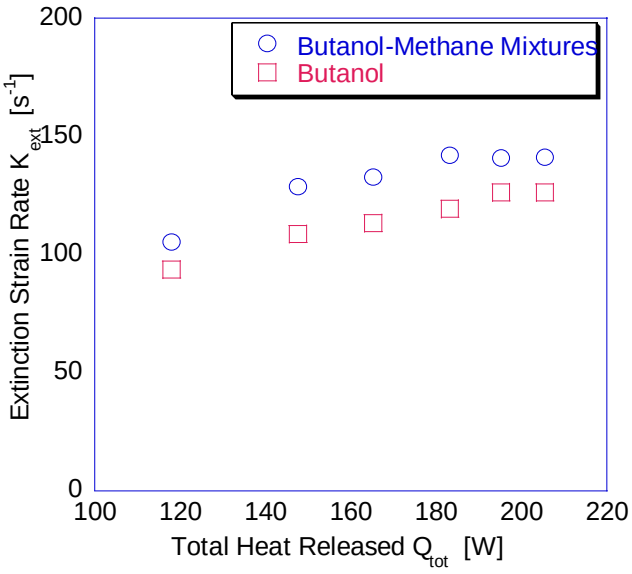

Figure 4.4 Calculations of extinction strain rate K as a function of the total heat released from combustion

4.3 Butanol Flame Structure Measurements

Butanol diffusion flames constitute a novel research area. Through this work, butanol combustion profiles are mapped and fundamental data are provided on its non-premixed combustion. Extinction strain rates as well as scalar dissipation rates were calculated, with a particular emphasis on their values at extinction. Experimental data that can guide kinetic modeling were produced. Finally, butanol diffusion flame structures were compared to widely studied methane and ethanol ones, in an effort to rationalize the potential use of butanol for power generation.

4.3.1 Obtaining species concentrations from Raman signal

The raw results of the Raman experiment correspond to arbitrary units of signal (number of counts) as a function of wavelength. This number is proportional to the photons of scattered light that are detected at that certain wavelength due to their interaction with the molecules of the species under consideration. Two plots of N_2 and O_2 for flame configuration M2 from section 4.2.2 are presented in Fig. 4.5, as characteristic examples. The location of these measurements is the exit of the fuel and oxidizer nozzles respectively for the two measured species.

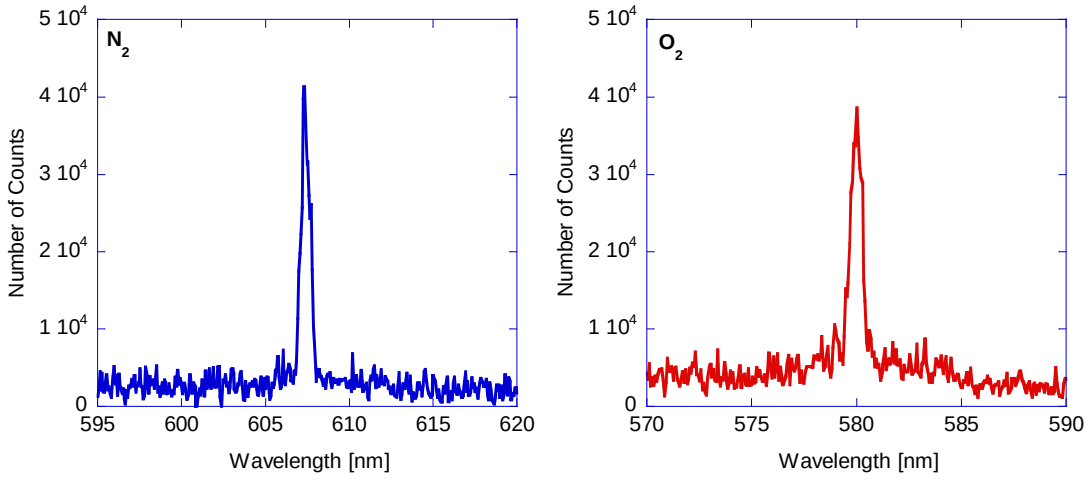

Figure 4.5 Example of raw Raman signals of N_2 and O_2 for flame configuration M2

In order to extract Raman signal intensity information out of these plots, the area under the curves was integrated. The result equals the energy of the signal E_s in eq.1.6, already presented in the introduction part. Recalling this equation, it is evident that if the number density n_i of the species at a given location is known, then the number density of the species n_s at other locations can be obtained in terms of this known value, the intensity of the Raman signals E_i, E_s and the ratio of the differential Raman cross-section at the two locations, eq. 4.9:

$$n_s = n_i \cdot \frac{E_s}{E_i} \cdot \frac{\frac{\partial \sigma}{\partial \Omega_i}}{\frac{\partial \sigma}{\partial \Omega_s}} \tag{4.9}$$

The rest of the terms of eq.1.6 are constant numbers and cancel out. As the known location for this study, the exit of the fuel nozzle was considered for N_2 and C-H bond and the exit of the oxidizer nozzle for O_2. As far as N_2 is concerned, it is noticeable

that the exit of the oxidizer nozzle could be equally considered for this calculation, since it returned the same results with an accuracy of 5%. The number density of species j at the reference locations i, is calculated in [kmol/m^3] using eq. 4.10, where the total volumetric flow rate is calculated through eq. 4.1:

$$n_{i,j} = \frac{\dot{m}_j / MW_j}{\dot{V}_{tot}} \tag{4.10}$$

In order to complete the calculations for the species concentrations of eq. 4.9, the ratio of the Raman cross-section between the two locations has to be estimated. The differential Raman cross-section is temperature dependent and for the temperature range of the current experiments its variation with temperature is plotted in Figure 4.6 for the three major species under consideration. The polynomial expressions used for this calculation are found in [82].

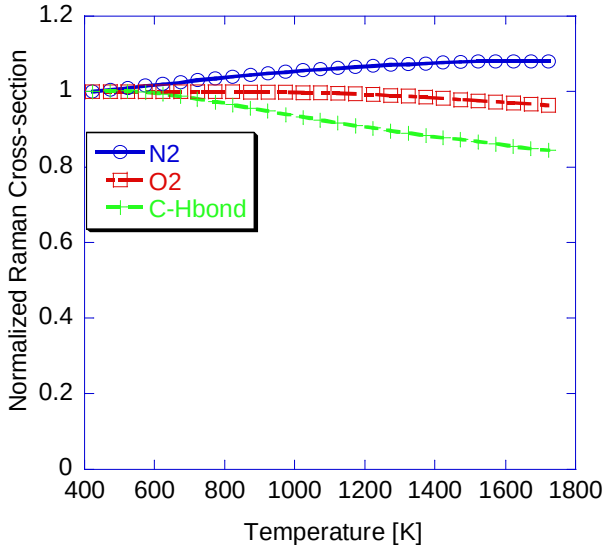

Figure 4.6 Temperature dependence of the Raman cross-section

4.3.2Species and temperature measurements in Butanol flames

4.3.2.1 Comparison of ethanol, methane and butanol-methane flames

Flame structure was probed in terms of major species profiles acquired with line-Raman imaging and temperature measurements for four flames, one for each of the fuels of section 4.2.1. Because of the long time necessary for acquisition of the Raman data, these measurements were performed only for the cases $\mathbf{A}_{but\_HR}$, $\mathbf{A}_{meth\_HR}$, $\mathbf{A}_{mixt\_HR}$ and $\mathbf{A}_{eth\_HR}$ of Table A.3 of the Appendix, which correspond to an overall equivalence ratio of 1.15. The four cases are renamed for simplicity as test cases 1 (butanol), 2 (methane), 3 (butanol-methane mixture) and 4 (ethanol) in Table 4.6. This table presents the mass flow rates of the streams involved. Notably, in tables 4.6 and A.3 the flow rates of fuel and oxidizer are equal, since extinction was achieved by increasing the amount of diluent in the flame. In Table 4.7, the values of ρ_i, U_i, and K for cases 1-4 are presented. It is reminded that all cases release the same amount of heat which is equal to 208W.

Table 4.6 Mass flow rates for the four flame configurations

Test Case	Alcohol	N_2 in alcohol stream	CH_4	N_2 in CH_4 stream	O_2	N_2 in O_2 stream
	[x10^{-6}kg/s]	[x10^{-6}kg/s]	[x10^{-6}kg/s]	[x10^{-6}kg/s]	[x10^{-6}kg/s]	[x10^{-6}kg/s]
1. Butanol	6.29	9.41	0.00	22.35	14.19	15.92
2. Methane	0.00	0.00	4.15	29.07	14.41	19.84
3. Butanol - Methane Mixture	3.37	9.41	1.93	20.12	14.30	19.84
4. Ethanol	7.19	9.41	0.00	20.12	8.71	13.31

Table 4.7 Densities and speeds at the oxidizer and fuel nozzles and strain rates for the four flame configurations

Test Case	Oxidizer Density ρ_{ox}	Fuel Density ρ_{fuel}	Oxidizer Speed u_{ox}	Fuel Speed u_{fuel}	K
	[kg/m^3]	[kg/m^3]	[cm/sec]	[cm/sec]	[sec^{-1}]
1	0.39	0.86	63.00	36.12	155.5
2	0.40	0.74	70.36	36.43	160.3
3	0.48	0.78	58.48	36.40	140.1
4	0.53	0.83	34.09	36.11	105.9

Major species concentration measurements in kmol/m^3 for C-H bond, O_2, and N_2, as a function of the distance from the fuel nozzle exit in mm are shown in Figure 4.7. Each of the figure panels corresponds to a different fuel. The measured temperature distribution is also presented. It is noted, that the fuel concentrations are multiplied by a factor of 5 to achieve clearer illustration of the results. In all test cases, fuel concentration has its maximum at the location closest to the fuel nozzle and starts depleting as it approaches the flame zone. Similarly, oxidizer is maximum at the oxidizer nozzle and its destruction begins as it advances towards the flame.

The error of the Raman measurements deserves some discussion. The image intensifier is a noisy device, hence producing significant error, which translates to lower S/N ratios for weaker signals, i.e. in the flame region. The maximum error is observed in the flame region, where the S/N ratio for N_2 is around 4. The minimum is observed at the nozzles, where for N_2, O_2 and C-H bond the S/N ratios are to the order of 10. A

detailed analysis on the uncertainties associated to the Raman signal is performed in section 4.4.3.

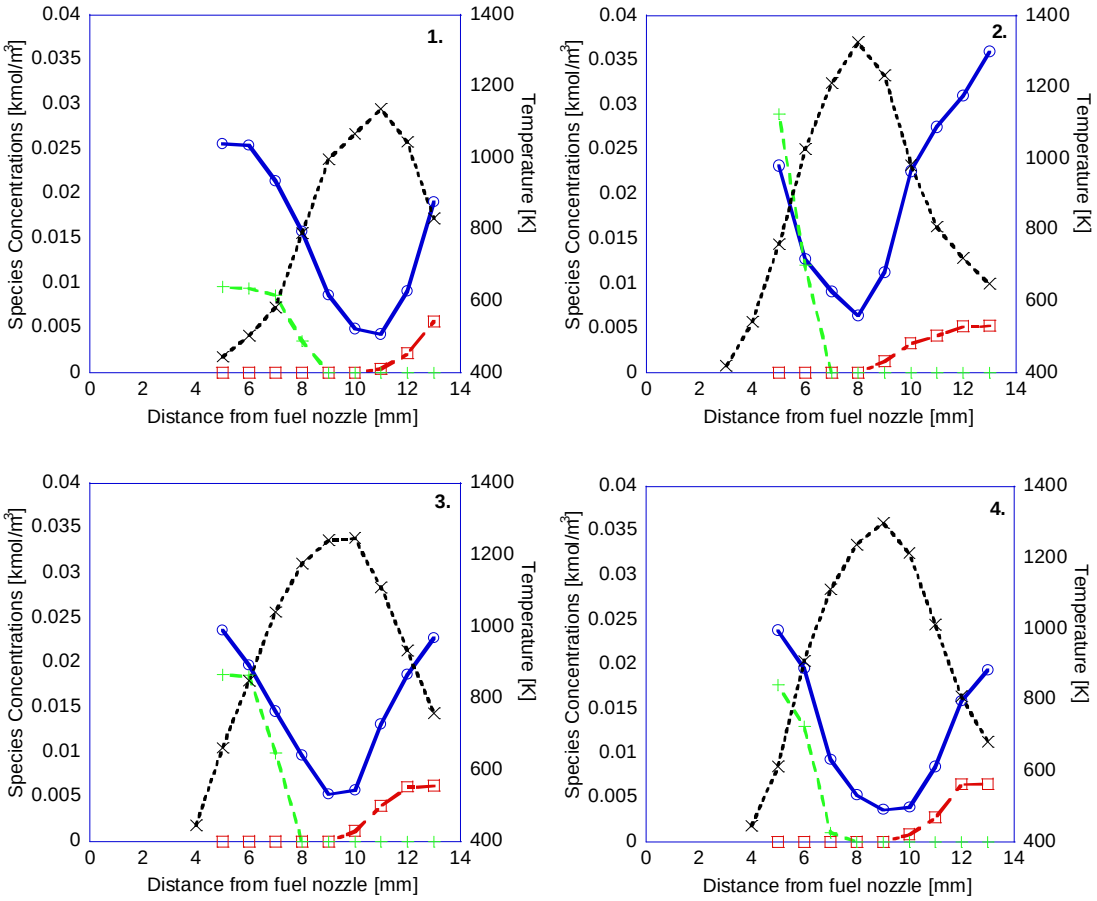

Figure 4.7 Species concentration measurements for N_2 (o), O_2 (□) and C-H bond (+) and Temperature distribution curves (x) for test cases 1, 2, 3 and 4

In all the flames under consideration, there was no leakage of C-H containing species into the oxidizer stream. Fuel consumption was initiated through pyrolysis at intermediate temperatures and it is interesting to note that there are practically no C-H bonds left in the zone of the flame where the temperature is maximum. This is in

agreement with widely supported suggestions that CO oxidation is the main cause of exothermicity in flames of carbon-containing fuels. Taking into consideration that the equivalence ratio as well as the overall heat release is constant for all test cases, it is noted that in cases of reduced strain (cases 1,4) the region in which both the parent fuel and the oxidizer have been drastically depleted is thicker compared to the cases of increased strain rate (cases 2, 3).

There is significant physical importance in the nitrogen signal also reported in Fig. 4.8. The flames are highly diluted (N_2 > 80% of the mixture on a molar basis) and as a result N_2 concentration can be seen as a measure of the total mixture density. For an ideal gas this concentration scales as 1/T and the resulting closely hyperbolic relation of nitrogen concentration with temperature across the flame can be seen in Fig. 4.8.

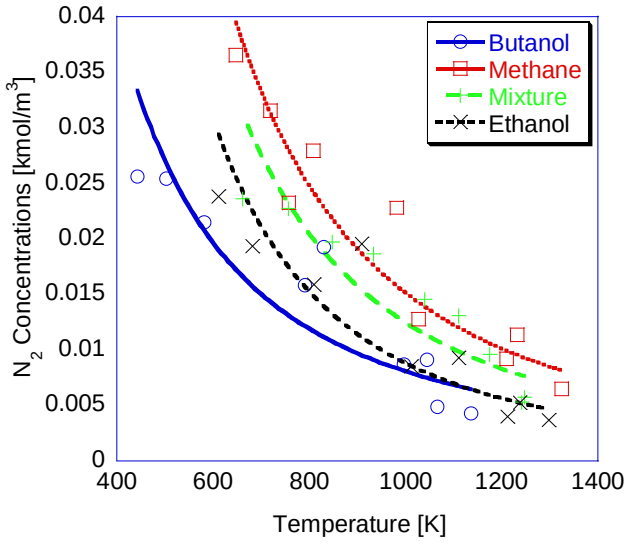

Figure 4.8 Nitrogen concentrations as a function of temperature for the four flame configurations

Regression coefficients R^2 vary between 0.82-0.91 for the various fuels. It is noted that for every given nitrogen concentration the methane flame is the one with the highest temperature followed by the other fuels ranked in descending order of molecular weight (perhaps counter-intuitively: *not* heating value). It is also noted that the average molecular weight of the fuel stream (including the diluent) ranks similarly to the one of the parent fuels and is equal to 25.6, 28.5, 30.3 and 31.2 kg/kmol for methane, methane-butanol mixture, ethanol and butanol respectively. An important feature of butanol flames is that for the same heat release and overall stoichiometry they generate lower temperatures in the flame region.

4.3.2.2 The effect of strain on pure butanol flames

The structure of butanol flames is affected by imposed strain. In Fig. 4.9, two pure butanol flames are compared that have the same equivalence ratio ϕ=1.15 and overall heat release 208W. The strain on the two flames differs from 155.5 s^{-1} in the already presented case 1 of section 4.3.2.1, to 129.22 s^{-1} in a new case 1′ established for this comparison.

Much as it is theoretically right that non-premixed flames do not have an inherent flame thickness as the premixed ones do, it is clear that a mixing layer thickness can be defined from the Raman-Temperature data of Fig. 4.7, by curve-fitting a Gaussian distribution to the temperature profile [81] and considering the characteristic thickness to be equal to the full width at half maximum (FWHM), which for a Gaussian correlates

with the standard deviation as $FWHM = 2 \cdot \sqrt{2 \cdot \ln 2} \cdot \sigma \approx 2.35482 \cdot \sigma$. As shown in Fig. 4.9, an increase in strain rate compresses the mixing layer, which is calculated to be 5.45 mm and 7.37 mm for cases 1 and 1′ respectively.

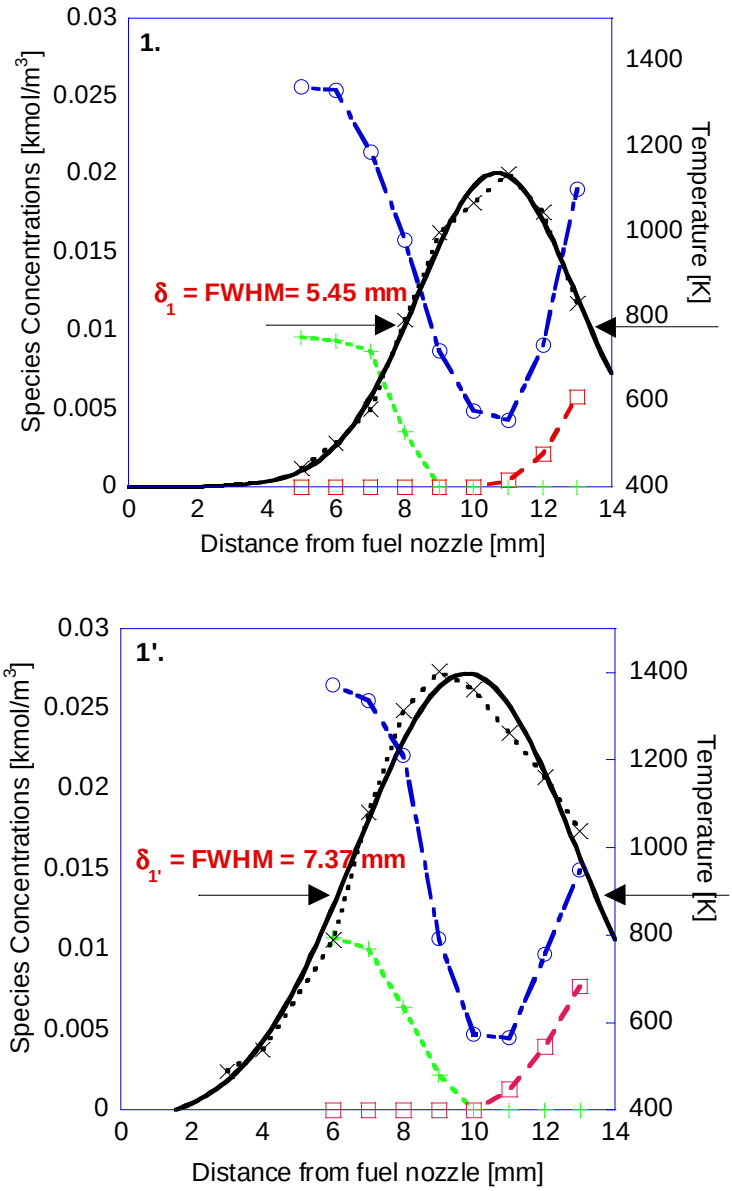

Figure 4.9 Mixing layer thicknesses δ_1 and $\delta_{1'}$ for butanol flame cases 1 and 1′ respectively and species concentration measurements for N_2 (o), O_2 (□) and C-H bond (+). Temperature distribution curves (x) are curve-fitted with Gaussian distributions (solid lines)

In addition, it is noticeable that the shrinking of the mixing layer due to increasing strain is accompanied by a significant drop in temperature, ~280 K. Theoretical suggestions [41, 79] indicate a $1/K^{0.5}$ dependence of the mixing layer thickness on imposed strain. The two points of Fig.4.9 are consistent with a $1/K^{1.63}$ behavior, which is a much sharper decline. The main structural feature that is established is an abrupt decrease in mixing layer thickness before the flame reaches the extinction strain rate of Figs. 4.1 and 4.2.

4.3.2.3 Methane-assisted butanol flames

Flame structure measurements of species concentration and temperature were obtained for the six butanol-methane mixture cases of section 4.2.2, cases M1-M6. The mass flow rates of the involved streams are shown in Table 4.8, which differs from table 4.4 in the mass flow rate of the diluents. The overall equivalence ratios and total heat release from combustion are in accordance to Table 4.4. In Table 4.9, the values of ρ_i, U_i, and K for cases the six mixture cases under consideration are presented.

Table 4.8 Mass flow rates for the six flame configurations

Test Case	$C_4H_{10}O$	N_2 for $C_4H_{10}O$	CH_4	N_2 for CH_4	O_2	$N_2$for O_2
	[x10^{-6}kg/s]	[x10^{-6}kg/s]	[x10^{-6}kg/s]	[x10^{-6}kg/s]	[x10^{-6}kg/s]	[x10^{-6}kg/s]
M1	1.123	18.682	2.210	19.363	24.423	6.460
M2	2.246	11.608	0.874	18.214	19.184	12.818
M3	3.369	9.410	1.076	20.121	27.043	12.818
M4	4.941	9.410	0.842	18.214	25.733	12.818
M5	4.492	17.601	0.692	16.657	25.733	17.904
M6	5.615	17.601	0.190	18.982	32.282	6.460

Table 4.9 Densities and speeds at the oxidizer and fuel nozzles and strain rates for the six flame configurations

Test Case	Oxidizer Density ϱ_{ox}	Fuel Density ϱ_{fuel}	Oxidizer Speed u_{ox}	Fuel Speed u_{fuel}	K
	[kg/m^3]	[kg/m^3]	[cm/sec]	[cm/sec]	[sec^{-1}]
M1	0.379	0.744	66.32	45.29	173.02
M2	0.388	0.797	67.16	33.68	153.88
M3	0.404	0.792	80.40	34.97	172.48
M4	0.373	0.802	84.21	33.94	178.63
M5	0.496	0.817	71.72	39.32	162.93
M6	0.480	0.844	65.80	40.93	160.12

Raman spectroscopy measurements of major species concentration, in kmol/m^3 for C-H bond, O_2, and N_2, as a function of the distance from the fuel nozzle exit in mm are presented in Figure 4.10. Each figure corresponds to a different flame configuration from Table 4.8. The measured temperature distribution is also presented on a separate y-axis. In these cases, the fuel concentrations are multiplied by a factor of 10 to achieve clearer illustration of the results. As observed in the panels of Figure 4.7 as well, the fuel and oxidizer concentrations have their maximum at the location closest to the fuel and oxidizer nozzles respectively and their destruction begins as they advance towards the flame. Nitrogen signal is again observed to be highly affected by the high temperatures, as it drops-off in the flame region of all configurations.

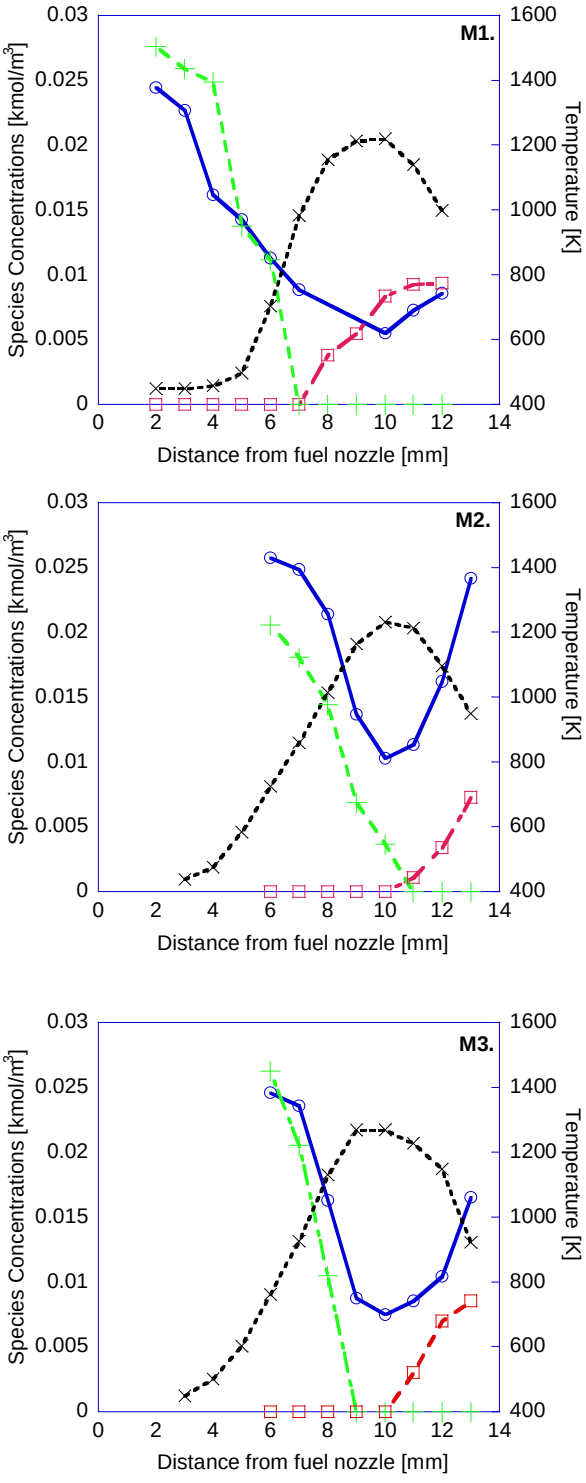

Figure 4.10 (cont. on next page)

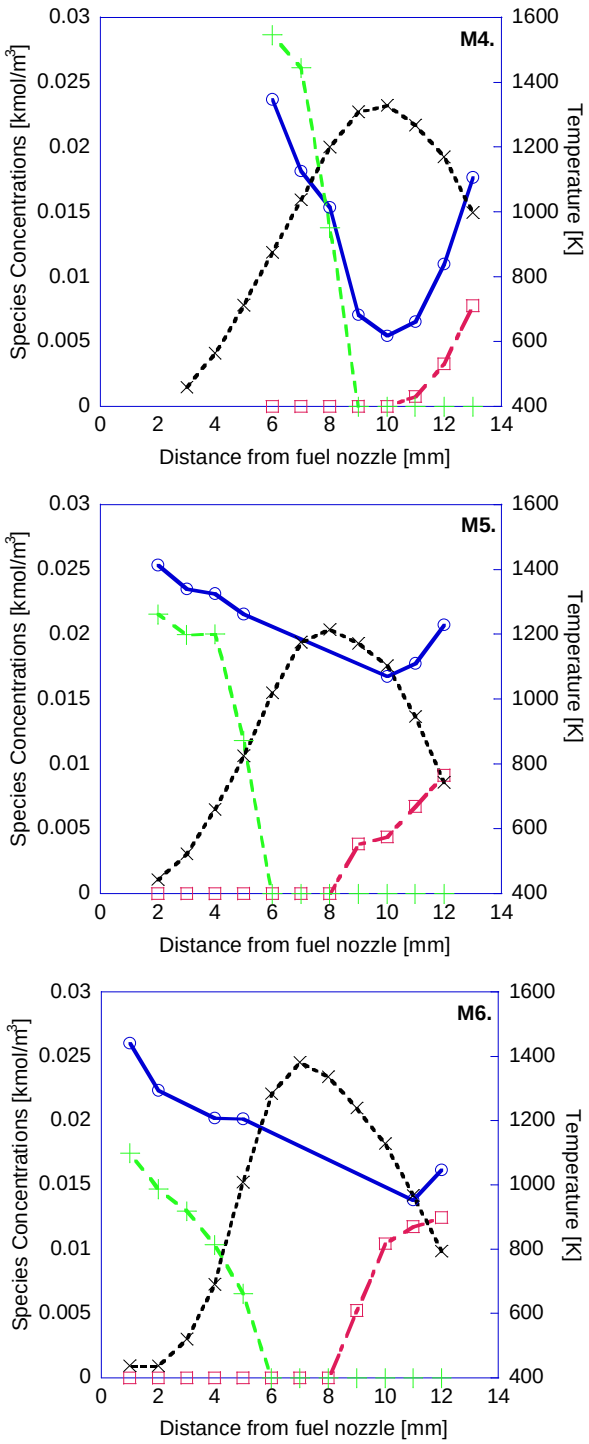

Figure 4.10 Species concentration measurements for N_2 (o), O_2 (□) and C-H bond (+) and temperature distribution curves (x) for test cases M1-M6 of table 4.8

In cases with lower strain rates (M5, M6), it is observed that oxidizer and fuel have vanished before the two profiles intersect. Fuel consumption has been initiated through pyrolysis, since the temperature is elevated and this is followed by combustion of the intermediate products with oxygen. In these cases, the flame-sheet region is broader and this is accompanied with broader temperature distribution curves, as well. As the strain rate increases, the reactant concentrations are brought closer (cases M3,M4) or even vanish at the same location (case M1). This happens because with increasing strain, the residence time in the mixing layer is reduced, resulting to a thinner flame region. However, even though case M2 has the lowest strain rate, the above observations do not hold.

An overlap of the reactant lines is observed indicating a fuel leakage in the oxidizer region. This phenomenon is observed in flames close to extinction and flame M2 has the lowest heat release and the lowest peak temperature indicating a potential approach to extinction conditions. Comparing cases with the same overall equivalence ratio (M1, M2, M3 and M6), the combustion behavior of the species follows the pattern of steeper gradients with increasing strain rate (except for case M2). Temperature distributions have their maximum value approximately at the center of the gap between the nozzles and this maximum increases with higher fuel energy release. The error in these measurements is on the order of 10% and is related to the slight instabilities of the flame-sheet as established in the lab, as well as to the scatter in the seven measurements

of temperature that corresponded to each data point. This error will be discussed in detail in section 4.4.3.

It is noted that the flames are highly diluted (N_2 > 80% of the mixture) and as a result N_2 concentration can be seen as a measure of the total mixture density similar to the flames presented in section 4.3.2.1. The hyperbolic relation of nitrogen concentration with temperature across the flame can be seen in Fig. 4.11. Regression coefficients R^2 vary between 0.76-0.89 for the various mixtures. These data can be compared with the corresponding data for flames of pure fuels shown in Fig. 4.8.

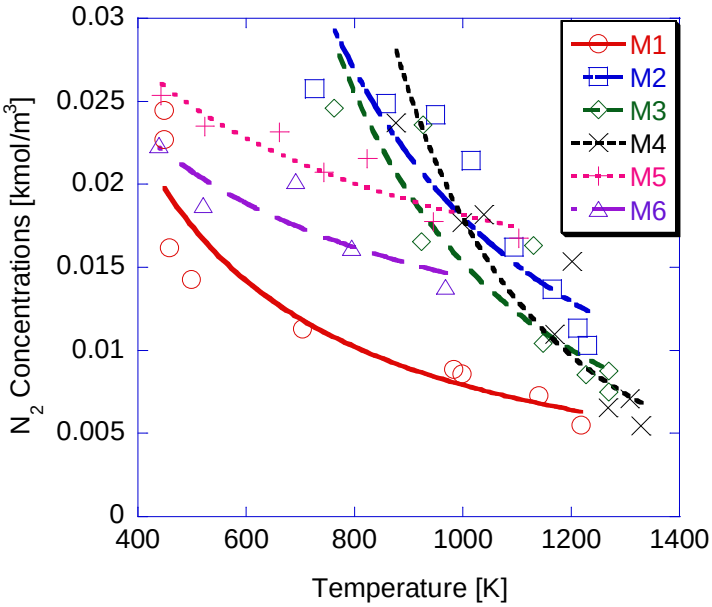

Figure 4.11 Nitrogen concentrations as a function of temperature for the six flame configurations

4.4 Estimation of the Scalar Dissipation Rate at the Stoichiometric Surface

A final goal of this chapter will be the approximation of the scalar dissipation rate, the importance of which was explicitly presented in section 1.2.2. Equations (1.3) and (1.4) reveal the possibility of estimating the scalar dissipation rate at the stoichiometric surface χ_{stoich} either through the gradient of the mixture fraction at the same location $\left|\nabla Z\right|_{stoich.}$, or through the mixing layer thickness δ. In this section, both approaches are employed to the butanol-methane mixtures (M1-M6) of section 4.3.2.3.

4.4.1 First approach: The mixing layer thickness estimated through the temperature distribution

Similarly to section 4.3.2.2, the experimentally obtained temperature values were curve-fitted with a Gaussian distribution and the thickness was then approximated as the "full width at half maximum" (FWHM) of the curve. The calculated flame thicknesses δ are tabulated in Table 4.10.

Table 4.10 Calculated mixing layer thickness δ as FWHM

Test Case	M1	M2	M3	M4	M5	M6
δ [mm]	6.078	7.228	7.090	8.459	7.233	7.019

The inverse square root dependence of δ on strain rate that is implied by eq. (1.3) is investigated in Fig. 4.12. The experimental findings are plotted on a log-log scale alongside with a curve depicting the theoretically expected behavior. Since only the slopes of the respective curves are significant for purposes of comparison, the theoretical curve is plotted such that the initial points of both curves coincide.

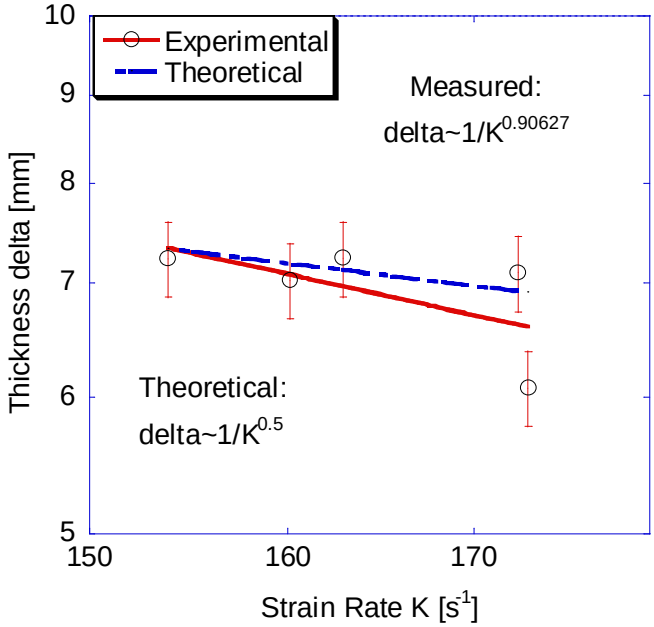

Figure 4.12 Mixing layer thickness δ estimated through the temperature distribution vs. strain rate on a log-log scale for flame configurations M1-M6. The experimentally measured slope (solid line acquired through least square fit) is compared with the theoretically expected $1/K^{0.5}$ behavior (dashed line) which is positioned such that the initial points of both lines coincide

The results of Fig. 4.12 show that there is a difference between the theoretically expected $1/K^{0.5}$ and the actually measured dependence of δ on strain rate which scales as $1/K^{0.90627}$. The exponent is far from the expected value and the regression constant is very poor R=0.61956. A detailed discussion on the calculation of the error bars shown in

Fig.4.12 takes place in section 4.4.3. Their magnitude in on the order of 5% of the estimated mixing layer thickness value. The observed departure of the mixing layer thickness from the theoretically expected trend constitutes the calculation of the scalar dissipation rate from the temperature distribution inappropriate for this study. For that reason, the scalar dissipation rate at the stoichiometric surface was approximated using the mixture fraction gradient $\left|\nabla Z\right|_{stoich.}$.

4.4.2 Second approach: The mixing layer thickness estimated through the mixture fraction gradient at the stoichiometric surface

The definition of the mixture fraction is based on the mass fraction of major species and can be formulated in several ways, which were evaluated in [43]. A definition based on the mass fraction of N_2 can be followed, where:

$$Z = \frac{Y_{N_2} - Y_{N_2Ox}}{Y_{N_2Fuel} - Y_{N_2Ox}} \tag{4.11}$$

In this last equation, Y denotes mass fraction, N_2 subscript stands for nitrogen and F, Ox for the fuel and oxidizer stream respectively. Y_{N2} can be used as a conserved scalar since N_2 is non-reactive. However, in this study, due to the lack of information regarding the combustion products, Y_{N2} was approximated through:

$$Y_{N_2} = \frac{C_{N_2}.MW_{N_2}}{C_{N_2}.MW_{N_2} + C_i \cdot MW_i} \tag{4.12}$$

In this equation, C_{N2} and MW_{N2} are the measured concentration and the molecular weight of nitrogen. Subscript i denotes either the fuel or oxidizer side outside

the flame region and C_i and W_i are the measured concentrations and molecular weights of either fuel or oxygen. Hence, the gap between the nozzles was assumed to consist of three regions: The flame-sheet region, located in the vicinity of the maximum temperature, and the fuel and oxidizer regions where no combustion products were present.

This technique was applied in flame configurations M2, M3 and M4 of Fig 4.10, which have measured values of N_2 concentration in the flame region as well. After calculating the mixture fraction Z in all locations, an error function was curve-fitted to the Z distribution, since this is the functional form expected from the theoretical analyses of [40, 43]. The curve fit function is of the form:

$$Z = A * erfc(\frac{\mathbf{x} - B}{C}) \qquad (4.13)$$

where A, B and C are regression constants and x is the distance from the fuel nozzle.

The stoichiometric surface was considered to be at the location of the maximum slope of the Z distribution and the corresponding plot for flame configuration M3 is shown in Fig. 4.13. The calculated $\left|\nabla Z\right|_{stoich.}$ for each flame case was then used in order to determine the mixing layer thickness δ, which was estimated by using a precise equality in Eq. 1.4 (of intro). δ for flame case M3 is also shown in Fig.4.13. Since the objective here was to verify the inverse-square-root dependence of δ on the imposed strain, only a relative measurement was required. So, using a precise equality instead of

proportionality in Eq. 1.4 does not alter the substance of our results. Table 4.11 contains the values of δ for all three flame cases.

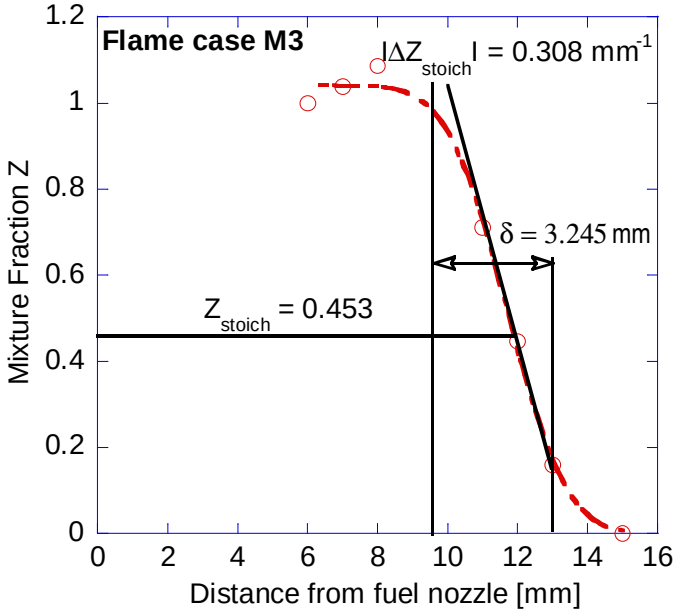

Figure 4.13 Mixture fraction distribution and curve-fitted error function for flame configuration M3

Table 4.11 Calculated mixing layer thickness δ through $|\nabla Z|_{stoich.}$

Test Case	M2	M3	M4
δ [mm]	2.847	3.245	2.483

Here, the investigation of the inverse square root dependence of δ on strain rate, similarly to Fig. 4.12, showed that there is good agreement between the theoretically expected $1/K^{0.5}$ and the actually measured dependence of δ on strain rate which scales as $1/K^{0.42394}$. In all three cases, the stoichiometric surface was found to be located approximately 2mm away from the location of maximum temperature in the oxidizer

side. Specifically, it was 13.2 mm for cases M2 and M4 and 12 mm for case M3. This can be attributed to the significant experimental error rising from the Raman measurements. A more sensitive camera that would capture combustion products is necessary for a more accurate measurement of the mixture fraction.

4.4.3 Uncertainty analysis on the calculation of the mixing layer thickness δ

4.4.3.1 Uncertainty in the direct measurement of temperature and in the resulting δ-calculation

The overall uncertainty U in the measurement of temperature, both due to random and systematic errors, is to be investigated in this section. It is reminded, that the measurements were performed using K-type thermocouples and that each temperature-measurement point was an average of 7 thermocouple readings.

According to ANSI/ASME and AIAA Standards [83, 84] a systematic uncertainty, B, has to be defined and associated with the instrumentation of the particular experiment. B is defined as full width at 5% of the maximum of a Gaussian envelope that describes the systematic error [85]. For a given instrument, the systematic error is a fixed number and for the K-type thermocouples, the systematic uncertainty B is 2.2^{o}C or 0.75% of the measured temperature value (whichever of the two is larger) [86], for

temperatures above 0°C. The standard deviation estimate S_B of the distribution of the systematic error equals half the value of the systematic uncertainty: $B = 2 \cdot S_B$.

Except for the uncertainty associated with the probe specifications, a second source of systematic error makes this analysis more complex. The source of this secondary error is the systematic error in the measurement of the thermocouple location. This uncertainty is considered negligible here because of the use of accurate translational stages.

The standard deviation estimate S of the random uncertainty, can be defined using eq. 4.14, for a sample of N readings (N = 7 for this investigation).

$$S = [\frac{1}{N-1} \sum_{i=1}^{N} (X_i - \overline{X})^2]^{1/2} \qquad (4.14)$$

In the last equation, X_i corresponds to the individual reading i and $\overline{X}$ is the mean of the sample population:

$$\overline{X} = \frac{1}{N} \sum_{i=1}^{N} X_i \qquad (4.15)$$

For every temperature point j (resulting from N=7 individual readings i), the combined standard uncertainty u_c was estimated according to ISO Guide [87]:

$$u_c{}^2 = S_{B_j}{}^2 + S_j{}^2 \qquad (4.16)$$

A level of confidence has to be associated with the uncertainty of the temperature variable, hence a coverage factor $t_{\%}$ has to be introduced such that [87]:

$$U_{\%} = t_{\%} u_c \qquad (4.17)$$

In the last equation $U_{\%}$ is the expanded or *overall* uncertainty at a given percent confidence and t is the value from the t-distribution. The confidence level was selected to be 95%, for consistency with the systematic uncertainty. In order to select the $t_{0.95}$ value from the corresponding table for the t-distribution, a number of degrees of freedom was needed. The effective number of degrees of freedom is approximated by the Welch-Satterthwaite formula [87]:

$$\nu_j = \frac{\left(S_j{}^2 + S_{B_j}{}^2\right)^2}{S_j{}^4 \Big/ \nu_{S_j} + S_{B_j}{}^4 \Big/ \nu_{B_j}} \tag{4.18}$$

Where ν_{S_j} and ν_{B_j} are the numbers of degrees of freedom associated with S_j and S_{Bj} respectively:

$$\nu_{S_j} = N - 1 \tag{4.19}$$

$$\nu_{B_i} \approx \frac{1}{2}\left(\frac{\Delta B_j}{B_j}\right)^{-2} \tag{4.20}$$

The last equation represents a recommended estimate for ν_{B_j} by ISO Guide [87]. The term in the parenthesis corresponds to the relative uncertainty of B_j, which for a K-type thermocouple was 0.1%.

Table 4.12 contains the measured values of temperature and the overall corresponding uncertainties for flame case M3 of section 4.3.2.3. The intermediate variables contributing to the calculation of U and were discussed in this section, are tabulated and presented as well. The overall uncertainty of the temperature presented in

Table 4.12 is associated solely with the measurement of temperature (it is developed in the y-direction) and not with the dependence of the measured variable on space. As shown in the very first column of Table 4.12, there is a spatial direction on which temperature measurements are obtained, thus there is an underlying error in the x-direction.

Table 4.12 Random, systematic and overall uncertainties for the measured temperatures of flame configuration M3 of section 4.3.2.3

Distance from fuel nozzle	Temperature	S_j	S_{Bj}	u_c	ν_j	$t_{0.95}$	$U_{0.95}$	Overall relative uncertainty
[mm]	[K]	[K]	[K]	[K]			[K]	[%]
3	448	4.03	2.20	4.59	10	2.23	10.23	2.28
4	501	6.01	2.20	6.40	8	2.31	14.76	2.95
5	603	15.69	2.26	15.85	6	2.45	38.79	6.43
6	762	27.34	2.86	27.49	6	2.45	67.27	8.83
7	926	32.67	3.47	32.85	6	2.45	80.39	8.68
8	1131	45.48	4.24	45.68	6	2.45	111.77	9.88
9	1269	48.63	4.76	48.86	6	2.45	119.57	9.42
10	1270	50.32	4.76	50.54	6	2.45	123.68	9.74
11	1228	46.34	4.61	46.57	6	2.45	113.95	9.28
12	1148	43.99	4.31	44.20	6	2.45	108.16	9.42
13	923	31.69	3.46	31.88	6	2.45	78.01	8.45

This error emerges from the degree of accuracy on the shifts of the translational stage, where the burner is mounted and it was taken as constant. The corresponding relative uncertainty was considered to be 5% of the increment the translational stage was moving (always equal to 1mm). Fig.4.14 shows the measured temperature values along with their associated uncertainties, both in x and y direction, for flame configuration M3.

It can be seen that the x-direction uncertainties are negligible. A similar analysis in the temperature distributions of the remaining flame configurations reveals the approximate 10% uncertainty discussed in section 4.3.2.3, which corresponds to the hot regions around and in the flame.

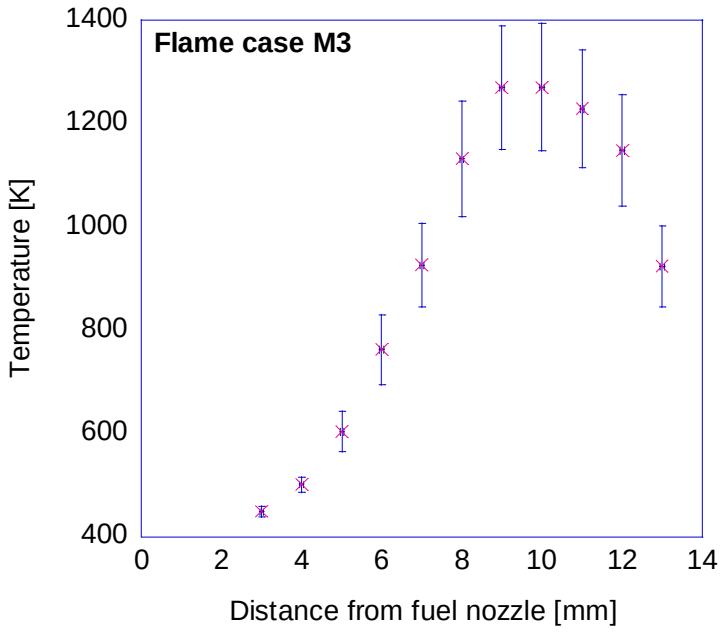

Figure 4.14 Measured temperature values along with their associated uncertainties, both in x and y direction, for flame configuration M3

The estimated uncertainties associated with the direct measurements of temperature propagate through data reduction. In order to estimate the uncertainty of the mixing layer thickness δ, general uncertainty analysis was followed; that is, only overall uncertainties were considered and not the details of systematic or random

components. According to general uncertainty analysis [83], the overall uncertainty U_y of the variable Y=Y(X_1,X_2,…X_i) is:

$$U_y{}^2 = \left(\frac{\partial Y}{\partial X_1}\right)^2 \cdot U_{X_1}^2 + \left(\frac{\partial Y}{\partial X_2}\right)^2 \cdot U_{X_2}^2 + \ldots + \left(\frac{\partial Y}{\partial X_i}\right)^2 \cdot U_{X_i}^2 \qquad (4.21)$$

During the first approach (section 4.4.1), the mixing layer thickness δ was approximated as a *full width at half maximum* of the Gaussian distribution that resulted after curve-fitting the experimental temperature data.

$$\delta = 2 \cdot \sqrt{2 \ln 2} \cdot \sigma \qquad (4.22)$$

For flame case M3, the expression of the Gaussian distribution was defined using Kaleidegraph 3.5 with a regression coefficient $R^2 = 0.99649$, as:

$$T = 378.09 + 918.29 \cdot \exp\left(-\frac{(x - 9.9912)^2}{2 \cdot 3.0109^2}\right) \qquad (4.23)$$

The uncertainties associated with the constants of equation 4.23 are:

$m_1 = 378.09 \pm 30.876$ K and $m_2 = 918.29 \pm 28.978$ K, where the other two constants correspond to the mean μ and the standard deviation σ of the Gaussian:

$$\mu = 9.9912 \pm 0.05523 \text{ mm} \qquad (4.24)$$

$$\sigma = 3.0109 \pm 0.12584 \text{ mm} \qquad (4.25)$$

From equations 4.21, 4.22 and 4.24, the value and the corresponding uncertainty of the mixing layer thickness δ are estimated:

$$\delta = 7.0901 \pm 0.29633 \text{ mm} \qquad (4.26)$$

For this flame configuration, the relative uncertainty of δ is on the order of 4.2% and similarly is estimated for the other test cases, resulting in the error bars of Fig. 4.12.

4.4.3.2 Uncertainty in the direct measurement of species and in the resulting δ-calculation

It is reminded here that the image intensifier is a noisy device, hence producing significant error, which translates to lower S/N ratios for weaker signals, i.e. in the flame region. The maximum error is observed in the flame region, where the S/N ratio for N_2 is around 4. The minimum error is observed at the nozzles, where for N_2, O_2 and C-H bond the S/N ratios are on the order of 10. S/N ratios are considered to represent the total uncertainty rising from the measurements of concentration, since their random and systematic components could not be further distinguished.

For flame case M3, the expression of the error function that was curve-fitted over the mixture fraction data was defined using Kaleidegraph 3.5, with a regression coefficient $R^2 = 0.99581$, as:

$$Z = 0.52104 \cdot erfc\left(\frac{(x - 11.689)}{1.899}\right) \tag{4.27}$$

The uncertainties associated with the constants of equation 4.27 are:

$m_1 = 0.52104 \pm 0.010265$, $m_2 = 11.689 \pm 0.0883$ mm and $m_3 = 1.899 \pm 0.2087$ mm

4.4.4Scalar dissipation rate approximation through the mixture fraction approach

In order to approximate the scalar dissipation rate at the stoichiometric surface χ_{stoich}, equations 1.3 and 1.4 were combined:

$$\chi_{stoich} = 2D(\nabla Z)^2_{stoich} = 2D/\delta^2 \quad (4.28)$$

The mixing layer thickness δ was used as calculated through the mixture fracture gradient in section 4.4.2, since this approach was proven to be more accurate when compared to a calculation of δ based on the temperature distribution. The diffusion coefficient D of eq. 4.28 corresponds to the diffusivity of the conserved scalar, however its value is not easy to define. The flames under investigation are considered to have a Lewis number Le≈1, hence equal diffusivities are considered for fuel and oxidizer. In addition, they are strongly diluted in N_2 which constitutes the medium within which mass transport occurs. As a result, the diffusivity that should ideally be used in eq. 4.28 would be that of either fuel or oxidizer in N_2 at an elevated temperature close to flame conditions. In practice though, this is a complex calculation since various species are present at the flame.

For a temperature of ~650K, which was the highest temperature for which data are available in [63], three relevant diffusion coefficients are given in [63]. In a binary mixture of N_2-O_2, D=0.849 cm^2/s and of CH_4-N_2 D=0.890 cm^2/s. If methane is considered in excess air, D=0.899cm^2/s. It can be seen that D varies slightly with the species involved

and as a result the average of the above three values was used for the calculation of χ_{stoich}. Table 4.13 contains these calculated values of χstoich for flame configurations M2, M3 and M4 as well as the corresponding strain rate values also presented in Table 4.9. The results are plotted in Figure 4.15.

Table 4.13 The calculated values of χ_{stoich} and the corresponding strain rates K for flame configurations M2, M3 and M4

Flame configuration	χ_{stoich}	K
	[s^{-1}]	[s^{-1}]
M2	216.97	153.88
M3	167.01	172.48
M4	285.26	178.63

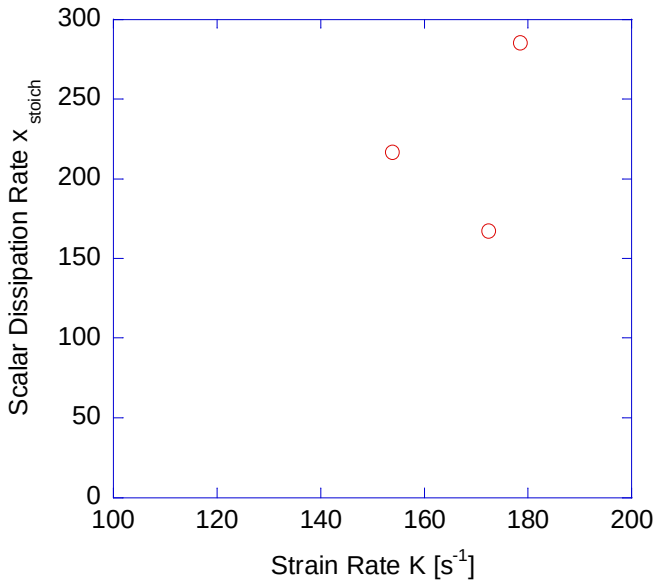

Figure 4.15 Scalar dissipation rate at the stoichiometric surface as a function of strain rate for flame configurations M2, M3 and M4

In the Figure, the proportionality expected from eq. 1.3 between χ_{stoich} and K is not validated and in particular, the relation is not even monotonic. This can be attributed both to the significant errors associated with the Raman measurements, as well as to the fact that three measuring points can hardly establish or validate a trend quantitatively.

4.5 Summary

Butanol non-premixed flames can sustain higher strain rates at extinction than the corresponding flames of ethanol, which is currently used as a bio-fuel. The related increase in extinction strain rate is on the order of 10-20% depending on overall stoichiometry as well as whether the comparison is done on a constant-heat-release or a constant-fuel-mass-flow-rate basis. In comparison to the non-oxygenated methane fuel, the extinction strain rate of butanol flames is almost 40% lower. It is noted that butanol/methane mixtures exhibited extinction strain rates that were lower than weighted averages of the extinction strain rates for the pure components if these weighted averages were calculated using either mass or mol fractions.

No leakage of C-H-bond-containing fuels was measured for any of the compared fuels. This generated a zone where the two reactants did not coexist. For the same heat release, these zones were thicker for flames of oxygenated fuels (butanol and ethanol) rather than of methane, because of the smaller strain on the flames. For strongly diluted flames, an almost linear relation was established between temperature and nitrogen concentration. For constant heat release and the same nitrogen concentration, butanol

exhibited approximately 10% smaller temperature, because of the higher average molecular weight of the required streams.

Pure butanol flames were found to be more vulnerable to extinction than butanol-methane mixture flames with the same overall equivalence ratio and total combustion heat release. Furthermore, a monotonic behavior of the extinction strain rate was observed with increasing heat release, both in pure butanol and in the mixture cases.

The inverse square root dependence of the mixing layer thickness δ on strain and scalar dissipation rate was investigated for the butanol-methane mixture cases and δ was estimated using the temperature distribution across the flame. This was found to generate a departure of δ from the theoretically expected square-root behavior. For that reason, the scalar dissipation rate at the stoichiometric surface was approximated through the mixture fraction gradient $|\nabla Z|_{stoich.}$ for three of the previously used flame cases. The results did show a closer agreement with theoretical predictions.

CHAPTER 5

BUTANOL KINETIC MODELING

In this section, calculations are presented of butanol kinetics in the zero-dimensional piston-cylinder assembly described in Chapter 2. In particular, two combustion simulations were performed, both of them in air: First, stoichiometric combustion of butanol was considered and second, combustion of a lean mixture was investigated, with an equivalence ratio ϕ=0.7, for the same amount of fuel. It is reminded here that in the simulation ignition is achieved through autoingition, without an external ignition source and that the compression ratio is 20:1.

The analysis was extended to include comparisons with ethanol and n-heptane. The amount of each one of the two fuels was selected such that they would release approximately the same amount of heat (in J) to 1 mol of butanol, burnt at 0.8 bar, 350 K and in a volume of 400 cm^3. The corresponding values of heat release were around 925 J and 650 J for the stoichiometric and lean case respectively, based on the lower heating values [63] of the fuels. Table 5.1 contains the reactant mole fractions used [in %], for both equivalence ratios. The oxygen and nitrogen amounts were calculated based on the global combustion reactions:

$$C_4H_9OH + 6(O_2 + 3.76N_2) \rightarrow 4CO_2 + 5H_2O + 22.32N_2 \quad (5.1)$$

$$C_2H_5OH + 3(O_2 + 3.76N_2) \rightarrow 2CO_2 + 3H_2O + 11.16N_2 \quad (5.2)$$

$$C_7H_{16} + 11(O_2 + 3.76N_2) \rightarrow 7CO_2 + 8H_2O + 40.92N_2 \quad (5.3)$$

Table 5.1 Reactant mole fractions based on the combustion of 1 mol of butanol

	ϕ=1.0 Fuel	ϕ=0.7 Fuel	LHV	ϕ=1.0 Oxygen	ϕ=0.7 Oxygen	ϕ=1.0 Nitrogen	ϕ=0.7 Nitrogen
	[%]	[%]	[MJ/kg]	[%]	[%]	[%]	[%]
Butanol	3.41	2.41	33.075	20.46	20.67	76.13	76.92
Ethanol	6.59	4.70	28.865	19.79	20.19	73.62	75.11
Heptane	1.90	1.33	44.566	20.78	20.91	77.32	77.76

5.1 Pressure and Temperature

Pressure and temperature information as a function of time and crank angle are provided in the six panels of Figure 5.1 for the three fuels and stoichiometric conditions. In order to correlate real time with crank angle degrees, a frequency of 50Hz was considered and the top dead center was reached at t=0.01s. Butanol highest temperatures do not exceed 3000K, whereas the peak temperatures for ethanol and n-heptane are 3092K and 3220K respectively. It is recognized that these values are unrealistic – this is probably due to the adiabatic calculation that is performed here. However, it is noted that for the same heat release, butanol combustion reaches lower temperatures. As far as pressure is concerned, butanol shows again the lowest peak compared to the other fuels. In particular, butanol peak pressure corresponds to 106.3 bar, ethanol to 133.9 bar and n-heptane to 138.6 bar. Figure 5.2 presents the corresponding results for ϕ=0.7. In this case, all fuels combust below 3000K and 125 bar.

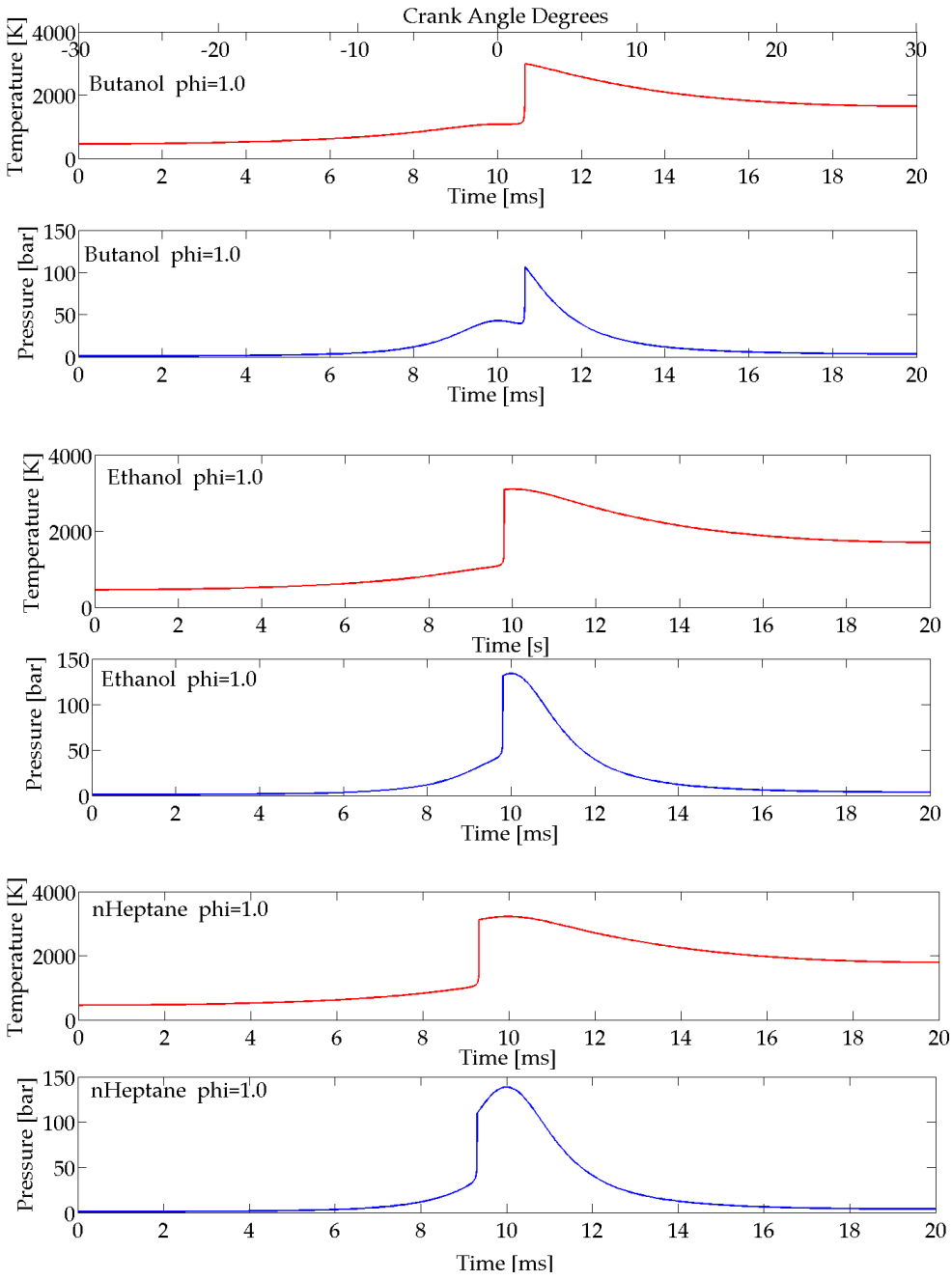

Figure 5.1 Pressure and temperature variation in the cylinder as a function of time for butanol, ethanol and n-heptane at stoichiometric conditions

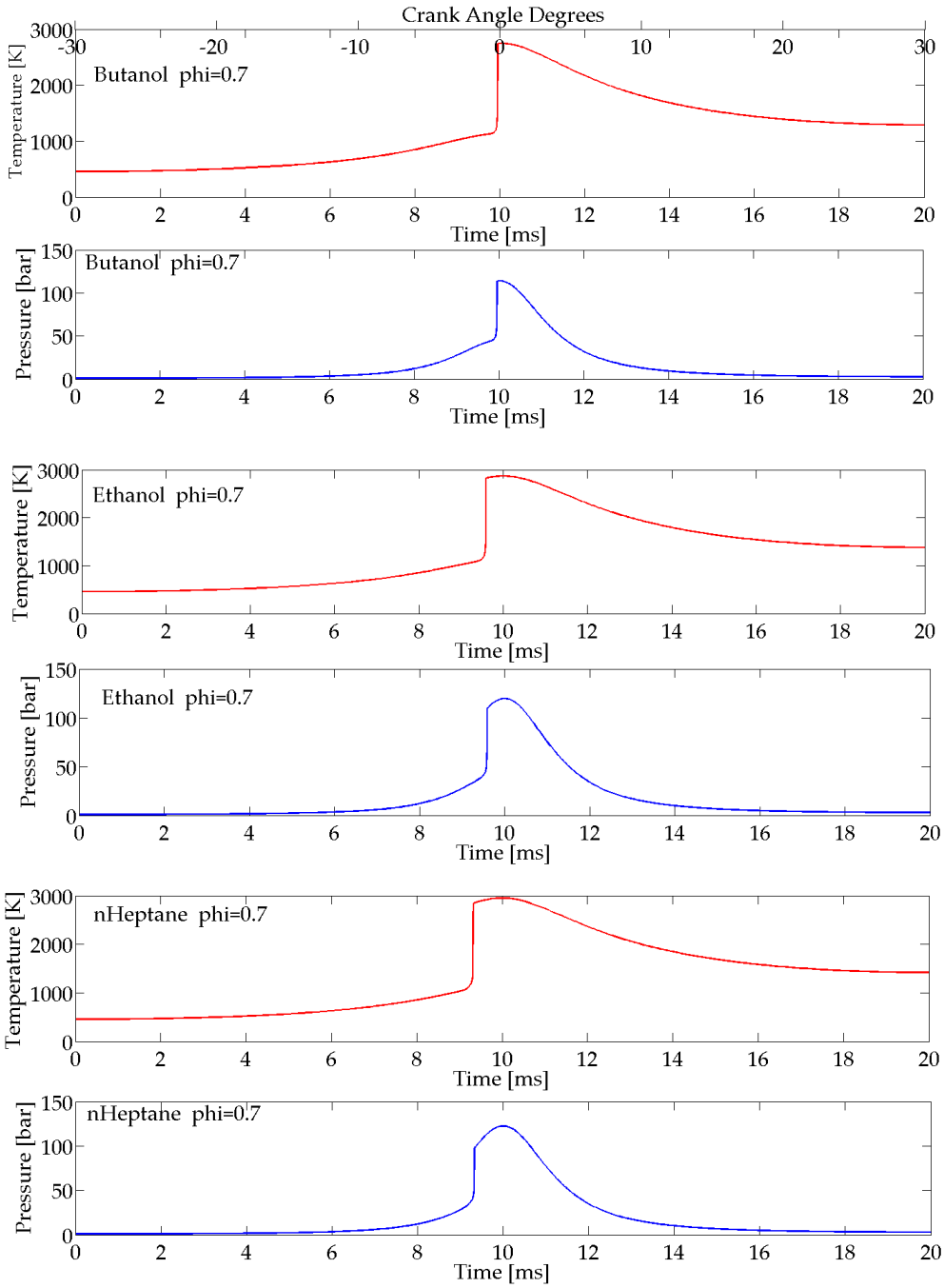

Figure 5.2 Pressure and temperature variation in the cylinder as a function of time for butanol, ethanol and n-heptane at lean conditions

In the particular system considered here, the ignition delay period cannot be defined as in usual diesel engine applications, since no fuel is injected in the chamber. Alternatively, the ignition timing will be considered here, which correlates solely to the start of combustion defined through the temperature distribution, since all mixtures have the same initial temperature and heat release per volume. In other words, the premixture is considered to ignite at the particular instance when the temperature-jump shown in Figs. 5.1 and 5.2 occurs. This mode of combustion has some similarity with HCCI combustion, which uses early injection so as to achieve homogeneous mixture at the point of autoignition. It is true though that the reactor used for this simulation is far from realistic engine conditions.

Considering ignition timing, the start of combustion takes place at 10.54 ms for butanol, 9.77 ms for ethanol and 9.25 ms for heptane, at stoichiometric conditions. The corresponding values for ϕ=0.7 are: 9.90 ms, 9.54 ms and 9.21 ms for the three fuels respectively, showing that butanol is characterized by a slower auto-ignition timing for both equivalence ratios. In the lean case though, the ignition timings are brought closer for the three fuels and occur earlier than in the stoichiometric case.

5.2 Major Species

Major species concentrations of butanol, ethanol and n-heptane are presented in Figs. 5.3 and 5.4, as a function of time and crank angle degrees, for ϕ=1.0 and ϕ=0.7 respectively.

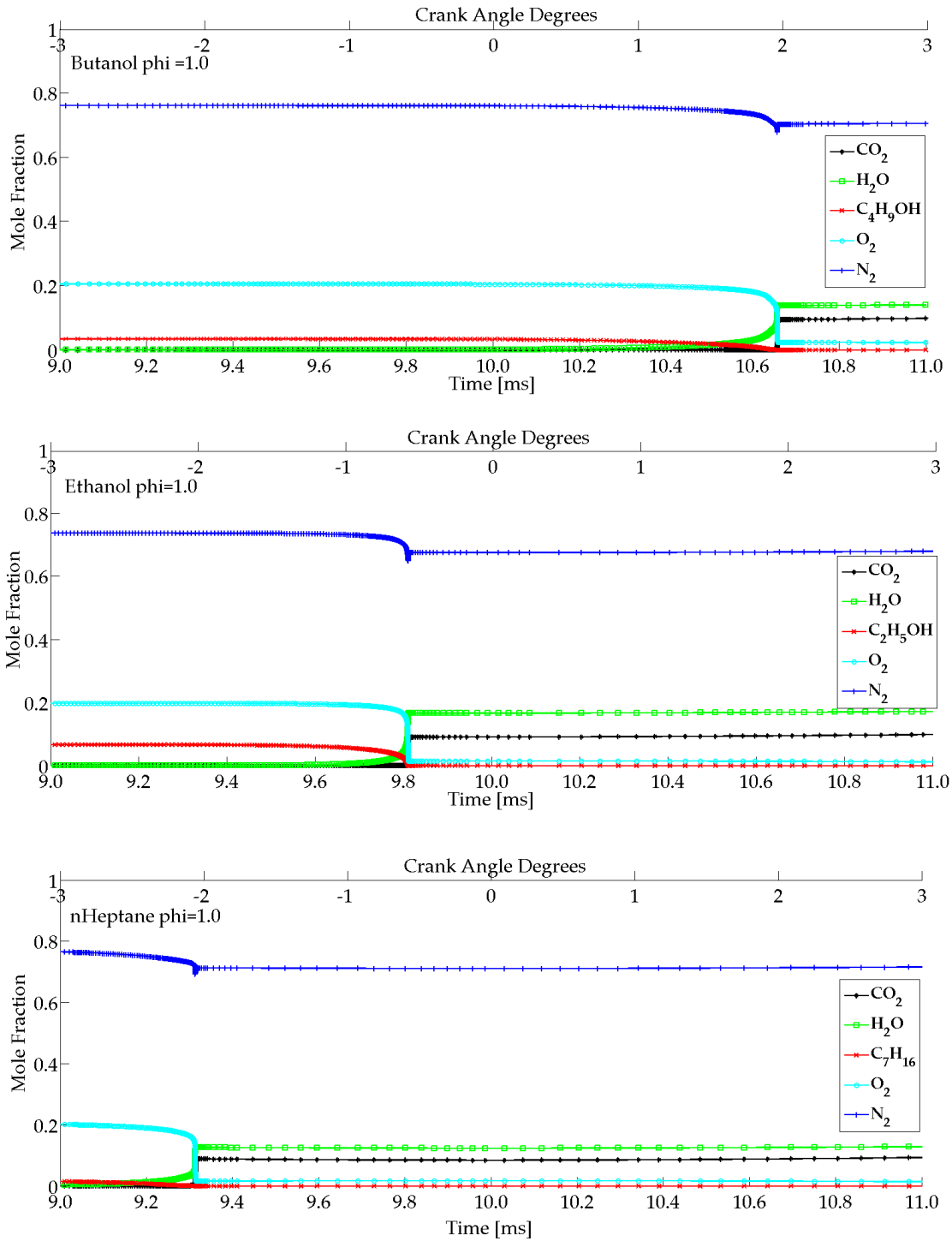

Figure 5.3 Major species concentrations for Butanol, Ethanol and n-Heptane for stoichiometric combustion

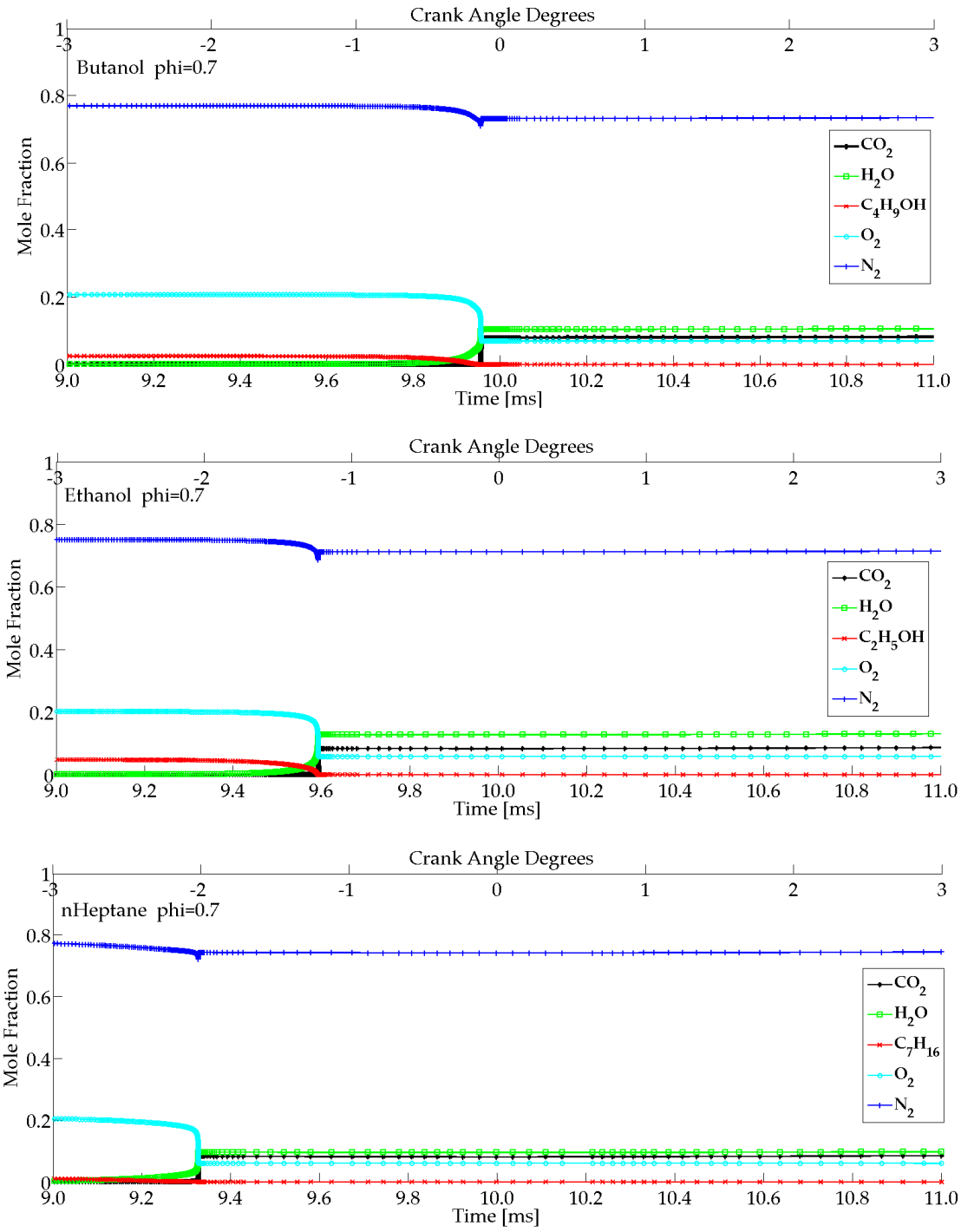

Figure 5.4 Major species concentrations for Butanol, Ethanol and n-Heptane for lean combustion

Reactants are depleted during the oxidation reaction. Products, namely CO_2 and H_2O are formed at that time and N_2 mole fraction decreases slightly. It is worth highlighting here that the ignition timing described earlier is clearly demonstrated in Figs. 5.3 and 5.4. The timing for the reaction initiation is reduced as the fuel changes from butanol to heptane, revealing that the slowest ignition timing occurred for butanol, for both equivalence ratios.

5.3 Intermediate Combustion Species

Mole fractions of four important intermediate species observed during combustion are presented in Figs. 5.5-5.8. Each figure corresponds to a particular combustion intermediate, namely: O, H, OH radicals and HCHO (formaldehyde) and shows its time variation in the combustion of the three fuels considered here. In addition, each figure contains two panels, one for stoichiometric and one for lean combustion.

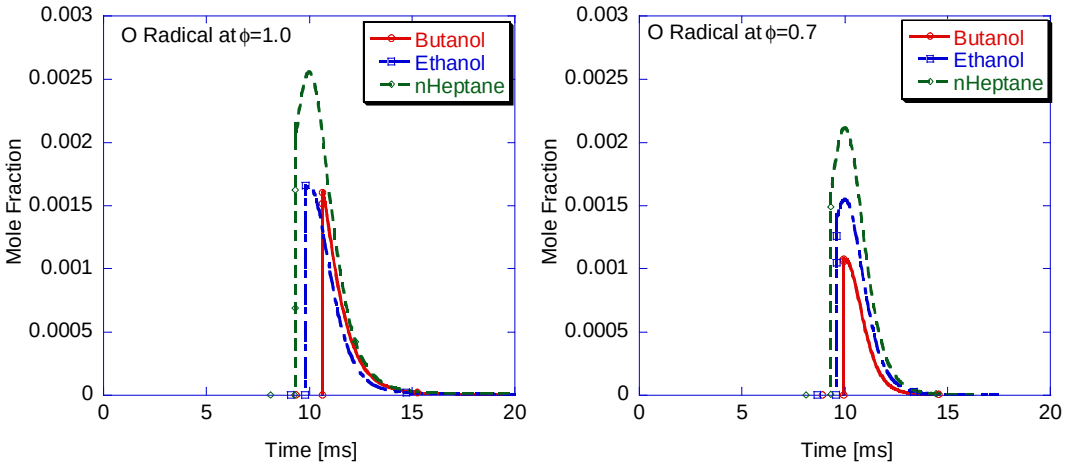

Figure 5.5 Mole fraction for O radical at stoichiometric and lean conditions

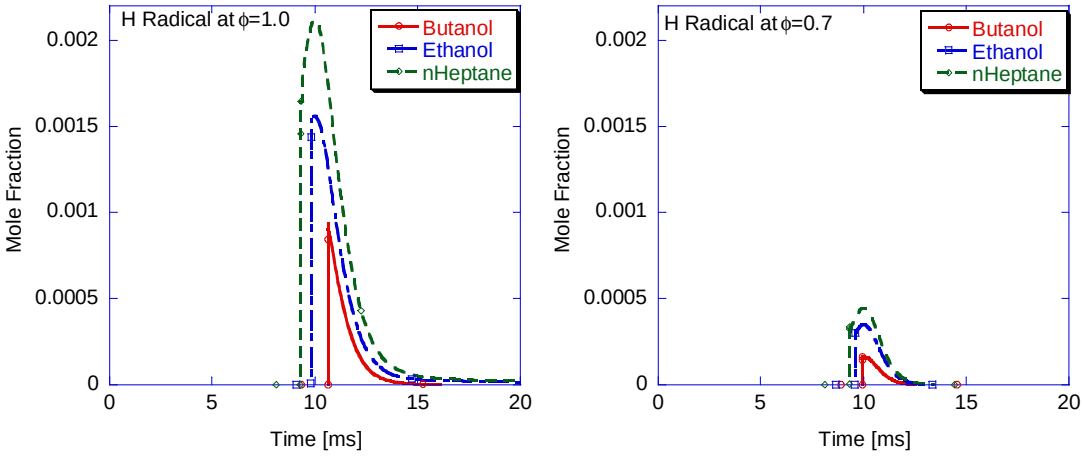

Figure 5.6 Mole fraction for H radical at stoichiometric and lean conditions

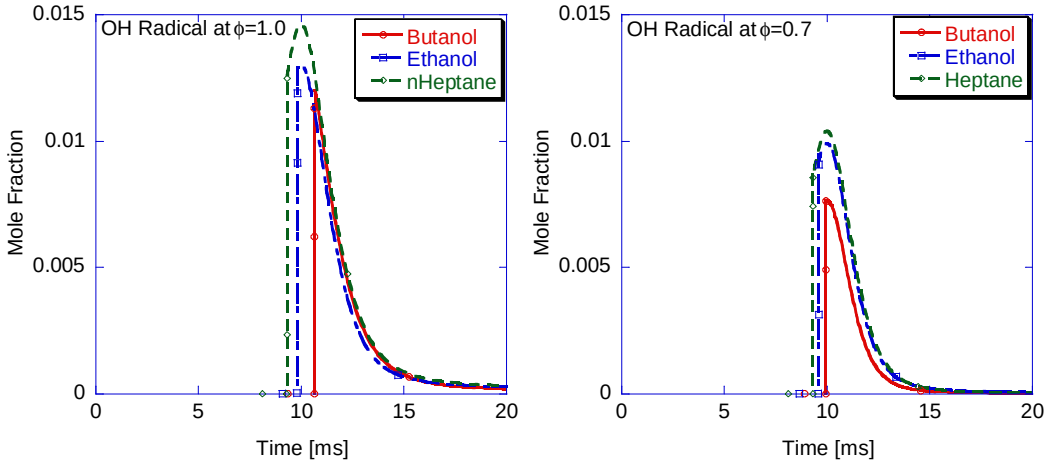

Figure 5.7 Mole fraction for OH radical at stoichiometric and lean conditions

The importance of these combustion intermediates is closely related to the oxidation mechanisms of the considered fuels. In particular, hydrocarbon oxidation usually initiates through collisions and radical H is released. This radical will react with O_2 to produce OH and O radicals and the radical pool begins to built-up. In the case of alcohols, oxidation initiates mainly by H-abstraction which takes place by active H, O

and OH radicals. These combustion intermediates are particularly unstable and as seen in the Figs.5.5-5.7, they do not survive combustion. Especially in excess of O_2, their rate of consumption is even higher and in particular, H radical is barely observed in the lean case. The mechanism of heptane, produces the highest amount of radicals, followed by ethanol, for both equivalence ratios. It is also noticeable that their order of appearance essentially correlates to the ignition timing, which is the shortest for heptane and the highest for butanol.

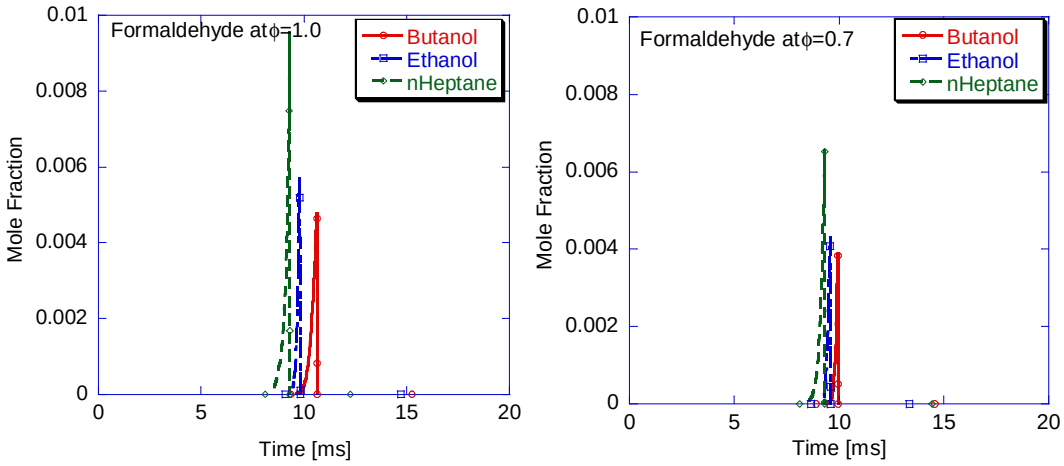

Figure 5.8 Mole fraction for formaldehyde HCHO at stoichiometric and lean conditions

Except for the three radicals, the formation of formaldehyde is also important to monitor mainly because its formation follows the initiation steps of the mechanism of both hydrocarbons and alcohols. In principle, it is a stable species, however the duration of its survival in the combustion environment is negligible, since it reacts with radicals O, H and OH, towards the formation of CO and CO_2. Similarly to the previous results,

butanol produces the least amount of HCHO. This is counter-intuitive because one would expect more formaldehyde from an oxygenated fuel, but it seems that the intermediate steps are such that less HCHO is produced in the butanol case. The fate of the O-atom in the fuel should be investigated through detailed chemical considerations that are beyond scope here. During lean combustion, HCHO production decreases for all fuels.

5.4 Summary

In summary, two butanol combustion simulations were performed in a closed system of varying volume, one for stoichiometric and one for lean combustion (ϕ=0.7). Similar computations were performed for ethanol and heptane. It was shown that, for the same heat release, butanol combustion reached lower peak pressures and temperatures than the corresponding values of both ethanol and heptane. In addition, butanol autoignition occurred after a longer time interval compared to the other fuels for both equivalence ratios. The difference in timing decreased with decreasing the equivalence ratio. Reaction initiation occurred earlier for heptane then for ethanol and later for butanol, as evidenced through computations of major species mol fractions. As far as combustion intermediates (H, O, OH, HCHO) were concerned, the highest amount was produced by heptane, followed by ethanol, for both equivalence ratios, whereas butanol produced the least amount of intermediates. During lean combustion, the production of combustion intermediates decreased for all fuels.

CHAPTER 6

CONCLUSIONS AND RECOMMENDATIONS FOR FUTURE WORK

6.1 Summary and Conclusions

Conclusions of several parts of this study were offered at the end of chapters 3, 4 and 5. Here, some of this material is summarized and repeated for the convenience of the reader.

Butanol was established to be appropriate for the technology of electrostatic atomization, due to the –OH bond in its molecule. Butanol electrospray phenomenology and structure revealed an unsteady behavior of the established sprays that resulted in lack of monodispersity, which was perceived as an important advantage of previous e-spray applications. This polydispersity was observed for all conditions that were examined, namely a wide range of flow rates and applied voltages (5-30 ml/hr and 3-7kV). However, electrospray stability was established within a narrow region of low flow rates (1-4.5 ml/hr). Butanol electrosprays were compared to electrosprays of ethanol and heptane with a 2% Stadis enhancer. Moreover, since in principle electrical conductivity and surface tension are the fundamental properties of such sprays, the electrospray behavior of three alcohol-containing mixtures with equal values for both of these properties was investigated. This investigation showed that the electrospray creation is a function of not solely these two parameters, but also could potentially be

affected by properties such as the liquid dielectric constant, the viscosity and the density. The lack of monodispersity was rationalized through several different factors, namely e-spray menisci oscillations, secondary droplet break-up, and a measured variation of butanol electrical conductivity with the applied electrical field. The lack of monodispersity in oscillating sprays could potentially be out-weighted by enhanced mixing prior to combustion in practical automotive applications.

Pure butanol, as well as methane-assisted butanol non-premixed flames were studied in a counter-flow configuration and their combustion was probed using line Raman imaging. In addition, ethanol and pure methane flames were generated at the same experimental set-up, in order to compare butanol with well-established fuels. Combustion consisted of three zones, the oxidizer, the fuel and the flame zone. In the flame zone, the two reactants did not coexist and were consumed in their entirety. In addition, the flame zone was thicker for butanol and ethanol rather than of methane, for the same heat release, because of the smaller strain on the flames. The investigated flames were highly diluted, thus nitrogen could be treated as a measure of the total mixture density. As far as extinction conditions are concerned, butanol is more resistive to extinction than ethanol for both flames of a same-heat-release or a same-fuel-mass-flow-rate, but is more vulnerable to extinction than methane. Pure butanol flames extinguish at lower strain rates than butanol-methane mixture flames with the same overall equivalence ratio and total combustion heat release. Furthermore, an almost monotonic behavior of the extinction strain rate was observed with increasing heat

release, both in pure butanol and in the mixture cases. The scalar dissipation rate at the stoichiometric surface was approximated through the mixing layer thickness δ, the calculation of which was performed through two different approaches. First, it was estimated using the temperature distribution across the flame, which was found to generate a departure of δ from the theoretically expected square-root behavior. For that reason, the scalar dissipation rate at the stoichiometric surface was approximated through the mixture fraction gradient $\left|\nabla Z\right|_{stoich.}$ for three of the previously used flame cases and the results did show a better agreement with theoretical predictions.

Finally, a first approach to butanol kinetic modeling was pursued. Adiabatic butanol combustion was computed in piston-cylinder using a zero-dimensional model with detailed kinetics for stoichiometric and a lean (ϕ=0.7) butanol/air mixtures. The same calculation was repeated for ethanol and heptane. It was found that butanol peak pressures and temperatures were lower than the corresponding values of both ethanol and heptane. These values were unrealistically high for engine applications, due to the adiabatic conditions that were considered. Butanol autoignition occurred with an increased ignition timing compared to the other fuels, however, this difference in timing decreased with decreasing the equivalence ratio. Finally, the mechanism of heptane, produces the highest amount of radicals (O, H, OH) as well as of formaldehyde, followed by ethanol, for both equivalence ratios. It is also noticeable that the order with which these radicals appear in the calculation essentially correlates to the ignition timing, which is the shortest for heptane and the longest for butanol.

6.2 Recommendations for Future Work

With regards to possible directions for future research, the area of butanol oxidation kinetics should be further investigated, along with model validation through experimentation. As described earlier in this study, the area of butanol kinetic modeling is today in embryonic stage. The existing butanol mechanism of 87 species and 884 reactions could be a first step towards mechanism reduction efforts, since it appears that only a finite number of intermediate reactions influences significantly the combustion process. The need for simpler but chemically realistic mechanisms emerges from literature and several useful methods could be employed, such as sensitivity and Jacobian analysis [88-90], detailed reduction [91] and computational singular perturbation theory (CSP) [92].

After obtaining the reduced butanol mechanism, a modeling package such as CHEMKIN or CANTERA could be used to perform the kinetic modeling of butanol oxidation in various experimental configurations. Combustion information such as laminar flame speeds and emissions should be obtained for several equivalence ratios and compositions. Furthermore, the data produced from the simulation could be validated through experimentation, at the configuration considered, in order to investigate the degree of agreement between model and experiment.

The combustion behavior of this novel bio-fuel should attract further interest from the internal combustion engine community. Studies of butanol and butanol-

containing blends could be performed in both spark ignition and diesel engines, since butanol mixes effectively with petroleum diesel as well. Emissions, engine performance and combustion stability could be the fundamental parameters over which the applicability of butanol could be evaluated. In the context of emissions, this new biofuel of increased power density could be combined with Low-Temperature-Combustion technologies such as Homogeneous Charge Compression Ignition that have been shown to contribute to reduced soot and NO_x emissions. It is reminded that oxygenated fuels intrinsically produce less soot. In addition, the compatibility of this fuel with existing infrastructure should be thoroughly investigated, since its properties will directly affect the engine maintenance and life duration. As an ultimate step, "downstream" technologies, such as engine combustion, could be coupled with research into the production stage of butanol from agricultural/biological sources, in order to improve the efficiency of the whole process.

REFERENCES

1. T. Eseji, N. Qureshi and H.P. Blaschek, Production of Acetone-Butanol-Ethanol in a continuous flow bioreactor using degermed corn and chlostridium beijernickii, *Process Biochemistry*, vol. 42, pp. 34-39, 2007.
2. Y. Tashiro, H. Shinto, M. Hayashi, S. Baba, G. Kobayashi and K. Sonomoto, Novel High-Efficient Butanol Production from Butyrate by Non-Growing Clostridium saccharoperbutyl-acetonicum N1-4 (ATCC 13564) with Methyl Viologen, *Biosci. Bioeng*, vol. 104, pp. 238–240, 2007.
3. Y. Tashiro, K. Takeda, G. Kobayashi and K. Sonomoto, High production of acetone–butanol–ethanol with high cell density culture by cell-recycling and bleeding, *Biotechnol*, vol. 120, pp. 197–206, 2005.
4. N. Qureshi and I. S. J. Maddox, Continuous production of acetone-butanol-ethanol using immobilized cells of Clostridium acetobutylicum and integration with product removal by liquid- liquid extraction, *Ferment. Bioeng*, vol. 80, pp. 185–189, 1995.
5. K. Q. Tang and A. Gomez, Monodisperse electrosprays of low electric conductivity liquids in the cone-jet mode, *J. Colloid & Interface Sci*., vol. 184, pp. 500-511, 1996.
6. A. Gomez and K. Q. Tang, Charge and Fission of Droplets in Electrostatic Sprays, *Physics of Fluids*, vol. 6, pp. 405-414, 1994.
7. G.I Taylor, Disintegration of water drops in an electric field, *Proceedings of the Royal Society of London*, vol. 280, pp. 383-397, 1964.
8. K. Tang and A. Gomez, On the structure of an electrostatic spray of monodisperse droplets., *Physics of Fluids*, vol. 6, pp. 2317-2332, 1994.
9. J. Fernández de la Mora and J. Navascues, Generation of submicron monodisperse aerosols in electrosprays., *Journal of Aerosol Science*, vol. 21, pp. 673-676, 1990.
10. Da-ren Chen, D. Y. H. Pui and S. Kaufman, Electrospraying in conducting liquids for monodisperse aerosol generation in the 4nm to 1.8μm diameter range., *Journal of Aerosol Science*, vol. 26, pp. 963-977, 1995.
11. M. S. Agathou, J. W. Powell, C. F. Lee and D. C. Kyritsis, Preliminary experimental study of butanol electrosprays for power generation, *Society of Automotive Engineers*, SAE Paper 2007-24-0020, 2007.
12. E. K. Anderson, A. P. Carlucci, A. de Risi, and D. C. Kyritsis, Electrostatic Effects on Gasoline Direct Injection in Atmospheric Ambiance, *Atomization and Sprays*, vol. 17, pp. 289-313, 2007.
13. E. K. Anderson, A. P. Carlucci, A. de Risi, and D. C. Kyritsis, Experimental Investigation of the Possibility of Automotive Gasoline Spray Manipulation through Electrostatic Field, *International Journal of Vehicle Design*, vol. 45, pp. 61-79, 2007.

14. E. K. Anderson and D. C. Kyritsis, Experimental investigation of combustion of electrostatically charged ethanol blended gasoline droplets, *The 5th Joint meeting of the U.S. Sections of the Combustion Institute*, San Diego, CA, Paper G11, 2007.
15. E. K. Anderson and D. C. Kyritsis, Experimental Investigation of Electrostatically Charged Ethanol/Gasoline Droplet Combustion, *20th Annual Institute for Liquid Atomization and Spray System*, (ILASS-Americas) Conference, Chicago, IL, 2007.
16. J. S. Shrimpton, Pulsed Charged Sprays: Application to DISI Engines During Early Injection, *Int. J. Numer. Meth. Engng.*, vol. 58, pp. 513-536, 2003.
17. J. S. Shrimpton and A. J. Yule, Characterization of Charged Hydrocarbon Sprays for Application in Combustion Systems, *Exp. in Fluids*, vol. 26, pp. 460-469, 1999.
18. R. E. Hetrick and M. H. Parsons, Electrospray for Fuel Injection, SAE Paper 972987, *Society of Automotive Engineers*, Warrendale PA, 1997.
19. M. E. Thomas, R. DiSalvo and P. Makar, Electrostatic Atomization Insertion into Compression Ignition Engines, SAE Paper 2002-01-3053, *Society of Automotive Engineers*, Warrendale PA, 2002.
20. K. C. Thong and F. J. Weinberg, Electrical Control of the Combustion of Solid and Liquid Particulate Suspensions, *Proc. Roy. Soc. Lond.*, vol. 324, pp. 201-215, 1971.
21. K. Kim and R. J. Turnbull, Generation of Charged Drops of Insulating Liquids by Electrostatic Spraying, *J.Appl. Phys.*, vol. 47, pp. 1964-1969, 1976.
22. A. J. Kelly, The Electrostatic Atomization of Hydrocarbon Oils, *J. Inst. Energy*, pp. 312-320, 1984.
23. J. Fernández De La Mora, The effect of Charge Emission from Electrified Liquid Cones , *J. Fluid Mech.*, vol. 243, pp. 561-574, 1992.
24. D. C. Kyritsis, S. Roychoudhury, C. Mc Enally, C. Pfefferle and A. Gomez, Mesoscale combustion: A first step towards liquid fueled batteries, *Experimental Fluid and Thermal Science*, vol. 28, pp. 97-104, 2004.
25. D. C. Kyritsis, B. Coroton, F. Faure, S. Roychoudhury and A. Gomez, Optimization of a catalytic combustor using electrosprayed liquid hydrocarbons for mesoscale power generation, *Comb. and Flame,* vol. 139, pp.77-89, 2004.
26. M. Cloupeau and B. Prunet-Foch, Electrostatic spraying of liquids in cone-jet mode, *Journal of Electrostatics*, vol. 22, pp. 135-159, 1988.
27. M. Cloupeau and B. Prunet-Foch, Electrohydrodynamic spraying functioning modes: a critical review, *J. Aerosol Sci.*, vol. 25, pp. 1021-1036, 1994.
28. F. A. Williams, Recent advances in theoretical descriptions of turbulent diffusion flames. In S. N. B. Murthy, editor, *Turbulent Mixing in Nonreactive and Reactive Flows*, pp. 189-208, Plenum Press, New York, 1975.
29. S. K. Liew, K. N. C. Bray and J. B. Moss, A flamelet model of turbulent non-premixed combustion., *Combust. Sci. and Tech.*, vol. 27, pp.69-73, 1981.
30. N. Peters, Laminar diffusion flamelet models in non-premixed turbulent combustion., *Prog. Energy Combust. Sci.*, vol.10, pp. 319-339, 1984.

31. N. Peters, Laminar flamelet concepts in turbulent combustion., *Twenty-First Symposium (International) on Combustion,* The Combustion Institute, Pittsburg, pp. 1231-1250, 1986.
32. K. N. C. Bray and N. Peters, Laminar flamelets in turbulent flames., in P. A. Libby and F. A. Williams, editors, *Turbulent reacting Flows*, Academic Press, London, pp. 63-113, 1994.
33. S.P. Burke and T.E.W. Schumann, Diffusion flames, *Proceedings of the Combustion Institute*, vol. 1, pp. 2-11, 1928.
34. R.W. Bilger and J. H. Kent, Concentration fluctuations in turbulent jet diffusion flames., *Combustion Science and Technology*, vol.9, 25-29, 1974.
35. A. Liñán, The asymptotic structure of counter-flow diffusion flames for large activation energies, *Acta Astronautica,* vol.1, pp. 1007-1039, 1974.
36. R.W. Bilger, Structure of diffusion flames, *Combustion Science and Technology*, vol.13, 155-170, 1976.
37. K. Seshadri and F.A. Williams, Laminar flow between parallel plates with injection of a reactant at high Reynolds number, *International Journal of Heat and Mass Transfer*, vol.21, pp. 251-253, 1978.
38. H. G. Im, J. H. Chen and J.Y Chen, Chemical Response of Methane/Air Diffusion Flames to Unsteady Strain Rate. *Combustion and Flame,* vol.118, pp. 204–212, 1999.
39. F. A. Williams, *Combustion Theory*, Addison-Wesley, New York, 1986.
40. V. S. Santoro, D. C. Kyritsis, A. Liñán and A. Gomez, Vortex-induced extinction behavior in methane/gaseous flames: A comparison with quasi-steady extinction. *Proceedings of the Combustion Institute*, vol. 28, pp. 2109–2116, 2000.
41. V. S. Santoro, D. C. Kyritsis, and A. Gomez, An experimental study of vortex-flame interaction in counter-flow spray diffusion flames. *Proceedings of the Combustion Institute*, vol. 28, pp. 1023–1030, 2000.
42. V. S. Santoro, D. C. Kyritsis, M. D. Smooke and A. Gomez, Nitric oxide formation during flame/vortex interaction. Proceedings of the Combustion Institute, vol. 29, pp. 2227–2233, 2002.
43. V. S. Santoro, D. C. Kyritsis and A. Gomez, Quantitative scalar dissipation rate measurements in vortex perturbed counter-flow diffusion flames. *Proceedings of the Combustion Institute*, vol. 29, pp. 1679–1685, 2003.
44. V. S. Santoro and A. Gomez, Extinction and reignition in counter-flow spray diffusion flames interacting with laminar vortices. Proceedings of the Combustion Institute, vol. 29, pp. 585-592, 2003.
45. J. S. Kim and F. A. Williams, Structures of flow and mixture-fraction fields for counter-flow diffusion flames with small stoichiometric mixture fractions, Applied Mathematics, vol. 53, No. 6, pp. 1551-1566, 1993.
46. K.Bijjula and D.C. Kyritsis, Experimental evaluation of flame observables for simplified scalar dissipation rate measurements in laminar diffusion flamelets, *Proceedings of the Combustion Institute,* vol. 30, pp. 493–500, 2005.

47. N. Chakraborty, E.R.Hawkes, J.H.Chen, and R.S Cant, The effects of strain rate and curvature on surface density function transport in turbulent premixed methane-air and hydrogen-air flames: A comparative study. *Combustion and Flame*, vol. 154, pp. 259-280, 2008.
48. S. Anirudh; V. Raghavan and U.S.P. Shet, Experimental investigation of characteristics of a diffusion flame established over liquid ethanol surface under opposed air flow Source, *Experimental Thermal and Fluid Science*, v 33, p 538-541, 2009.
49. S. M. Sarathy, M. J. Thomsona, C. Togbéb, P. Dagautb, F. Halterc and C. Mounaim-Rousselle, An experimental and kinetic modeling study of *n*-butanol combustion. *Proceedings of the Combustion Institute*, vol. 156, pp. 852-864 , 2009.
50. F. N Alasfour, Butanol - A single-cylinder engine study: Availability analysis. App. Thermal Eng. 1997; 17: 537–549.
51. F. N. Alasfour, Butanol - A single cylinder engine study: Engine performance. Int. J. Energy Res. 1997; 21: 21–30.
52. M. Gautam and D. W. Martin. Combustion Characteristics of Higher-alcohol/gasoline Blends. Proc. Inst. Mech. Eng., Part A 2000; 214: 497–511.
53. M. Gautam, D. W. Martin and D. Carder. Emissions Characteristics of Higher Alcohol/gasoline Blends. Proc. Inst. Mech. Eng. Part A 2000; 214: 165–182.
54. D.C. Rakopoulos , C.D. Rakopoulos, E.G. Giakoumis, A.M. Dimaratos, D.C. Kyritsis, Effects of butanol–diesel fuel blends on the performance and emissions of a high-speed DI diesel engine, *Energy Conversion and Management*, in press, 2010.
55. J. Dernotte, C. Mounaim-Rousselle, F. Halter and P. Seers, Evaluation of Butanol-Gasoline Blends in a Port Fuel-injection, Spark-Ignition Engine, *Oil & Gas Sc. And Technology-Revue de'l Institut Francais du Petrole*, vol. 65, issue: 2, pp. 345-351, 2010.
56. S. Szwaja and J. D. Naber, Combustion of n-butanol in a spark-ignition IC engine, *Fuel*, vol. 89, issue: 7, pp. 1573-1582, 2010.
57. P. Dagaut, S.M. Sarathy, M.J. Thomson, A chemical kinetic study of n-butanol oxidation at elevated pressure in a jet stirred reactor, *Proc. Combust. Inst.*, 32, pp. 229–237, 2009.
58. P. Dagaut and C. Togbé, Experimental and modeling study of the kinetics of oxidation of butanol-n-heptane mixtures in a jet-stirred reactor, *Energy & Fuels*, vol. 23, pp. 3527–3535, 2009.
59. P. Dagaut and C. Togbé, Oxidation kinetics of butanol–gasoline surrogate mixtures in a jet-stirred reactor: Experimental and modeling study, *Fuel*, vol. 87,pp. 3313–3321, 2008.
60. T. Le Cong, P. Dagaut, Kinetics of natural gas, natural gas/syngas mixtures oxidation and effect of burnt gas recirculation: experimental and detailed modeling, *Proceedings of the ASME Turbo Expo 2007*: Power for Land, Sea and Air, Montreal, Canada, pp. 1–9, May 14–17, 2007.
61. Y. Zhang and A. L. Boehman, Oxidation of 1-butanol and a mixture of n-heptane/1-butanol in a motored engine, in press, 2010.

62. P. S. Velo, Y. L. Wanga, F. N. Egolfopoulos, C. K. Westbrook, A comparative experimental and computational study of methanol, ethanol, and n-butanol flames, *Combustion and Flame*, in press, 2010.
63. D.R. Lide, CRC Handbook of Chemistry and Physics 75th ed., *CRC Press*, London 1994.
64. P. Atkins and J. de Paula, Physical chemistry 8th ed., *W.H. Freeman and Co.*, New York, 2006.
65. L. Grunberg and A. H. Nissan**,** The additivity of T_c^3 for some non-linear molecules, *Trans. Faraday Soc.*, vol. 44, pp. 1013-1021, 1948.
66. R.C. Reid, J.M. Prausnitz and B.E. Poling, The properties of gases and liquids 4th ed., *McGraw-Hill*, New York, 1987.
67. D. B. Macleod, On a Relation between surface tension and density, *Trans. Faraday Soc.*, vol. 19, pp. 38, 1923.
68. A. C. Eckbreth, Laser diagnostics for combustion temperature and species- 2nd edition, *Gordon and Breach*, Amsterdam, 1996.
69. G. Herzberg, Molecular spectra and molecular structure. I. Spectra of diatomic molecules-2nd edition, *D. Van Nostrand*, New York, 1950.
70. N. M. Marinov, A Detailed Chemical Kinetic Model for High Temperature Ethanol Oxidation, *Int. J. Chem. Kinet.*, vol: 31**,** pp. 183-220, 1999.
71. H. Seiser, H. Pitsch, K. Seshadri, W. J. Pitz, and H. J. Curran, Extinction and Autoignition of n-Heptane in Counterflow Configuration, *Proceedings of the Combustion Institute*, vol. 28, pp. 2029-2037, 2000.
72. J. W. S. Rayleigh, On the conditions of instability of electrified drop, with applications to the electric discharge from liquid points, *Proc. R. Soc.*, vol. 29, pp. 71-83, 1879.
73. K. Q. Tang and A. Gomez, Generation of monodisperse water droplets from electrosprays in a corona-assisted cone-jet mode, *J. Colloid & Interface Sci.*, vol.175, pp. 326-332, 1997.
74. I. Hayati, A. I. Bailey, and TH. F. Tadros, Investigations into the mechanisms of electrodynamic spraying of liquids, *Colloid Interface Sci.*, vol.117, pp. 205, 1987.
75. D. P. H. Smith, The electrodynamic atomization of liquids, *IEEE Trans. Ind. Appl.* IA-, vol. 22, pp. 527, 1986.
76. A. R. Jones and K. C. Thong, The production of charged monodisperse fuel droplets by electrostatic dispersion, *Phys. D. Appl. Phys.*, vol. 4, pp. 1159, 1971.
77. M. Pilch and C. A. Erman, Use of breakup time data and velocity history data to predict the maximum size of stable fragments for acceleration-induced break-up of a liquid drop, *International Journal of Multiphase Flow*, vol. 13, issue 6, pp. 741-757, 1987.
78. L. Wang, R. Stevens, A. Malik, P. Rockett, M. Paine, P. Adkin, S. Martyn, K. Smith, J. Stark and P. Dobson, High-aspect-ratio silica nozzle fabrication for nano-emitter electrospray applications, *Microelectronic Engineering*, 84 , pp. 1190–1193, 2007.
79. N. Peters, Turbulent combustion 2nd ed., *Cambridge University Press*, New York, 2002.

80. M. Matalon, Flame dynamics, *Proceedings of the Combustion Institute*; vol.32, pp. 57-82, 2009.
81. C. K. Law, Combustion physics 1st ed., *Cambridge University Press*, New York, 2006.
82. G. Wang, A. N. Karpetis and R. S. Barlow, Dissipation length scales in turbulent nonpremixed jet flames, *Proceedings of the Combustion Institute*, vol. 148, pp. 62-75, 2007.
83. American National Standards Institute/American Society of Mechanical Engineers, Test Uncertainty, *ASME*, PTC 19.1-1998, New York, 1998.
84. American Institute of Aeronautics ans Astronautics, Assessment of Wind Tunnel Data Uncertainty, *AIAA*, AIAA Standard S-071-1995, New York, 1995.
85. H. W. Coleman and W. G. Steele, Experimentation and Uncertainty Analysis for Engineers 2nd ed., *John Wiley & Sons Inc.*, New York, 1999.
86. J. P. Holman, Experimental Methods for Engineers 7th ed., *Mc Graw Hill*, New York, 2001.
87. International Organization for Standardization, Guide to the Expression of Uncertainty in Measurement, *ISO*, Geneva, 1993.
88. T. Tunanyi, Reduction of large reaction mechanisms, *New J. Chem.*, vol. 14, pp. 795-803, 1990.
89. A. S. Tomlin, M. J. Pilling, T. Tunanyi, J. H. Merkin and J. Bradley, Mechanism reduction for the oscillatory oxidation of hydrogen: Sensitivity and quasi-steady-state analyses, *Combustion and Flame*, vol. 91, pp.107-130, 1992.
90. A. S. Tomlin, T. Tunanyi and M. J. Pilling, Mathematical tools for the construction, investigation and reduction of combustion mechanisms, *Comprehensive Chemical Kinetics*, pp.293-437, 1997.
91. H. Wang and M. Frenklash, Detailed reduction of reaction mechanisms for flame modeling, *Comb. and Flame*, vol. 87, pp.365-370.
92. D. A. Goussis and S. H. Lam, A study of homogeneous methanol oxidation kinetics using CSP, Proc. Comb. Inst., vol. 22, pp. 113-120, 1992.

APPENDIX A

Electrospray Structure: Velocity Information

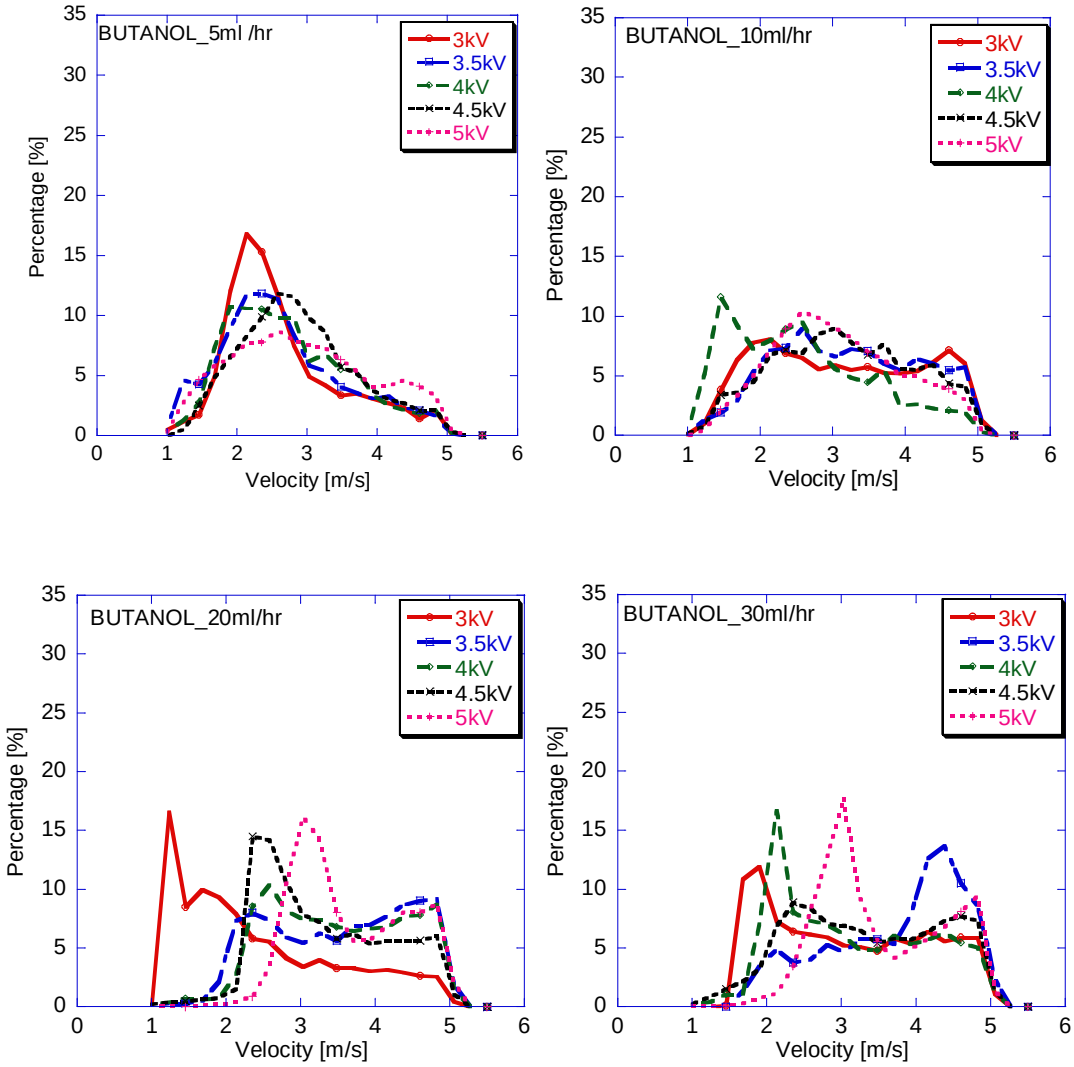

Figure A.1 Velocity distribution of Butanol for flow rates 5ml/hr, 10ml/hr, 20ml/hr and 30ml/hr

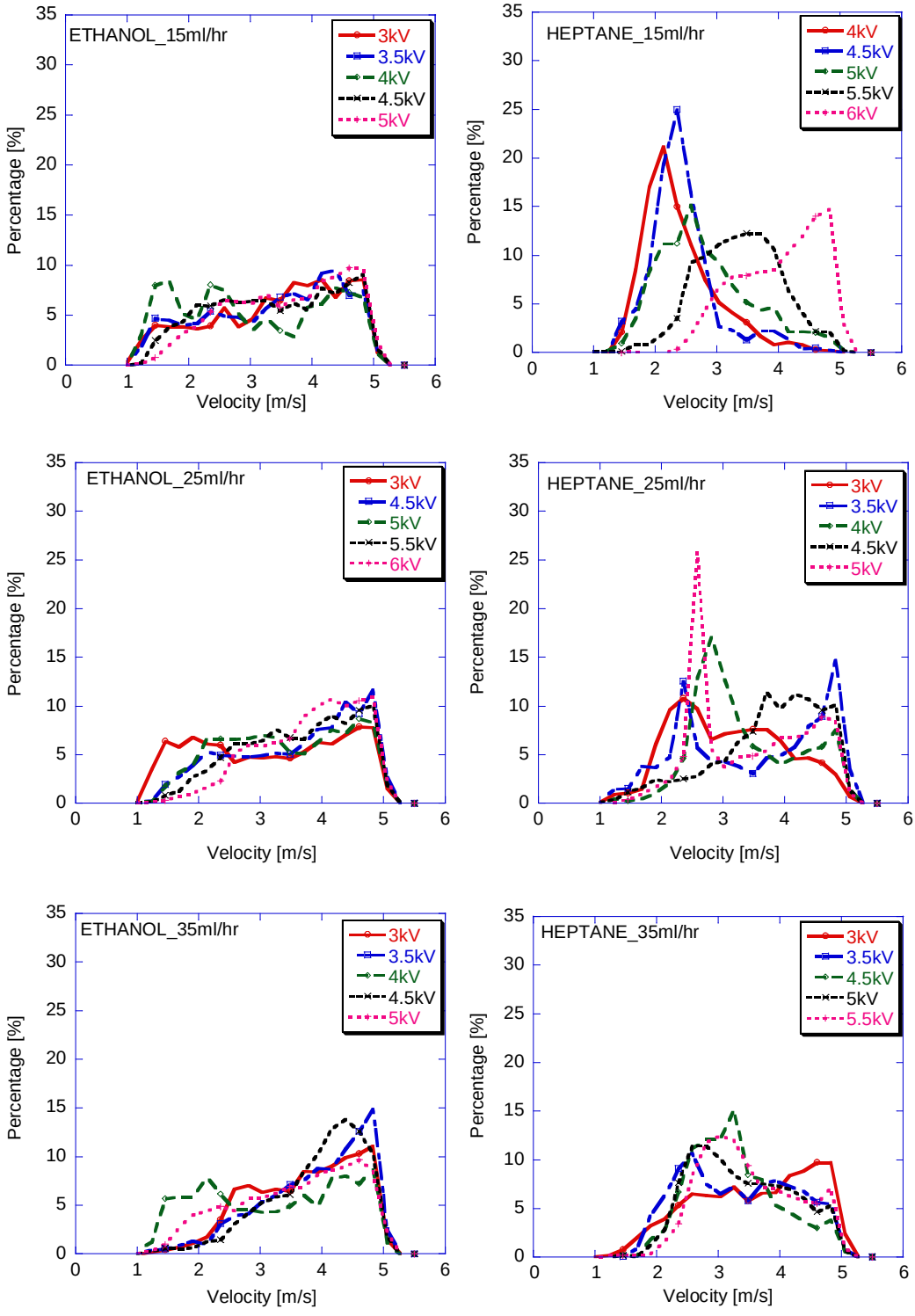

Figure A.2 Velocity distribution of Ethanol and Heptane for flow rates 15ml/hr, 25ml/hr and 35ml/hr

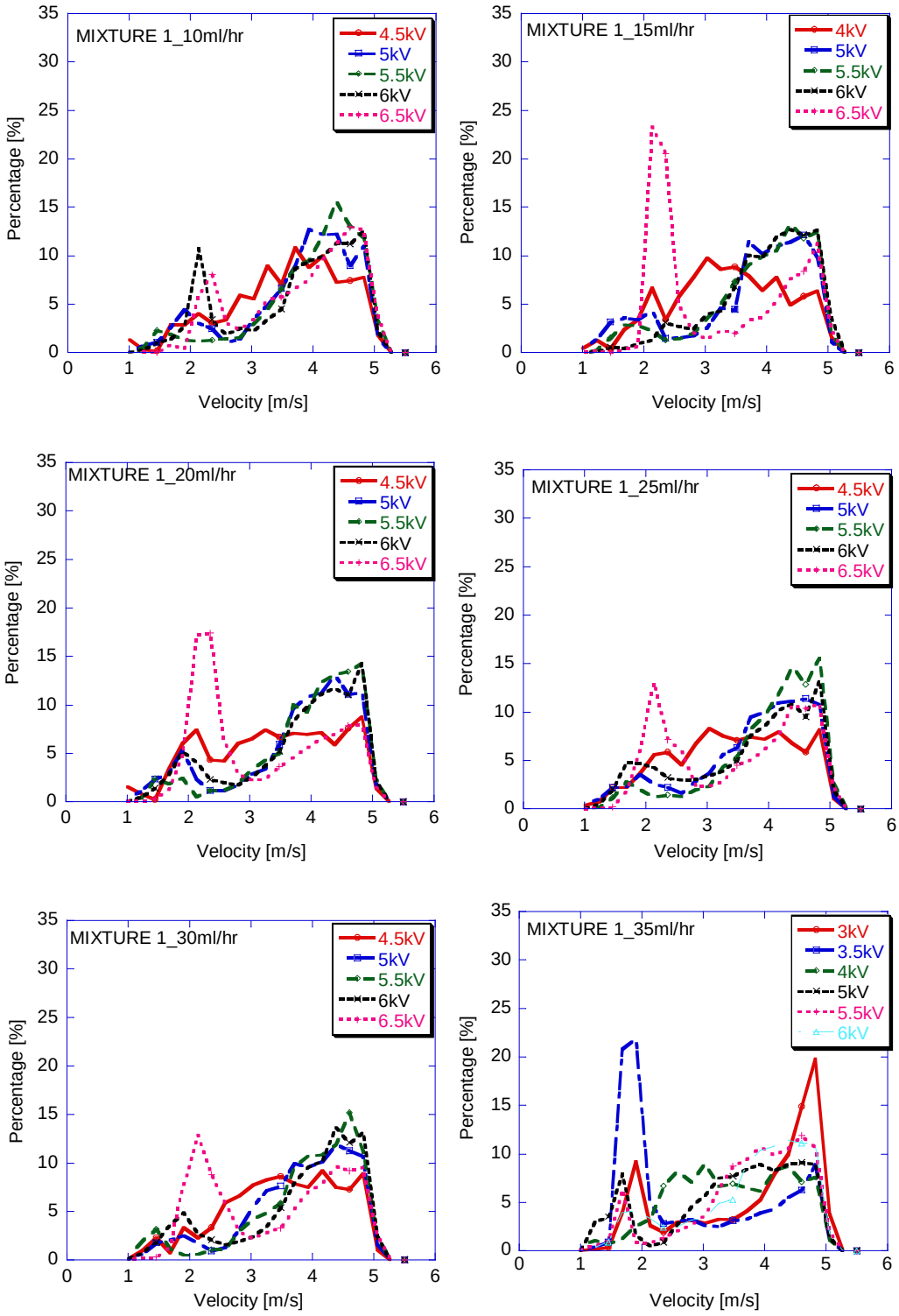

Figure A.3 Velocity distribution of Mixture 1 for flow rates 10ml/hr, 15ml/hr, 20ml/hr, 25ml/hr, 30ml/hr and 35ml/hr

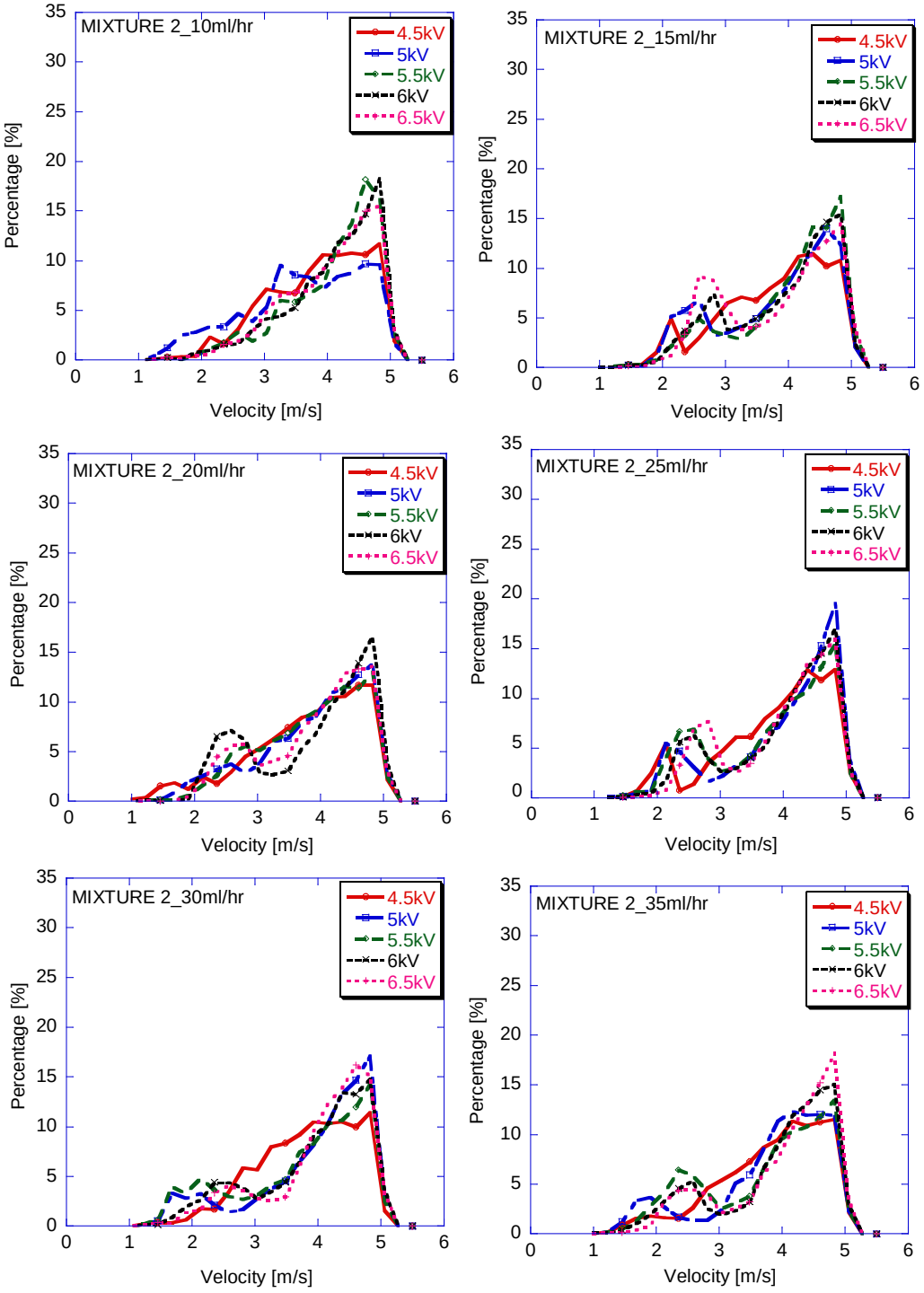

Figure A.4 Velocity distribution of Mixture 2 for flow rates 10ml/hr, 15ml/hr, 20ml/hr, 25ml/hr, 30ml/hr and 35ml/hr

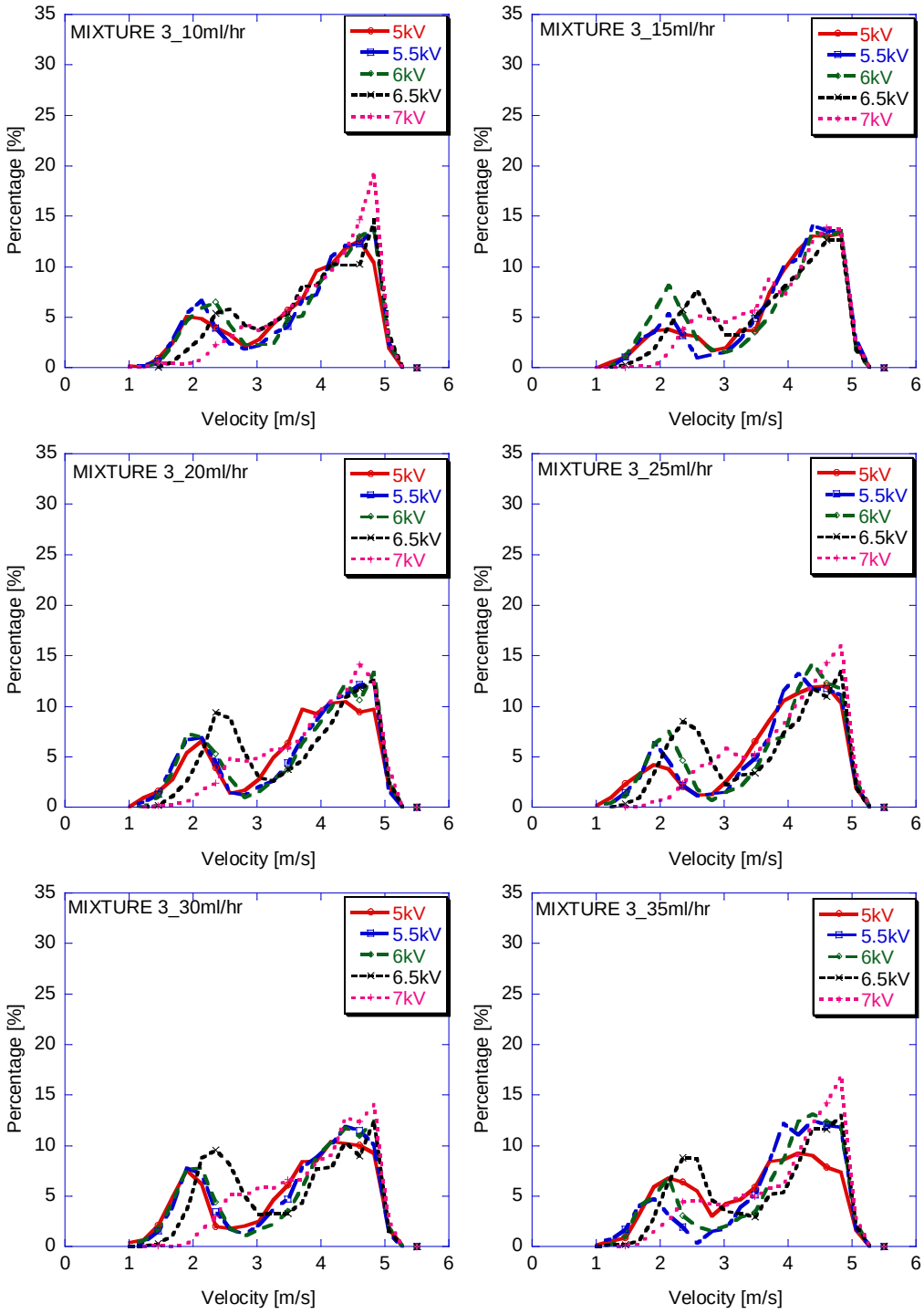

Figure A.5 Velocity distribution of Mixture 3 for flow rates 10ml/hr, 15ml/hr, 20ml/hr, 25ml/hr, 30ml/hr and 35ml/hr

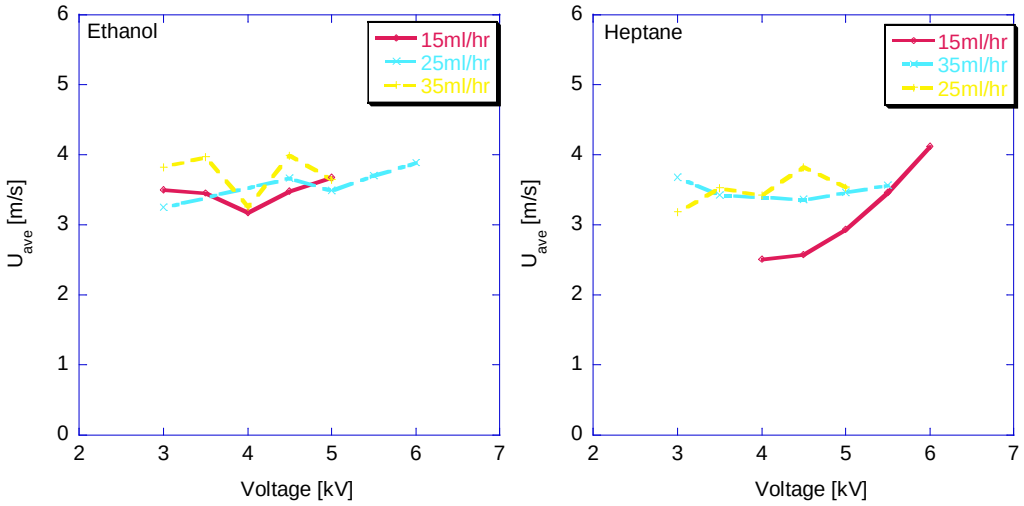

Figure A.6 Effect of the applied voltage on the mean velocity for Ethanol and Heptane

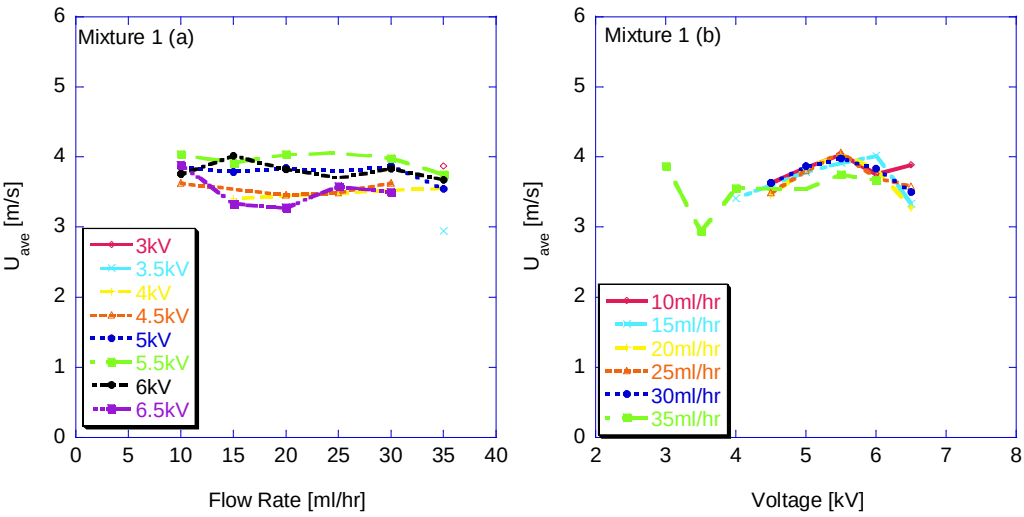

Figure A.7 Effect of the (a) liquid flow rate and (b) of applied voltage on the mean velocity for Mixture 1

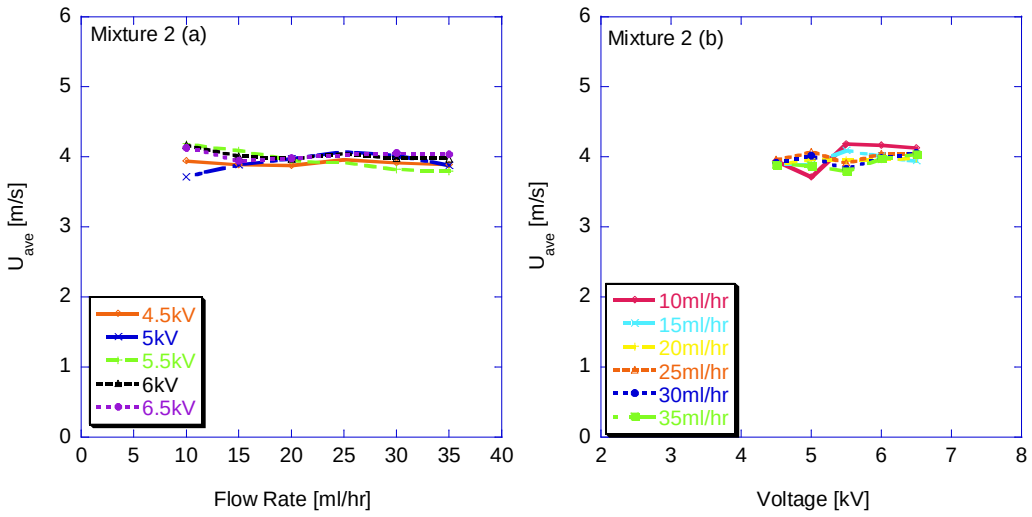

Figure A.8 Effect of the (a) liquid flow rate and (b) of applied voltage on the mean velocity for Mixture 2

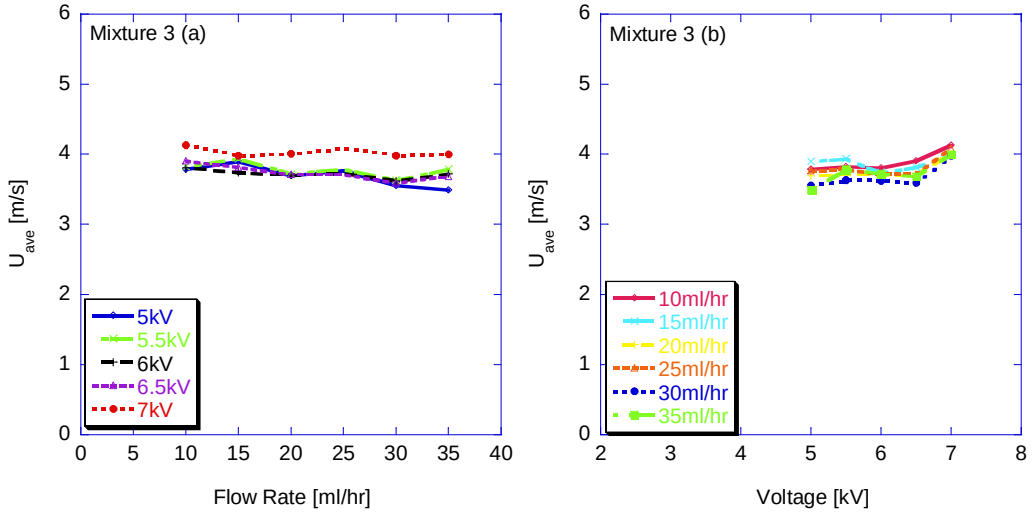

Figure A.9 Effect of the (a) liquid flow rate and (b) of applied voltage on the mean velocity for Mixture 3

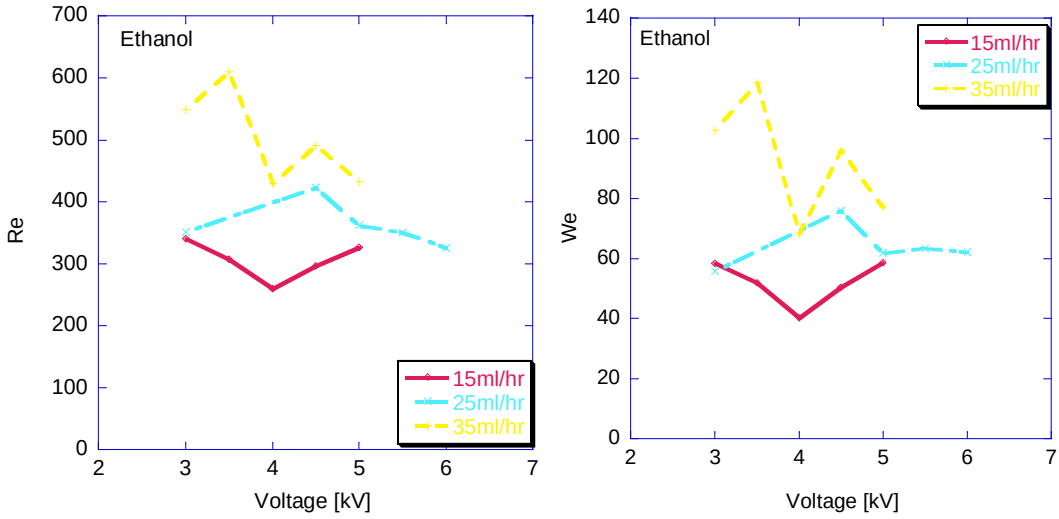

Figure A.10 Effect of voltage on Re and We numbers for Ethanol

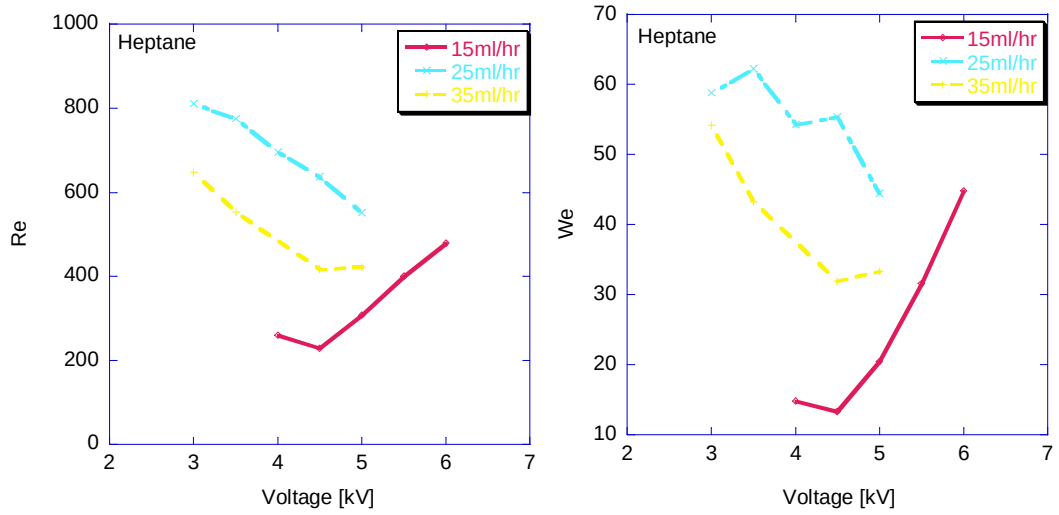

Figure A.11 Effect of voltage on Re and We numbers for Heptane

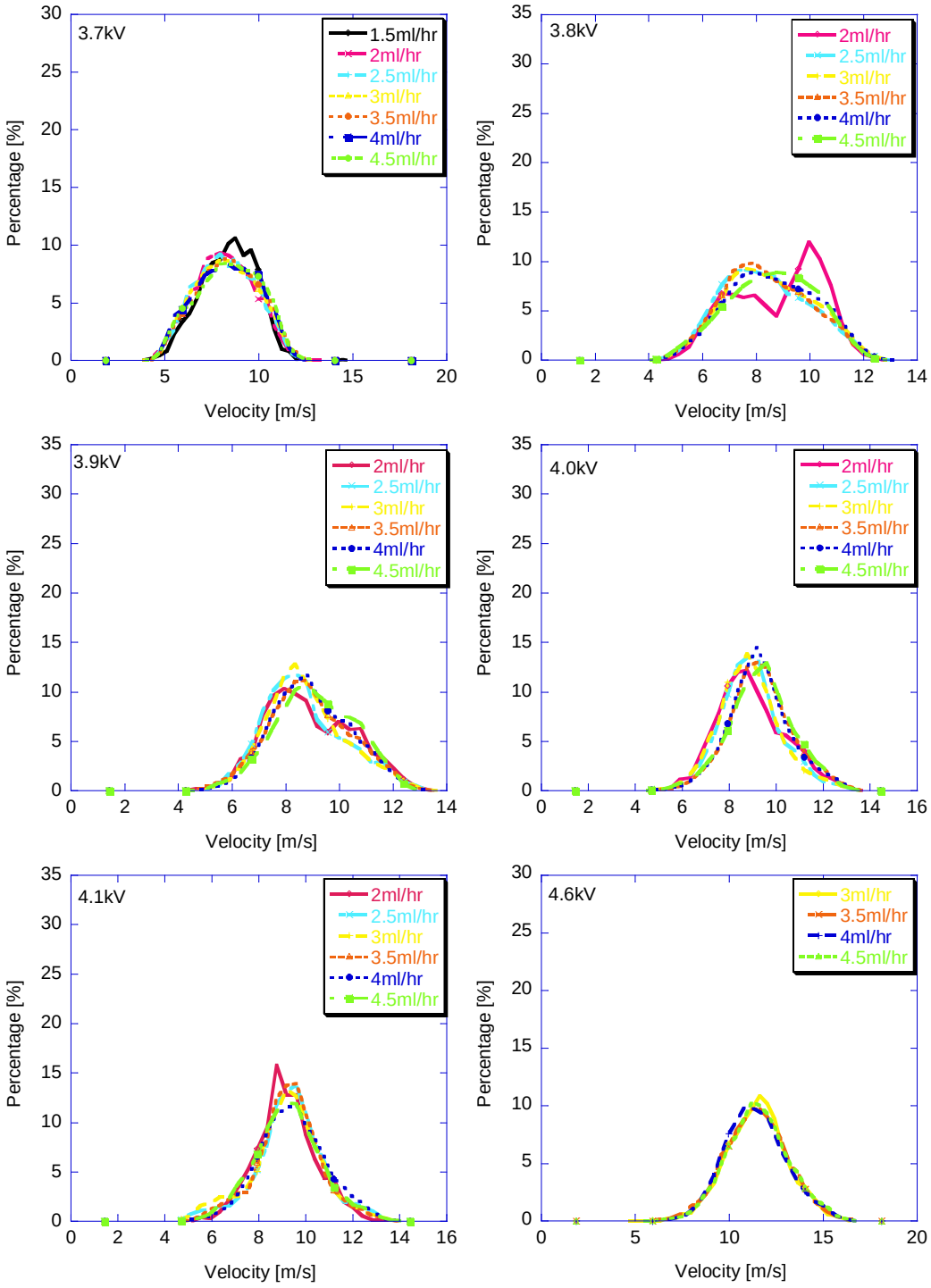

Figure A.12 Velocity distribution for Butanol at low flow rates and voltages 3.7kV, 3.8kV, 3.9kV, 4.0kV, 4.1kV and 4.6kV

APPENDIX B

Extinction Conditions for various Equivalence Ratios

Table B.1 Mass flow rates at extinction, extinction strain rates and total heat released for flames of an overall equivalence ratio ϕ=0.70

Test Case	C_4H_9OH or C_2H_5OH	N_2 for C_4H_9OH or C_2H_5OH stream	CH_4	Total Fuel	N_2 for CH_4 stream	O_2	N_2 for O_2 stream	K_{ext}	Etot
	[x10^{-6}kg/s]	[x10^{-6}kg/s]	[x10^{-6}kg/s]	[x10^{-6}kg/s]	[x10^{-6}kg/s]	[x10^{-6}kg/s]	[x10^{-6}kg/s]	[sec^{-1}]	[W]
A but_HR	6.29	9.41	0.00	6.29	32.40	23.21	19.84	125.9	208.0
A meth_ HR	0.00	0.00	4.14	4.14	44.57	23.67	37.15	173.4	207.2
A eth_ HR	7.19	12.16	0.00	7.19	29.07	14.25	19.84	115.8	207.5
A mixt_ HR	3.37	12.16	1.92	5.29	40.12	23.43	26.66	152.7	207.6
A meth_ FFR	0.00	0.00	6.29	6.29	75.54	35.89	45.71	213.1	314.0
A eth_ FFR	6.29	12.16	0.00	6.29	29.07	12.49	13.31	102.3	181.6
A mixt_FFR	4.02	12.16	2.27	6.29	36.52	27.85	26.66	154.5	246.2
B but_HR	7.19	9.41	0.00	7.19	36.52	26.52	26.66	147.5	237.7
B meth_ HR	0.00	0.00	4.75	4.25	71.30	27.07	25.29	197.3	237.6
B eth_ HR	8.24	12.16	0.00	8.24	30.75	16.35	26.66	132.7	237.9
B mixt_ HR	3.84	12.16	2.21	6.05	41.56	26.87	33.47	170.8	237.5
B meth_ FFR	0.00	0.00	7.19	7.19	82.58	41.04	58.09	247.7	359.0
B eth_ FFR	7.19	12.16	0.00	7.19	29.07	14.25	19.84	115.8	207.5
B mixt_FFR	4.60	12.16	2.59	7.19	43.23	31.89	26.66	170.4	282.1
C but_HR	7.86	9.41	0.00	7.86	33.37	29.17	33.47	157.7	260.0
C meth_ HR	0.00	0.00	5.19	5.19	68.23	29.84	37.15	218.9	259.7
C eth_ HR	9.01	12.16	0.00	9.01	29.07	17.90	26.66	133.2	260.0
C mixt_ HR	4.27	12.16	2.38	6.65	51.60	29.39	33.47	189.0	259.9
C meth_ FFR	0.00	0.00	7.86	7.86	86.53	44.93	64.41	267.7	393.2
C eth_ FFR	7.86	12.16	0.00	7.86	32.40	15.65	19.84	123.1	227.1
C mixt_FFR	5.03	12.16	2.83	7.86	63.23	34.70	33.47	213.8	307.3

Table B.2 Mass flow rates at extinction, extinction strain rates and total heat released for flames of an overall equivalence ratio ϕ=0.85

Test Case	C_4H_9OH or C_2H_5OH	N_2 for C_4H_9OH or C_2H_5OH stream	CH_4	Total Fuel	N_2 for CH_4 stream	O_2	N_2 for O_2 stream	K_{ext}	Etot
	[$x10^{-6}$kg/s]	[$x10^{-6}$kg/s]	[$x10^{-6}$kg/s]	[$x10^{-6}$kg/s]	[$x10^{-6}$kg/s]	[$x10^{-6}$kg/s]	[$x10^{-6}$kg/s]	[sec^{-1}]	[W]
A but_HR	6.29	9.41	0.00	6.29	29.07	19.23	19.84	116.1	208.0
A meth_ HR	0.00	0.00	4.14	4.14	42.68	19.45	37.15	164.5	207.2
A eth_ HR	7.19	12.16	0.00	7.19	25.60	11.76	19.84	107.8	207.5
A mixt_ HR	3.37	12.16	1.92	5.29	36.52	19.34	26.66	142.4	207.6
A meth_ FFR	0.00	0.00	6.29	6.29	71.91	29.55	45.71	201.1	314.0
A eth_ FFR	6.29	12.16	0.00	6.29	25.95	10.28	13.31	95.2	181.6
A mixt_FFR	4.02	12.16	2.27	6.29	33.69	22.87	26.66	144.2	246.2
B but_HR	7.19	9.41	0.00	7.19	33.69	21.88	26.66	137.6	237.7
B meth_ HR	0.00	0.00	4.75	4.75	70.08	23.76	25.29	190.7	237.6
B eth_ HR	8.24	12.16	0.00	8.24	26.66	13.48	26.66	123.3	237.9
B mixt_ HR	3.84	12.16	2.21	6.05	39.54	22.10	33.47	161.8	237.5
B meth_ FFR	0.00	0.00	7.19	7.19	77.33	33.79	58.09	232.5	359.0
B eth_ FFR	7.19	12.16	0.00	7.19	25.60	11.76	19.84	107.8	207.5
B mixt_FFR	4.60	12.16	2.59	7.19	40.99	26.25	26.66	160.0	282.1
C but_HR	7.86	9.41	0.00	7.86	30.41	24.09	33.47	147.0	260.0
C meth_ HR	0.00	0.00	5.19	5.19	65.74	25.97	37.15	209.7	259.7
C eth_ HR	9.01	12.16	0.00	9.01	24.53	14.70	26.66	122.6	260.0
C mixt_ HR	4.27	12.16	2.38	6.65	47.57	24.20	33.47	176.7	259.9
C meth_ FFR	0.00	0.00	7.86	7.86	79.68	37.00	64.41	249.7	393.2
C eth_ FFR	7.86	12.16	0.00	7.86	30.41	12.88	19.84	116.8	227.1
C mixt_FFR	5.03	12.16	2.83	7.86	59.42	28.62	33.47	200.7	307.3

Table B.3 Mass flow rates at extinction, extinction strain rates and total heat released for flames of an overall equivalence ratio ϕ=1.15

Test Case	C_4H_9OH or C_2H_5OH	N_2 for C_4H_9OH or C_2H_5OH stream	CH_4	Total Fuel	N_2 for CH_4 stream	O_2	N_2 for O_2 stream	K_{ext}	Etot
	[$x10^{-6}$kg/s]	[$x10^{-6}$kg/s]	[$x10^{-6}$kg/s]	[$x10^{-6}$kg/s]	[$x10^{-6}$kg/s]	[$x10^{-6}$kg/s]	[$x10^{-6}$kg/s]	[sec^{-1}]	[W]
A but_HR	6.29	9.41	0.00	6.29	25.95	14.11	19.84	105.2	208.0
A meth_ HR	0.00	0.00	4.14	4.14	34.01	14.37	37.15	144.3	207.2
A eth_ HR	7.19	12.16	0.00	7.19	17.83	8.69	19.84	99.9	207.5
A mixt_ HR	3.37	12.16	1.92	5.29	29.41	14.30	26.66	125.9	207.6
A meth_ FFR	0.00	0.00	6.28	6.29	54.89	21.84	45.71	171.0	314.0
A eth_ FFR	6.29	12.16	0.00	6.29	17.05	7.62	13.31	79.2	181.6
A mixt_FFR	4.02	12.16	2.27	6.29	28.04	16.95	26.66	128.6	246.2
B but_HR	7.19	9.41	0.00	7.19	29.74	16.13	26.66	124.7	237.7
B meth_ HR	0.00	0.00	4.75	4.75	60.06	16.58	25.29	165.9	237.6
B eth_ HR	8.24	12.16	0.00	8.24	18.21	9.95	26.66	106.7	237.9
B mixt_ HR	3.84	12.16	2.21	6.05	33.37	16.35	33.47	145.7	237.5
B meth_ FFR	0.00	0.00	7.18	7.19	65.74	24.99	58.09	207.7	359.0
B eth_ FFR	7.19	12.16	0.00	7.19	17.83	8.69	19.84	92.8	207.5
B mixt_FFR	4.60	12.16	2.60	7.19	35.28	19.45	26.66	143.3	282.1
C but_HR	7.86	9.41	0.00	7.86	21.62	17.68	33.47	126.2	260.0
C meth_ HR	0.00	0.00	5.19	5.19	49.59	18.01	37.15	174.6	259.7
C eth_ HR	9.01	12.16	0.00	9.01	17.44	10.90	26.66	107.7	260.0
C mixt_ HR	4.27	12.16	2.38	6.65	36.52	17.90	33.47	152.9	259.9
C meth_ FFR	0.00	0.00	7.86	7.86	69.46	27.36	64.41	225.5	393.2
C eth_ FFR	7.87	12.16	0.00	7.86	25.60	9.50	19.84	105.8	227.1
C mixt_FFR	5.03	12.16	2.82	7.86	48.57	21.15	33.47	175.9	307.3

Table B.4 Mass flow rates at extinction, extinction strain rates and total heat released for flames of an overall equivalence ratio ϕ=1.30

Test Case	C_4H_9OH or C_2H_5OH	N_2 for C_4H_9OH or C_2H_5OH stream	CH_4	Total Fuel	N_2 for CH_4 stream	O_2	N_2 for O_2 stream	K_{ext}	Etot
	[x10^{-6}kg/s]	[x10^{-6}kg/s]	[x10^{-6}kg/s]	[x10^{-6}kg/s]	[x10^{-6}kg/s]	[x10^{-6}kg/s]	[x10^{-6}kg/s]	[sec^{-1}]	[W]
A but_HR	6.29	9.41	0.00	6.29	23.09	12.49	19.84	99.1	208.0
A meth_ HR	0.00	0.00	4.14	4.14	30.75	12.71	37.15	137.1	207.2
A eth_ HR	7.19	12.16	0.00	7.19	15.47	7.69	19.84	92.8	207.5
A mixt_ HR	3.37	12.16	1.92	5.29	26.66	12.64	26.66	119.9	207.6
A meth_ FFR	0.00	0.00	6.28	6.29	48.24	19.33	45.71	159.8	314.0
A eth_ FFR	6.29	12.16	0.00	6.29	13.46	6.72	13.31	72.9	181.6
A mixt_FFR	4.02	12.16	2.27	6.29	25.95	14.98	26.66	123.1	246.2
B but_HR	7.19	9.41	0.00	7.19	27.00	14.37	26.66	118.5	237.7
B meth_ HR	0.00	0.00	4.75	4.75	52.92	14.81	25.29	153.0	237.6
B eth_ HR	8.24	12.16	0.00	8.24	14.27	8.80	26.66	99.6	237.9
B mixt_ HR	3.84	12.16	2.21	6.05	29.41	14.48	33.47	137.7	237.5
B meth_ FFR	0.00	0.00	7.18	7.19	56.84	22.09	58.09	193.3	359.0
B eth_ FFR	7.19	12.16	0.00	7.19	15.47	7.69	19.84	88.2	207.5
B mixt_FFR	4.60	12.16	2.60	7.19	32.40	17.17	26.66	136.3	282.1
C but_HR	7.86	9.41	0.00	7.86	18.60	15.69	33.47	119.3	260.0
C meth_ HR	0.00	0.00	5.19	5.19	45.52	15.91	37.15	209.7	259.7
C eth_ HR	9.01	12.16	0.00	9.01	11.39	9.61	26.66	97.3	260.0
C mixt_ HR	4.27	12.16	2.38	6.65	31.41	15.80	33.47	143.0	259.9
C meth_ FFR	0.00	0.00	7.86	7.86	60.70	24.19	64.41	210.9	393.2
C eth_ FFR	7.87	12.16	0.00	7.86	21.98	8.40	19.84	99.2	227.1
C mixt_FFR	5.03	12.16	2.82	7.86	42.95	18.67	33.47	164.7	307.3

AUTHOR'S BIOGRAPHY

Maria Agathou was born January 20, 1981 in Corfu, Greece. After graduating from the 2nd High school of Corfu in 1998, she succeeded in the National University entrance exams and attended the Chemical Engineering Department of the National Technical University of Athens (NTUA), Greece, for the academic year 1998-1999. In the Fall of 1999, she enrolled in the Mechanical Engineering Department of NTUA, Greece and she graduated in September of 2004 with a Diploma (combined B.S. and M.S.) in Mechanical Engineering. Her Master's thesis was titled: "Analysis of two pilot and one main injection strategy in direct injection diesel engines for reduction of emissions and combustion noise in near-idle conditions" and was conducted in the Center of Thermal Engines, in the Polytechnic University of Valencia, Spain. She obtained an additional Master's degree in September, 2005 with a Master's thesis titled: "Thermal study of an optical direct injection diesel engine through heat release rate diagrams and combustion visualization". The M.S. program, called *Energy Production and Management*, was offered as a collaboration of the Mechanical and Electrical Engineering Departments at NTUA, Greece. Both Master's thesis were submitted at NTUA under the supervision of Prof. Constantinos. D. Rakopoulos.

Maria then continued her graduate studies in order to pursue a Ph.D. degree at the University of Illinois at Urbana-Champaign, under the supervision of Professor Dimitrios C. Kyritsis in the Combustion Physics Laboratory. As a research assistant, her work has led to several journal publications and conference proceedings (the exact number of which is yet to be determined). In Spring of 2008, she was also a teaching assistant for the undergraduate course Heat Transfer. In Spring of 2009, she joined team Caterpillar to work as a Corporate Intern in the Engine Lab of the *Global Engine Development-NA,* in Mossville, IL. After completion of her Ph.D. degree she will be working in the Fuel Industry in Athens, Greece.